Development Of Resistive Plate Chamber For The CBM Experiment At FAIR And Other Application Of Radiation Detector

Corrected Copy

Thesis submitted for the degree of
Doctor of Philosophy (Science)
in
Physics

By
Arindam Sen

Department of Physics
University of Calcutta

2023

Dedicated to

My Parents

Acknowledgements

It is my pleasure to acknowledge the people who helped me in many ways to complete my Ph.D. research work.

First of all, I would like to express my deepest appreciation to my supervisor Dr. Saikat Biswas. I am very much thankful to him not only for conveying the spirit of research work but also for his help in controlling my emotions and keeping a constant focus on the research work. He created such a nice working environment that stimulates the art of experimental work in the laboratory. He always tried to ignite my mind with clues, that also helped me to find out new ways to solve problems.

I would like to thank Prof. Supriya Das for his encouragement, insightful comments, and valuable suggestions. He always tried to develop knowledge and new ideas. For the simulation work done by me, he guided me in every aspect and explained things in all possible lucid ways. He also helped me with his valuable suggestion and comments during any article writing and preparation of presentations etc.

My deepest gratitude and thanks to Prof. Sanjay Kumar Ghosh for his guidance and teaching during the starting days. He also guided me through all the critical situations and difficulties I faced during my academic tenure.

I am also thankful to Dr. Sidharth Kumar Prasad for his valuable suggestions and comments during the course of the study. He also teaches me the basic CERN-ROOT framework, which is necessary for data analysis and simulation in any High Energy Physics experiment.

It is my great pleasure to thank Dr. Vikas Singhal, VECC, India, who helped me to learn the C++ programming language and also the simulation framework. His patient advice and cool-mindedness impressed me very much.

My special thanks to my colleagues Mr. Sayak Chatterjee, Mr. Prottoy Das, Mr. Abhi Modak, Ms. Debjani Banerjee, and Mr. Asif Bhat and my seniors Dr. Shreya Roy and Dr. Rathijit Biswas.

I am very much indebted to Prof. Probir Roy for his encouragement, support, and guidance. He constantly advises me about scientific progress, academic progress, theoretical developments, etc. He also assisted me correcting errors I made while writing scientific content.

I am thankful to Prof. Subhasis Chattopadhyay, Deputy spokesperson of the CBM experiment and the convenor of the CBM-MuCh project, India, for providing me the opportunity to work on the CBM-MuCh project. His encouragement and many useful suggestions in the course of this work helped me a lot.

I am also thankful to the CBM-Hadron working group for providing the opportunity and support to work with the collaboration and do the simulation.

It is my great pleasure to thank Mr. Subrata Das of Bose Institute for helping me to build the readout of my detector and also for providing the technical support needed by me during this period. Mr. Mohan Das also helped me with any type of construction work. Without their active support and help, it would have been challenging for me to complete this work.

I would like to thank the other people at Bose Institute who wished for a long time and helped me in different ways. Specially thanks to our workshop superintendent Mr. Raju C Paul, head of the technical staff Mr. Dipankar Bera and security staffs of the institute. They are really an asset to the organisation.

I am very much thankful to Mr. Abhishek Seal and Mr. Prasun Singh Roy of VECC IT support for providing me the technical help and support. They have been a substantial source of help and support during these years.

Thanks to my seniors Dr. Rajesh Ganai and Dr. Mitali Mondal, for many fruitful discussions and for making me understand the critical points about the detector.

My special thanks to the project students Mr. Abhisek Roy, Ms. Rituparna Banerjee, Ms. Krishna Nivedita G, Ms. Debonita Saha, Ms. Aayushi Paul, Mr. Subham Jaiswal, Mr. Shivshant Chauhan, Mr. Rajat Paul, Mr. Pranjal Barik, Mr. Shreesh Sahai and Mr. Ayan Dandapat who worked with me in the lab and completed their project work.

Thanks to Mr. Sayan Chakraborty, who did his master's project with RPC in the lab, for helping me at the beginning of my Ph.D. to start taking data at the laboratory.

I would like to thank Dr. Somen Gope, postdoctoral fellow of Bose Institute, for helping me in correcting the thesis, valuable suggestions and also for taking data at the laboratory.

I am thankful to Dr. Sumit Kumar Kundu of IIT, Indore for his help during the software analysis work and to my junior Ms. Rudrapriya Das who helped me in taking some data. I am grateful to my junior Mr. Subir Mandal, who joined recently in our laboratory, for helping me in data taking and all other works in the lab.

I would like to thank Prof. Rajarshi Ray and Prof. Somshubhro Bandyopadhyay of the Physics Department, Bose Institute and Prof. Sibaji Raha, former Director of Bose Institute for their support and valuable discussions.

I would like to acknowledge the Innovation in Science Pursuit for Inspired Research (INSPIRE) unit of Department of Science & Technology (DST), Govt. of India for providing the fellowship and contingency to carry out the work. This work is also partially supported by the CBM-MuCh project from BI-IFCC, DST, Govt. of India.

I also acknowledge Dr. Sascha Vogel of Frankfurt International Graduate School for Science, Germany, for providing financial support at the time of 6^{th} International FAIR School, Italy, which was my first international travel to attend the school.

I am thankful to the organising committee of 15^{th} Pisa Meeting for the financial help to attend the conference. Thanks to the Frontier Detector for Frontier Physics Association for selecting

me for the Young Researcher Grant to attend 15^{th} Pisa Meeting on Advanced Detectors - Edition 2022 and present my work.

I am very much happy to acknowledge the organising committee of 29^{th} International Conference on Ultra-relativistic Nucleus-Nucleus Collisions (Quark Matter 2022) for the financial support for registration to attend the conference.

I thank all the research scholars, past and present of Bose Institute, who helped me in various ways by providing information, study-related discussions, etc.

Since I started working in this field, I have had opportunities to interact with many scholars, scientists, and experts in the field. Through direct and indirect interaction with them, I have learned a lot. I am indeed grateful to them.

I am thankful to the director of Bose Institute Prof. (Dr.) Uday Bandyopadhyay, for providing the facilities and a good environment for the research work at Bose Institute.

Last but not the least, I would like to thank my parents, Mr. Ananda Kumar Sen and Mrs. Nilima Sen, my sister Mrs. Sunanda Dasmahapatra, brother-in-law Mr. Santanu Dasmahapatra, my two nephews Aayog and Sanjog and all my family members, and all relatives for believing in me, for their patience, for their constant support, and for inspiring me, not only to pursue my research work during all these years but also to stand beside me always in the ups and downs of this journey.

Arindam Sen

Abstract of the thesis

The Compressed Baryonic Matter (CBM) experiment at the future Facility for Antiproton and Ion Research (FAIR) in Darmstadt, Germany, will explore the QCD phase diagram at low temperature and moderate to high baryonic density regime. The decay of charmonium (J/ψ), low mass vector mesons ρ^0, ω^0, Φ^0 in the muonic decay channel, *i.e.*, $\mu^+\mu^-$ will be used as a probe to get an idea about the in-medium modifications of the particles. The Muon Chamber (MuCh) at CBM will be used dedicatedly for muon tracking. CBM-MuCh will consist of five absorber layers of thickness 60, 20, 20, 30, and 100 cm, respectively. The first absorber will be made up of 60 cm of carbon. The rest of the absorbers will be made up of iron. In between the absorbers (termed as stations), three active detector layers will be placed. Given the maximum interaction rate of 10 MHz, the expected particle flux on the first two stations of CBM-MuCh will be about 1 MHz/cm^2 and 0.1 MHz/cm^2 and that on the 3^{rd} and 4^{th} stations have been estimated to be 15 kHz/cm^2 and 5.6 kHz/cm^2, respectively, for central Au–Au collisions at 8 AGeV. Triple GEM (Gas Electron Multiplier) detectors will be used in the first two stations to handle high particle rates. We are exploring the possibility of using Resistive Plate Chambers (RPCs) for the 3^{rd} and 4^{th} stations.

Single-gap RPC is one of the very popular gaseous detectors used in high-energy physics experiments nowadays. It is a very fast detector with a low cost of fabrication. The RPCs are usually built using glass or bakelite plates having high resistivity (ρ) $\sim 10^{10}$ - 10^{12} Ω cm.

Several RPC prototypes are built with different grades of indigenous bakelite plates and characterised in detail. Bakelite RPCs are generally fabricated with a linseed oil coating inside to make the inner electrode surface smoother, which helps to reduce the micro discharge probability and also to reduce the surface UV sensitivity dramatically and to effectively protect the bakelite surfaces from the Hydrofluoric Acid (HF), produced by the interaction of fluorine with the water vapour. There is a conventional way to do this linseed oil coating after making the gas gap. In this work, a new technique is introduced to do the linseed oil coating on the bakelite plate before making the gas gap. The detectors are tested using cosmic rays for efficiency, noise rate, time resolution, long-term stability, and radiation hardness in high-rate gamma environments varying different parameters. The detailed study of the development of bakelite RPCs for the CBM-MuCh has been described in this thesis.

In the second part of the thesis, an application of radiation detectors is described. Due to the COVID-19 outbreak and complete nationwide lockdown, the laboratory was closed from the end of March 2020 till the end of May 2020. After the lockdown, although the city was not in its normal state, we still were able to take data on some days. This lockdown has a significant effect on atmospheric conditions in terms of changes in the concentration of air pollutants. We have compared the cosmic ray flux, measured by the coincidence technique using plastic scintillation detectors, before and after the lockdown to observe the apparent change, if any, due to changes in the atmospheric conditions. Measurement of cosmic ray flux is done at Kolkata along with the major air pollutants present in the atmosphere before and after the lockdown.

Declaration

I do hereby declare that the investigation presented in the thesis has been carried out by me under the supervision of Dr. Saikat Biswas. The work is original and has not been submitted earlier as a whole or in part for a degree/diploma at this or any other Institution/University.

Arindam Sen

List of Publications

Thesis is based on the following publications

Journals

- **Characterisation of a new RPC prototype using conventional gas mixture.**
  Authors: **A. Sen**, S. Chatterjee, S. Das, S. Biswas
  Published in **Nuclear Inst. and Methods in Physics Research, A 1045 (2023) 167572**
  e-Print: **arXiv:** 2206.04259 [physics.ins-det, hep-ex]

- **A new technique of linseed oil coating in bakelite RPC and the first test results.**
  Authors: **A. Sen**, S. Chatterjee, S. Das, S. K. Ghosh, S. Biswas
  Published in **Nuclear Inst. and Methods in Physics Research, A 1024 (2022) 166095**
  e-Print: **arXiv:** 2108.06923 [physics.ins-det, hep-ex]

- **Cosmic ray flux and lockdown due to COVID-19 in Kolkata – Any correlation?**
  Authors: **A. Sen**, S. Chatterjee, S. Roy, R. Biswas, S. Das, S. K. Ghosh, S. Biswas
  Published in **Pramana - J Phys 95, 64 (2021)**
  e-Print: **arXiv:** 2010.06648 [hep-ex, astro-ph.HE, physics.ao-ph]

- **Characterisation of an RPC prototype with moderate resistivity plates using tetrafluoroethane ($C_2H_2F_4$).**
  Authors: **A. Sen**, S. Chatterjee, S. Roy, S. Biswas, S. Das
  Published in **2020 JINST 15 C06055 DOI: 10.1088/1748-0221/15/06/C06055**
  e-Print: **arXiv:** 2004.05469 [physics.ins-det, hep-ex]

National Conference Proceedings & Internal Notes

- **Performance studies of bakelite RPC with new technique of linseed oil coating.**
  Authors: **A. Sen**, S. Chatterjee, S. Das, S. K. Ghosh, S. Biswas
  CBM Progress report 2021, 106. ISBN: 978-3-9822127-0-8 [DOI: 10.15120/GSI-2022-00599]

- **Identification of Hadrons using PID framework.**
  Authors: S. K. Kundu, **A. Sen**, S. Biswas, A. Roy, S. Das
  CBM Progress report 2021, 198. ISBN: 978-3-9822127-0-8 [DOI: 10.15120/GSI-2022-00599]

- **Development and issues of bakelite RPC.**
  Authors: **A. Sen**, S. Chatterjee, S. Das, S. K. Ghosh, S. Biswas
  Proceedings of the DAE-BRNS Symposium on Nuclear Physics. Volume 64 (2019), 996-997.

- **Implementation of Electronic FEB Id and channel Id for MUCH.**
  Authors: **A. Sen** and V. Singhal
  CBM Progress report 2019, 75. ISBN: 978-3-9815227-8-5 [DOI: 10.15120/GSI-2020-00904]

- **Development of RPC with low resistive material for CBM-MUCH.**
  Authors: S. Chakraborty, **A. Sen**, S. Chatterjee, S. Roy, A. Roy, S. Biswas, S. Das, S. K. Ghosh, S. K. Prasad, and S. Raha
  CBM Progress report 2018, 67. ISBN: 978-3-9815227-6-1 [DOI: 10.15120/GSI-2019-01018]

Other publications

Journals

- **Charging-up effect and uniformity study of a single mask triple GEM detector.**
  Authors: S. Chatterjee, **A. Sen**, S. Das, S. Biswas
  Published in **Nuclear Inst. and Methods in Physics Research, A 1049 (2023) 168110**
  e-Print: **arXiv:** 2206.10876 [physics.ins-det, hep-ex]

- **Effect of relative humidity on the long-term operation of a single mask triple GEM chamber.**
  Authors: S. Chatterjee, **A. Sen**, S. Das, S. Biswas
  Published in **Nuclear Inst. and Methods in Physics Research, A 1046 (2023) 167747**
  e-Print: **arXiv:** 2206.04051 [physics.ins-det, hep-ex]

- **Visual investigation of possible degradation in GEM foil under test.**
  Authors: S. Chatterjee, **A. Sen**, S. Das, S. Biswas
  Published in **Nuclear Inst. and Methods in Physics Research, A 1045 (2023) 167573**
  e-Print: **arXiv:** 2206.04052 [physics.ins-det, hep-ex]

- **Study of charging-up effect for a single mask triple GEM detector.**
  Authors: S. Chatterjee, **A. Sen**, S. Das, S. K. Ghosh, S. Biswas
  Published in **Nuclear Inst. and Methods in Physics Research, A 1014 (2021) 165749**
  e-Print: **arXiv:** 2107.00890 [physics.ins-det, hep-ex]

- **Stability study and time resolution measurement of Straw Tube detectors.**
  Authors: S. Roy, S. Jaiswal, S. Chatterjee, **A. Sen**, S. Das, S. K. Ghosh, S. Raha, V. M. Lysan, G. D. Kekelidze, V. V. Myalkovsky, S. Biswas
  Published in **Pramana - J Phys 95, 50 (2021)**
  e-Print: **arXiv:** 2007.12547 [physics.ins-det, hep-ex]

- **Study of charging up effect in a triple GEM detector.**
  Authors: S. Chatterjee, **A. Sen**, S. Roy, K. Nivedita G, A. Paul, S. Das, S. Biswas
  Published in **2020 JINST 15 T09011**
  e-Print: **arXiv:** 2007.11444 [physics.ins-det, hep-ex]

- **Long term stability study of triple GEM detector using different Argon based gas mixtures: an update.**
  Authors: S. Chatterjee, S. Roy, **A. Sen**, S. Chakraborty, S. Biswas, S. Das, S. K. Ghosh, S. K. Prasad and S. Raha
  Published in **2020 J. Phys.: Conf. Ser. 1498 012037**
  e-Print: **arXiv:** 2007.12547 [physics.ins-det, hep-ex]

National Conference Proceedings & Internal Notes

- **Charging-up effect in single mask triple GEM chamber.**
  Authors: S. Chatterjee, **A. Sen**, S. Das, S. K. Ghosh, S. Biswas
  CBM Progress report 2021, 198. ISBN: 978-3-9822127-0-8 [DOI: 10.15120/GSI-2022-00599]

- **Study of charging up effect in GEM detector.**
  Authors: K. Nivedita G, A. Paul, S. Chatterjee, S. Roy, **A. Sen**, S. Biswas, S. Das
  Proceedings of the DAE-BRNS Symposium on Nuclear Physics. Volume 64 (2019), 976-977

- **R&D of Straw Tube detector for High Energy Physics experiments.**
  Authors: S. Roy, S. Jaiswal, S. Chatterjee, **A. Sen**, S. Biswas, S. Das, S. K. Ghosh, S. Raha, V. M. Lysan, G. D. Kekelidze, V. V Myalkovsky
  Proceedings of the DAE-BRNS Symposium on Nuclear Physics. Volume 64 (2019), 990-991

Contents

List of Figures

List of Tables

Abbreviation

AFM Atomic Force Microscopy

APPA Atomic, Plasma Physics and Applications

CALIC Calorimeter for Linear Collider Experiment

CBM Compressed Baryonic Matter

CERN European Organization for Nuclear Research

CR Collector Ring

DCM-QSM-SMM Dubna Cascade Model, Quark-Gluon String Model and Statistical Multi-fragmentation Model

DISC Discriminator

ECAL Electromagnetic Calorimeter

FAIR Facility for Antiproton and Ion Research

FWHM Full Width at Half Maximum

GEM Gas Electron Multiplier

GWP Global Warming Potential

HEP High Energy Physics

HESR High Energy Storage Ring

HF Hydrofluoric Acid

HFO Hydro Fluoro Olefin

HV High Voltage

ICAL Iron Calorimeter

INO India Based Neutrino Observatory

K.E. Kinetic Energy

LED Leading Edge Discriminator

LHC Large Hadron Collider

LMVM Low Mass Vector Meson

MAPD Micro Pixel Avalanche Photodiode

MAPMT Multi Anode Photo Multiplier Tubes

MCA Multi Channel Analyser

MIP Minimum Ionising Particle

MPGD Micro Pattern Gaseous Detectors

MRPC Multi Gap RPC

MuCh Muon Chamber

MVD Micro Vertex Detector

MWPC Multi Wire Proportional Counter

NADIR Neutron Antineutron Doublet Investigation by Reactor

NESR New Experimental Storage Ring

NIM Nuclear Instrumentation Module

NUSTAR Nuclear Structure, Astrophysics and Reactions

PANDA antiProton ANnihilation at DArmstadt

PC Personal Computer

PET Positron Emission Tomography

PMT Photo Multiplier Tube

PPC Parallel Plate Chamber

PSD Projectile Spectator Detector

QCD Quantum Chromodynamics

QGP Quark Gluon Plasma

RESR Recuperated Experimental Storage Ring

RH Relative Humidity

RPC Resistive Plate Chamber

RICH Ring Imaging Cherenkov Detector

STS Silicon Tracking Station

TAC Time to Amplitude Converter

TOF Time of Flight

TRD Transition Radiation Detectors

UrQMD Ultra relativistic Quantum Molecular Dynamics

WLS Wavelength Shifting

Chapter 1

Introduction

The Facility for Antiproton and Ion Research (FAIR) at Darmstadt, Germany, is one of the largest international accelerator facilities [1], currently under construction for research on atomic and plasma physics (APPA : Atomic, Plasma Physics and Applications [2]), nuclear and astrophysics (NUSTAR : Nuclear Structure, Astrophysics and Reactions [3]), basic physics on various areas around the weak and strong forces, exotic states of matter and the structure of hadrons (PANDA : antiProton ANnihilation at DArmstadt [4]) and the evolution of the universe from the Big Bang to the present (CBM : Compressed Baryonic Matter [5]) [6].

CBM experiment will mainly focus on the physics of Quark Gluon Plasma (QGP) which was formed in a few microseconds after the Big Bang and covered the whole early universe. In the Standard Model of particle physics, Quantum Chromodynamics (QCD) is the tool that helps us to explain the strong interaction force. Quarks and Gluons are the fundamental particles in QCD. After the fireball expansion and deconfinement of matter, now all the things got fridged and formed hadronic matter.

CBM is a fixed target experiment at FAIR that will use proton and heavy ion beams to explore the QCD phase diagram at low temperature and moderate to high baryonic density regime. Also, one of the main questions that CBM will explore is how the neutron star is formed. The equation of state will address those questions. At moderate temperatures and densities, nucleons are excited to short-lived states that decay by the emission of meson. Due to the large mass of the charm quarks, they are expected to be formed at the early stage of the collision and then hadronise to form the quarkonium. Detection of charmonium (J/ψ) via their

di-lepton decay channel ($J/\psi \rightarrow e^+ + e^-$ / $\mu^+ + \mu^-$) is one of the unique opportunities at CBM because no data is available till date in the heavy-ion sector below the topmost SPS energy of 158 GeV. The low mass vector mesons (LMVM) ρ, ω, Φ will also be formed primarily via $\pi\pi$ annihilation. After that, they will decay into meson or in the pair of leptons. The leptonic decay channel is four times more probable than the others. Since the leptons do not have any colour charge, they do not take part in strong interaction and hence are one of the most important probes of the QGP phase [5]. Diagnostic probes of the dense stage of the fireball, such as multi-strange baryons, dilepton pairs, and charmed particles, will also be measured for the first time by the CBM experiment in the beam energy range of 2 to 40 AGeV. In order to produce high statistics data even for particles with the lowest production cross-sections, the CBM experiment is designed to run at an average interaction rates of 100 kHz to 1 MHz.

One of the biggest challenges of CBM is to detect the low momentum muon pairs from high particle density. The tracking of muons will be done by the tracking detectors placed in the Muon Chamber (MuCh) subsystem. The MuCh subsystem will be placed downstream of the Silicon Tracking Station (STS). It will track particles and reconstruct the momentum dependent muon paths. MuCh will consist of several iron absorbers of varying thicknesses for hadron absorption. In between two absorber layers, there will be three active detector layers called stations. In the first two stations of CBM-MuCh, Gas Electron Multiplier (GEM) detectors will be used because of their high rate handling capability. Resistive Plate Chambers (RPC) are one of the options for the 3^{rd} and 4^{th} stations [7, 8].

Single gap Resistive Plate Chamber (RPC) is one of the most widely used detectors for triggering and tracking in High Energy Physics (HEP) experiments for its high efficiency and good time resolution. RPC has been considered in the CBM experiment both for muon detection in MuCh and for precise time of flight measurement by the Time of Flight (TOF) detector. In MuCh, the option is a single-gap bakelite RPC, whereas, in TOF, multi-gap glass RPCs will be used.

RPC is a gas-filled detector made up of high resistive (bulk resistivity $\sim 10^{10}$ - 10^{12} Ω cm) plates as electrodes. Typical electrode materials are glass or bakelite. Since the electrodes are highly resistive, it helps to contain the discharge created by the passage of a charged particle or

ionizing radiation in a gas volume. The typical time resolution of a single gap RPC is $\sim$ 1 - 2 ns [9, 10]. Since RPC has a very good time resolution, it is suitable as a tracking detector.

For RPC, there are two modes of operation. One is the streamer mode (gain $> 10^8$) and the other is the avalanche mode (gain $\ll 10^8$). The mode of operation depends on the used gas and applied voltage. For high-rate operation, the option is the avalanche mode. In the avalanche mode of operation mixture of Tetrafluroethene ($C_2H_2F_4$), Iso-butane (i-C_4H_{10}), Sulphur Hexafluoride (SF_6) gas is commonly used. Further, Argon based gases are used in the streamer mode of operation.

However, the most significant issue of RPC is its low particle rate handling capability. Nowadays, the RPC detector can handle particle rates of about $\sim$ 5-8 kHz/cm^2, but in the CBM-MuCh, RPC is supposed to handle a rate $\sim$ 15 kHz/cm^2 in the 3^{rd} station and $\sim$ 5.6 kHz/cm^2 in the 4^{th} station for 8 AGeV central Au-Au collision. The main goal of this thesis is to design and characterise the single gap bakelite RPC to be used in the CBM experiment.

1.1 FAIR SIS100

The FAIR facility was proposed in the year 2001. The SIS100 ring accelerators will be positioned in a tunnel 17 m below ground level in this facility. The accelerators will have a $\sim$ 1100 m circumference, covering almost 7 kilometres in a single rotation. The ion beam will first pass through the existing UNILAC and SIS18 accelerator facility. The length of UNILAC is 120 meters, which can accelerate the particles to $\sim$ 20 percent of the speed of light. The circumference of SIS18 is 216 meters and it can accelerate the particle to $\sim$ 90 percent of the speed of light. The beam will be injected into the SIS100 synchrotrons in the next step for further acceleration and the accelerated beam will then go to the CBM cave. The bending power (B $\times$ r) (also known as magnetic rigidity) generated by the dipole magnets plays a significant role in determining the available beam kinetic energy per nucleon [11, 12]. The governing equation is as follows:

$$E/A = \sqrt{(0.3 \times B \times r \times Z/A)^2 + m^2} - m \tag{1.1}$$

where Z and A are the charge and the mass number of the ion respectively. m is the mass of the nucleon. B is the magnetic field due to the dipole magnet and r is the radius of curvature [13].

The SIS100 (beam rigidity, B × r = 100 Tm) synchrotron is capable of producing the primary beams of protons up to 29 GeV, Au up to 11 AGeV, 14 AGeV for Ca and nuclei with Z/A = 0.5 up to 14 AGeV. The maximum achievable energy with Uranium (U) is 10.7 AGeV for SIS100. Figure 1.1 shows how FAIR is structured. The extracted beam can produce up to 10^9 Au ions per second in the CBM cave.

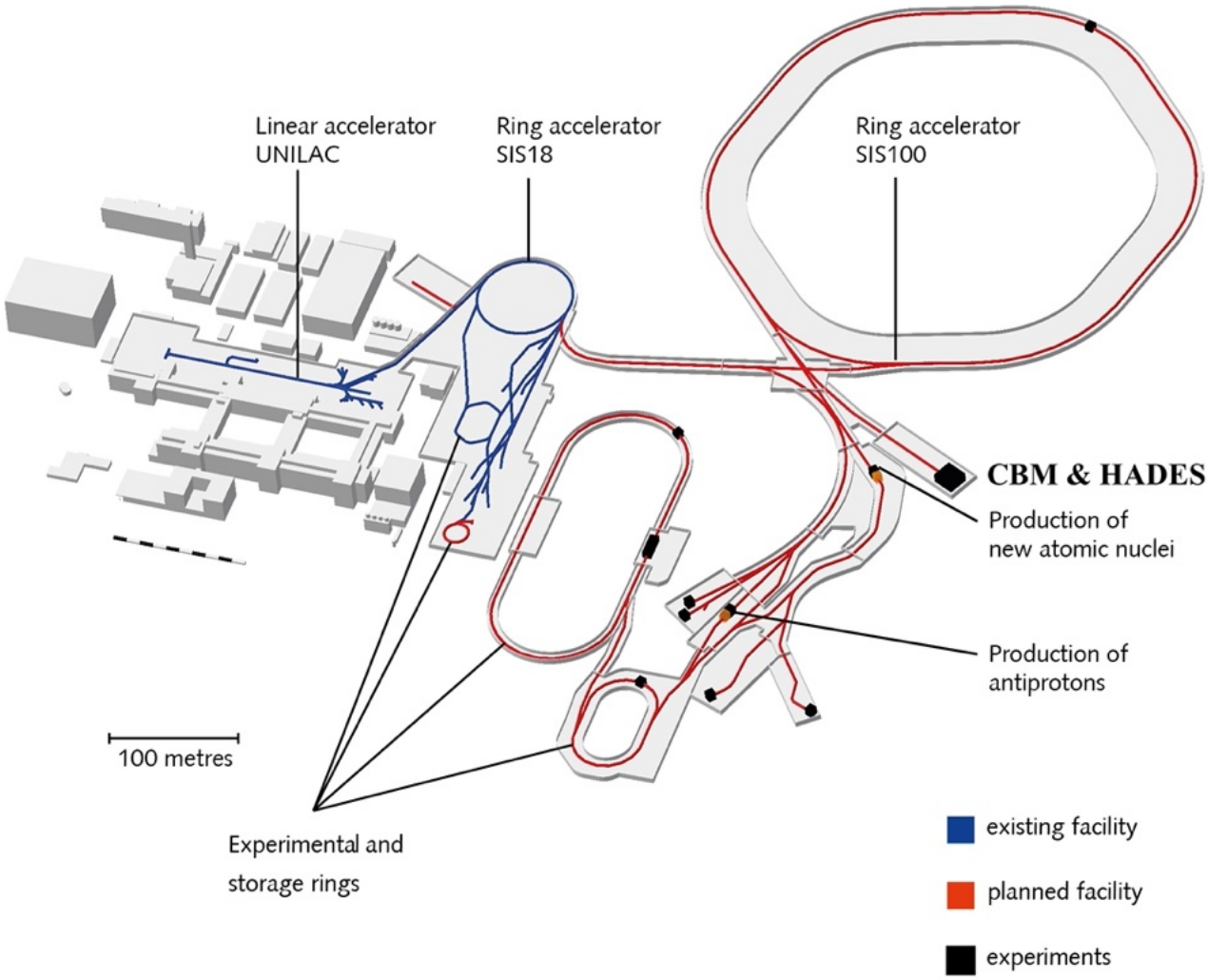

Figure 1.1: The layout of the FAIR SIS100 accelerator ring. Blue, red, and black indicate the existing GSI facility, upcoming synchrotron facility, and the experimental sites, respectively. The picture is taken from Ref. [14]

In the FAIR facility, CBM will be capable of measuring event-by-event fluctuations of conserved quantities (like baryons, strangeness , net-charge, etc.) in heavy-ion collisions with high precision with the compatible beam energies. The excitation function of yields, spectra, and collective flow of strange particles, charmed particles, and leptons will be studied in this energy range [13, 15].

The accelerator is now under construction. The Figure 1.2 depicts the current status of the construction site as of April 2023.

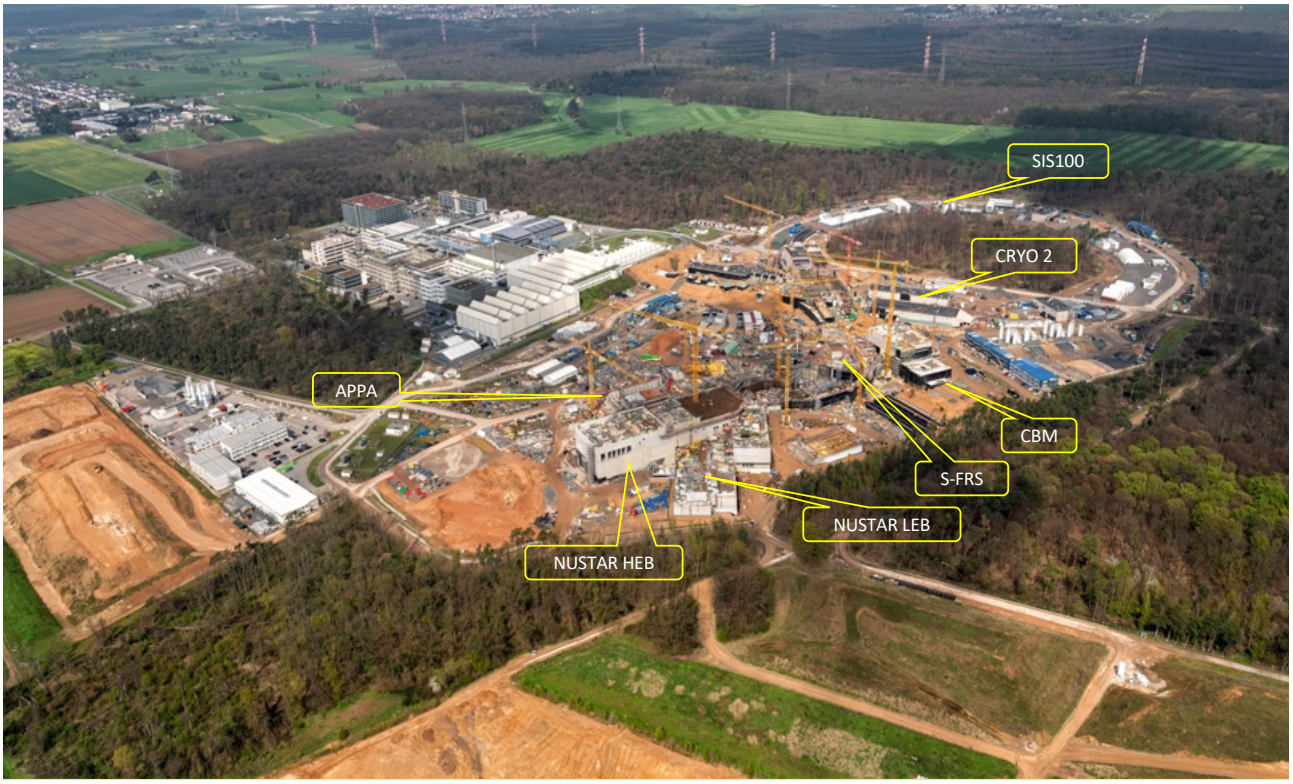

Figure 1.2: The photograph of construction site of FAIR SIS100 accelerator ring. The picture is taken from Ref. [16]

1.2 CBM experiment

The interaction rate in the CBM experiment will be very high $\sim$ 10 MHz as shown in Figure 1.3. The SIS100 accelerator at the FAIR facility will deliver high-intensity beams with maximum intensities of 10^9 ions/s up to Au ions, in the beam kinetic energy range of 2 AGeV to 11 AGeV. Proton beams of intensities up to 10^{11} /s will also be available with a maximum beam kinetic

energy of 29 GeV. This high interaction rate will enhance the possibilities to measure the rare probes with high statistics [13].

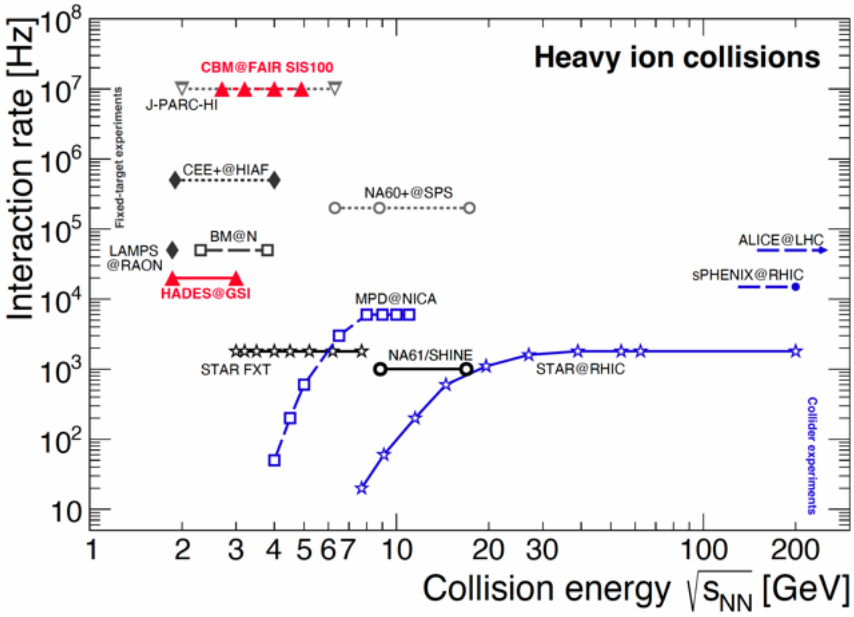

Figure 1.3: Comparison of the highest interaction rates of different present and future heavy-ion experiments. Update (2021) [17]

The high baryon density and the low-energy region of the QCD phase diagram is yet to be explored in heavy-ion collisions with such high interaction rates. This challenging job will be done by the CBM experiment. The fundamental questions such as the equation of state and the relevant degrees of freedom at high net-baryon densities, the existence of exotic QCD phases, in-medium modifications of the hadrons, indications of chiral symmetry restoration, the existence of the heavy multi-strange hypernuclei will be explored by the CBM experiment [17, 18, 19].

The event-by-event fluctuations of the conserved quantities like baryon number, strangeness, charm and electrical charge can be measured by the CBM experiment. The higher-order moments of these distributions are expected to show more sensitivity to the phase transition and matter structure near the critical point [20, 21].

The di-leptons are emitted at the early stages of the produced fireball and carry undistorted information about the medium properties. This is possible because they do not interact strongly, being electromagnetic in nature. The temperature of the fireball, which is produced in heavy-ion

collisions, can be achieved from the invariant mass spectra of di-leptons. Medium modification of the vector mesons, the lifetime of the fireball can also be determined by the di-leptonic probe. In the CBM experiment, there is a unique opportunity to explore di-lepton measurement and measurement of excitation function [22, 23].

Hadrons containing strange quarks will be produced in heavy-ion collisions in the CBM experiment. The yields of the strange baryons is correlated with the density of the fireball produced. In a purely hadronic scenario, the heavier multi-strange baryons, *e.g.* Ω, Ξ, can be produced in sequential collisions of lighter strange hadrons such as kaons and lambdas. CBM will thus measure the excitation function of multi-differential yields, flow, and fluctuations of strange hadrons, multi-strange baryons for different collision centralities [24, 25].

Charmed particles are generated in the primary stages of heavy-ion collisions. Different charmonium states can be suppressed due to Debye screening and this phenomenon is called charmonium suppression. In the experiments like RHIC and LHC, this phenomenon is observed earlier. With the CBM experiment at FAIR, in the SIS100 energy regime, the charm production will be studied at the beam energies close to the kinematic production threshold. 300 J/ψ will be measured for central Au+Au collisions energy at 10 AGeV as per one week of data taking, as expected. [26, 27].

1.3 CBM detector system overview

In the CBM experiment, different detector subsystems will be used to identify both hadrons and leptons. The main detector setup of the CBM experiment will consist of a dipole magnet and several detector subsystems such as Beam Monitor Detector System (BMON), Micro-Vertex Detector (MVD), Silicon Tracking Station (STS), Ring Imaging Cherenkov Detector (RICH), Muon Chamber (MuCh), Transition Radiation Detectors (TRD), Time of Flight (TOF) detectors, Forward Wall. In the CBM setup, MuCh and RICH are complementary to each other. The MuCh will be used for the detection of di-muon, whereas RICH will be dedicatedly used for the detection of di-electrons produced in the decay of charmonium and LMVM. When RICH is in operation, MuCh will be in the parking position and vice versa.

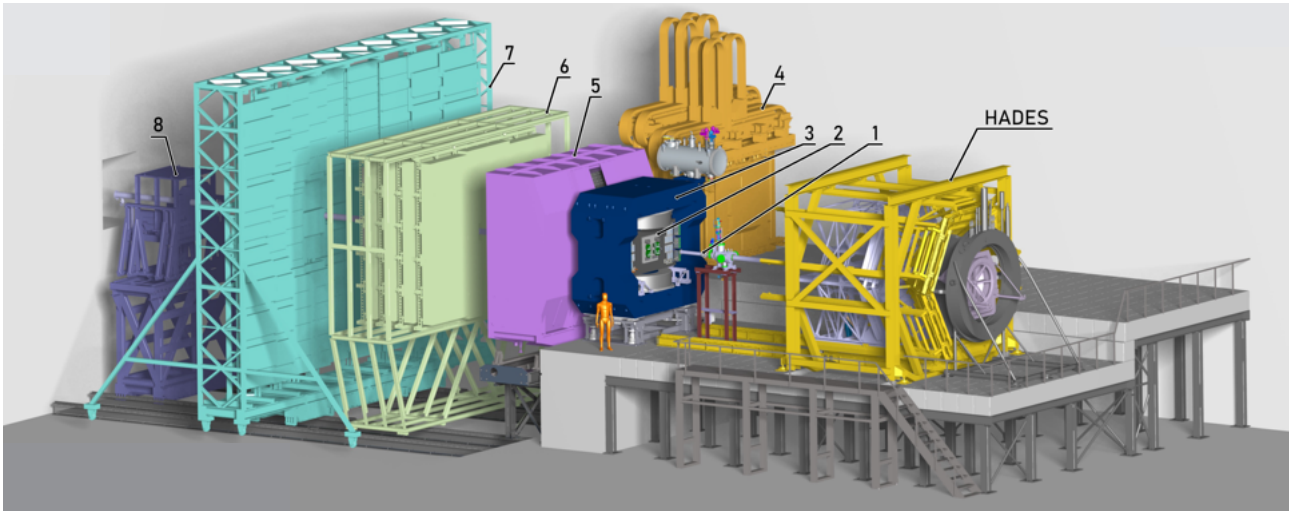

Figure 1.4: A combined experimental setup of CBM & HADES detector system. The CBM setup consists of: 1. Beam MONitor Detector (BMON), 2. Micro Vertex Detector (MVD) / Silicon Tracking System (STS), 3. Superconducting Dipole Magnet, 4. Muon Chamber (MuCh), 5. Ring Imaging CHerenkov Detector (RICH), 6. Transition Radiation Detector (TRD), 7. Time of Flight Detector (TOF), and 8. Forward Spectator Detector. The picture is taken from Ref. [28]

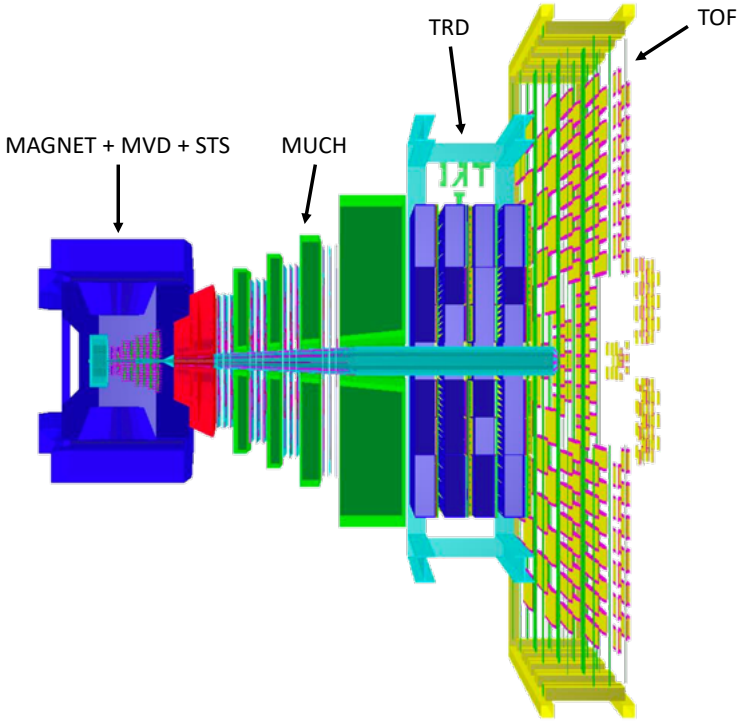

Figure 1.5: Cross-sectional view of detectors arrangements

In CBM, rare probes and multi-strange hyperons, hypernuclei, and vector mesons will be identified at high precision with large statistics. For large statistics, new self-triggered readout electronics and high-speed data acquisition systems will be used [13, 29]. Both the electronics and detectors will be radiation hard to run the experiment successfully. The rare probes will be identified from large track densities. Figure 1.4 (with RICH in beam line) and Figure 1.5 (with MuCh in beam line) show the experimental setup of the CBM experiment in two views.

1.3.1 Beam Monitor Detector System (BMON)

The purpose of Beam MONitor detector system (BMON) is beam monitoring and time-zero (T0) measurement for the CBM experiment. Prototype sensor based on poly-crystal (pc) chemical vapour deposition (CVD) diamond technology (pcQVD) had been fitted into the target chamber's vacuum vessel within mCBM at the 2022 beam campaign. The 1×1 cm^2 diamond sensor's metallisation is divided into 16 vertically and horizontally aligned strips on each side. With up to 4×10^8 Au-ions per spill, the new T0 diamond counter was successfully operated, offering steady T0 information with great time-resolution in the mCBM data stream in addition to highly helpful beam monitoring [30].

1.3.2 Dipole magnet

The superconducting dipole magnet (as shown in Figure 1.6) will be used to provide the bending power to the MVD and STS detectors. The target, STS and MVD are placed in the large gap of the magnet. Charged particle trajectories will bend under the magnetic field, and from the bending, the momentum will be determined.

The magnet will have a magnetic field intensity of 1 Tm which will be used for good momentum resolution [31]. GSI experts have refined the design of magnet now, and the new magnet will be used in the experiment. The aperture of the magnet enlarged to 1470 $\times$ 3300 mm^2 [28].

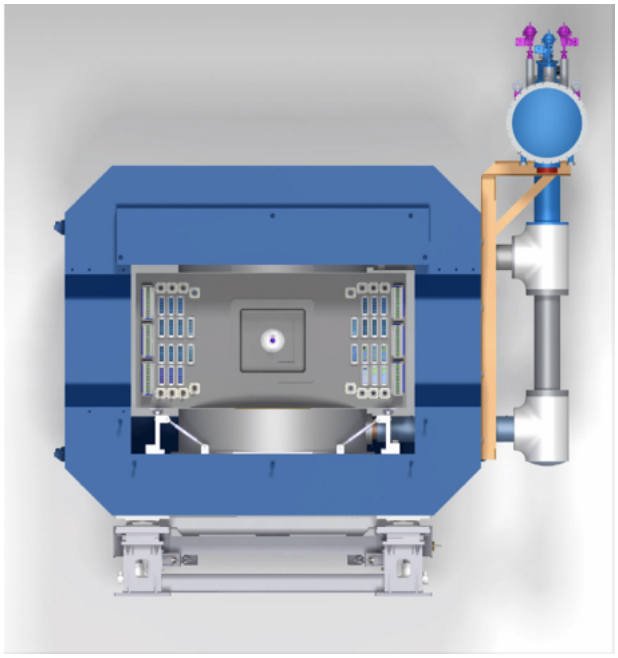

Figure 1.6: The schematic view of the dipole magnet that will be used in the CBM experiment. Figure is taken from Ref. [28].

1.3.3 Micro Vertex Detector (MVD)

The MVD detector (as shown in Figure 1.7) system consists of four layers of monolithic active pixel sensors (MAPS) located at 5(8) cm to 20 cm downstream of the target in the vacuum. The actual position will depend on the needs of a specific run. The decay vertices of open charm particles and weakly decaying charged hyperons will be determined by the MVD detector. A very low material budget will also reduce multiple scattering. These will be done with Monolithic Active Pixel Sensors (MAPS). The MAPS pixel size will be between 18×18 μm^2 and 20×40 μm^2. Position resolution $\sigma = 3.5$ - 6 μm can be achieved. With this vertex detector geometry, secondary vertices can be determined at a precision of about 50 - 100 μm along the beam axis [32].

The total thickness of the detector will be 300 - 500 μm silicon equivalent for sensors and support structures, that depends on the size of the stations.

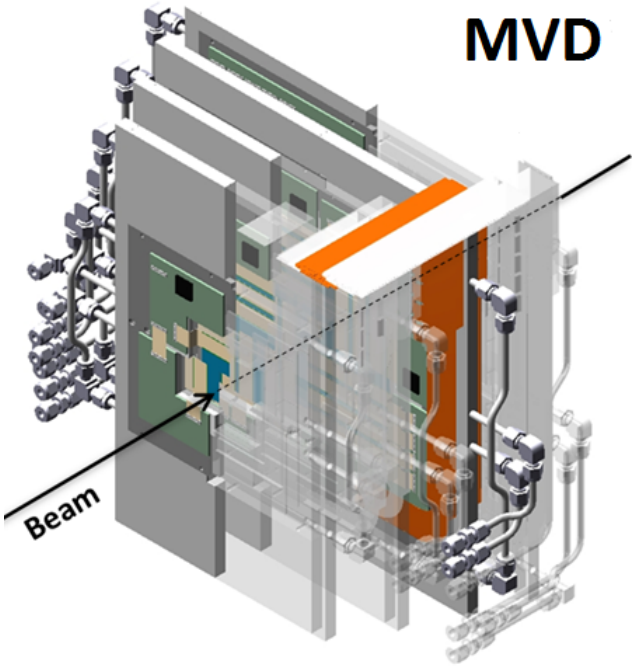

Figure 1.7: 4 layered MVD detector design of the CBM experiment, made of monolithic active pixel sensors

1.3.4 Silicon Tracking System (STS)

The main goal of the STS detector system in CBM is the track reconstruction and momentum determination for the charged particles. The STS (as shown in Figure 1.8) will consist of 8 tracking detector layers of silicon micro-strip sensors [30]. The performance is improved by using the low material budget of the stations and thereby reducing multiple scattering. With this detector, the momentum resolution can be achieved better than 2% in the 1 Tm dipole magnetic field [33]. The maximum non-ionising dose closest to the beam line does not exceed 1×10^{14} n_{eq} cm^{-2} for the sensors. According to the latest simulation, a new STS-3+5 modular design (geometry: v22c) has been adopted. The distance from the target to the first three stations is kept the same, as is the 10.5 cm pitch between successive stations. But, due to the additional supporting C-frame that will be in between the STS-3 and STS-5 blocks, an additional 2 cm of extra space is needed compared to the previous geometry (v21e). Finally, this STS-3+5 geometry will be an overall 2 cm longer in z length [34].

The cooling is the most important part of STS to maintain the performance of the detector. The cooling system consists of two cooling agents: perfluor (2-methyl-3-pentanon), also known

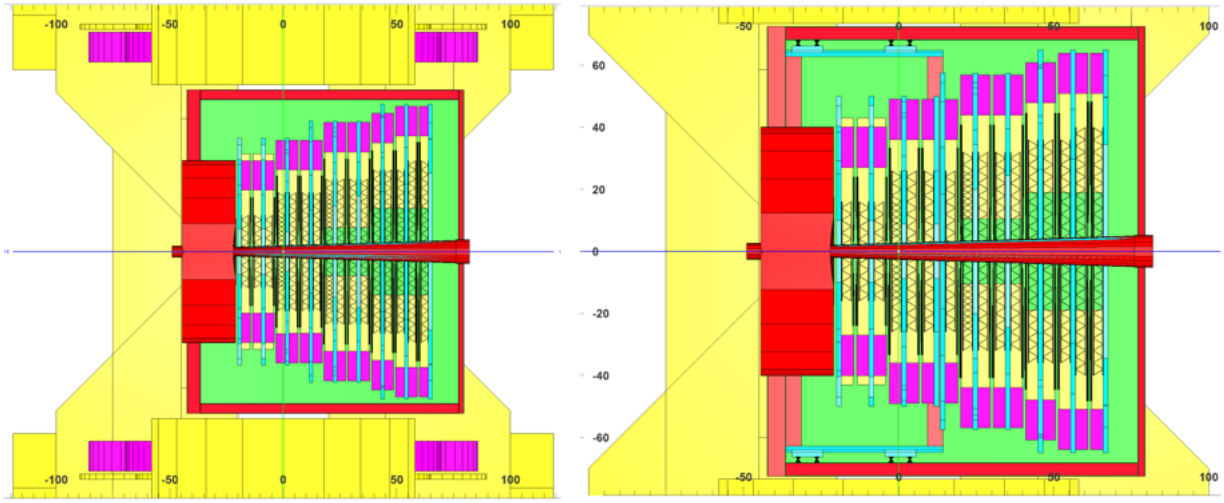

(a) (b)

Figure 1.8: The schematic view of STS for (a) v21e geometry, and (b) v22c geometry. Pictures are taken from Ref. [34]

as dry water or 3M NOVEC 649 with 7.5 kW rated power and a rated temperature of -40 °C), and dry air (rated power 300 W, rated temperature -10 °C). The liquid coolant will be used to cool the FEBs, and the dry air will be used to cool the silicon sensors.

1.3.5 Ring Imaging Cherenkov Detector (RICH)

With the RICH detector setup (as shown in Figure 1.9), electrons will be identified for momenta up to $\sim$ 8 - 10 GeV/c. It can also suppress the pion below 10 GeV/c momentum range, assuming that pions can be separated from electrons up to 90% of the maximum Cherenkov opening angle. RICH will be positioned behind the dipole magnet about 1.6 m downstream of the target. RICH will have a 1.7 m long gas radiator and two arrays of mirrors, the photon detector planes. The gas radiator element will be CO_2, which has refractive index n = 1.00045 (T = 0 °C, p = 1 atm). The Cherenkov radiation will be reflected by mirrors with Al+MgF_2 reflective coating built from 72 mirror tiles with a curvature of 3 m radius. The photo-detector plane where photons will be reflected will be built from Multi-Anode Photo Multiplier Tubes (MAPMT) (*e.g.* H8500 from Hamamatsu) and will be shielded from the magnetic field. Depending on the final magnetic field of the CBM dipole magnet, the photon detectors might still have to move upwards, which can be achieved by tilting the mirrors by up to 15° [35].

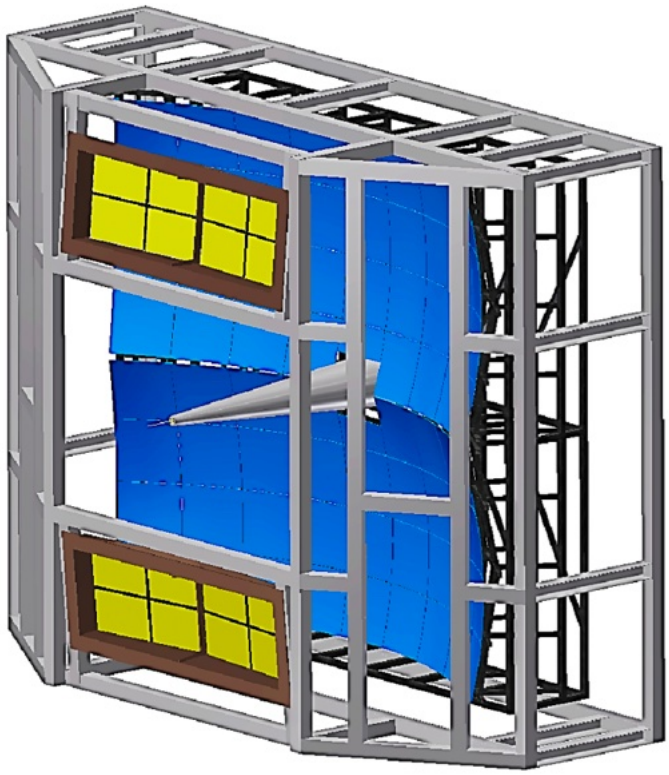

Figure 1.9: RICH detector setup for the CBM experiment dedicatedly designed for the electron identification [36].

1.3.6 Muon Chamber System (MuCh)

The Muon Chamber (MuCh) at the CBM experiment is dedicatedly designed to track the di-muons coming from the decay of LMVMs and charmonium. The schematic of the di-muon measurement setup at CBM (SIS100) is shown in Figure 1.10.

The MuCh will consist of several hadron absorbers to reduce the hadronic backgrounds. According to the latest geometry, MuCh consists of an absorber of 28 cm low-density graphite (density 1.78 g/cm^3) and 30 cm concrete (density $\sim$ 2.3 g/cm^3) combination and after that there will be three iron absorbers of thickness 20 cm, 20 cm, 30 cm respectively. Between two absorbers, there will be active detectors called stations for the detection of muons. After the first absorber, *i.e.* in the first station, three triple GEM detectors will be placed [37, 38, 39, 40, 41, 42, 43, 44, 45, 46, 47, 48, 49, 50, 51, 52]. The second station will also be equipped with triple GEM detectors but have a larger size. Single gap RPC detector is

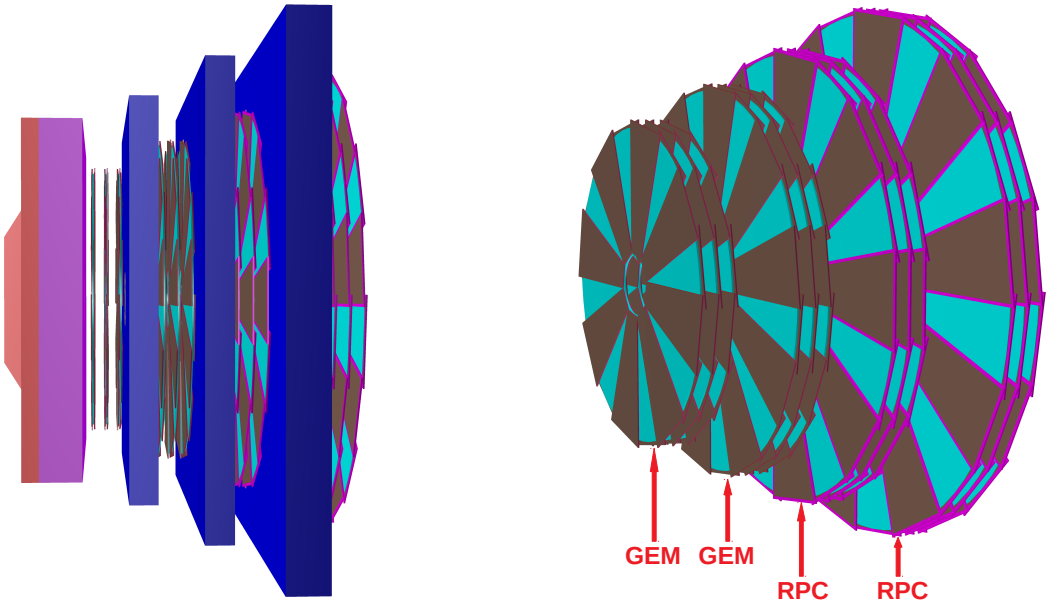

(a) (b)

Figure 1.10: Simulated setup of much subsystem (a) Setup for detectors and absorbers, (b) Detectors arrangements

proposed for the 3^{rd} and 4^{th} stations [53]. Finally, there will be a 100 cm thick iron absorber, specifically for the J/ψ measurement [15]. The particle rates will be $\sim$ 15 kHz/cm^2 and $\sim$ 5.6 kHz/cm^2 respectively at the 3^{rd} and 4^{th} stations for 8 GeV per nucleon central Au-Au collision [54]. There are many high-energy physics experiments dedicated to the muon detection, but the uniqueness of this MuCh detector system is that the total absorber is sliced and the detectors are placed in between the absorbers. Therefore one can identify track depending on the momentum. Using this technique, the resolution of low momentum identification is improved. The detection of low momentum muons in high efficiency is the basic criteria for reconstruction of the low mass vector mesons in the muon chambers.

1.3.7 Transition Radiation Detector (TRD)

There will be three detector layers in each station of TRD out of the three stations. They will serve the purpose of identification of electrons and positrons with momentum P $>$ 1.5 GeV/c. Identification of charged particles via their specific energy loss will be done. Thus the TRD, in addition, will also provide valuable information for the measurements of nuclear fragments.

Three stations will be located at $\sim$ 5 m, 7.2 m and 9.5 m, respectively, downstream of the target. The total active detector area will be $\sim$ 600 m^2. The expected particle rate at a distance of 5 m from the target is $\sim$ 100 kHz/cm^2 for 10 MHz minimum bias Au-Au collisions at 25 AGeV. In the central collision, particle density will reach up to $\sim$ 0.05/cm^2.

The main detector is Multi-Wire Proportional Counter (MWPC) with a radiator, and the active gas medium is Xe/CO_2. Each second transition radiation layer is rotated by 90°. Pion suppression factor will be well above 10 at electron identification efficiency of $\sim$ 90% [55]. The shape of the readout pads will be rectangular, and the resolution will be 300 - 500 μm across and 3 - 30 mm along the pad. The TRD detector configuration for the CBM experiment is shown in Figure 1.11.

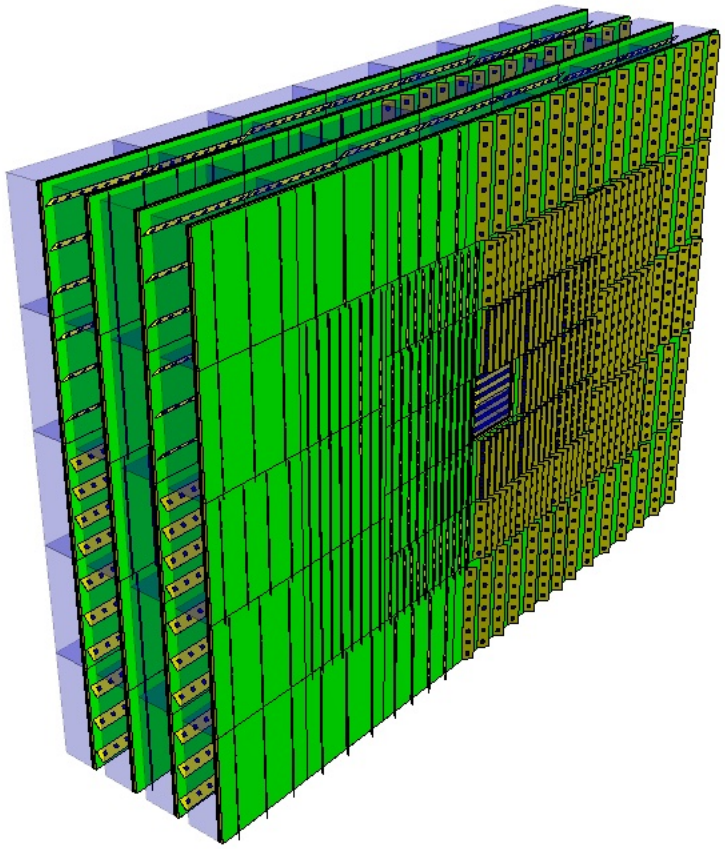

Figure 1.11: TRD detector configuration for the CBM experiment. For the SIS100 geometry, only one station consisting of three detector layers will be used between the STS and TOF wall [36].

1.3.8 Time of Flight Detector (TOF)

Several Timing Multi-gap Resistive Plate Chambers (MRPCs) will be used in a modular array for the measurement of the arrival time of charge particles that will cover the polar angles from 2.5° - 25°. The charge hadrons will be identified after having matched the TOF hit with the corresponding STS track. This setup will achieve a time resolution of 80 ps. To distinguish kaons from the pions and protons, it is also necessary to achieve at least 95% efficiency of the individual MRPC module.

The TOF wall will cover an active area of 120 m^2 and will be located between 6 m to 10 m downstream from the target of the SIS100 setup, depending on the physics goal. The hit rate will go up to 25 kHz/cm^2 in the inner zone and 10 kHz/cm^2 in the outer zone with TOF wall placed at a distance for the minimum-bias events [56]. Design of the CBM TOF detector system is shown in Figure 1.12.

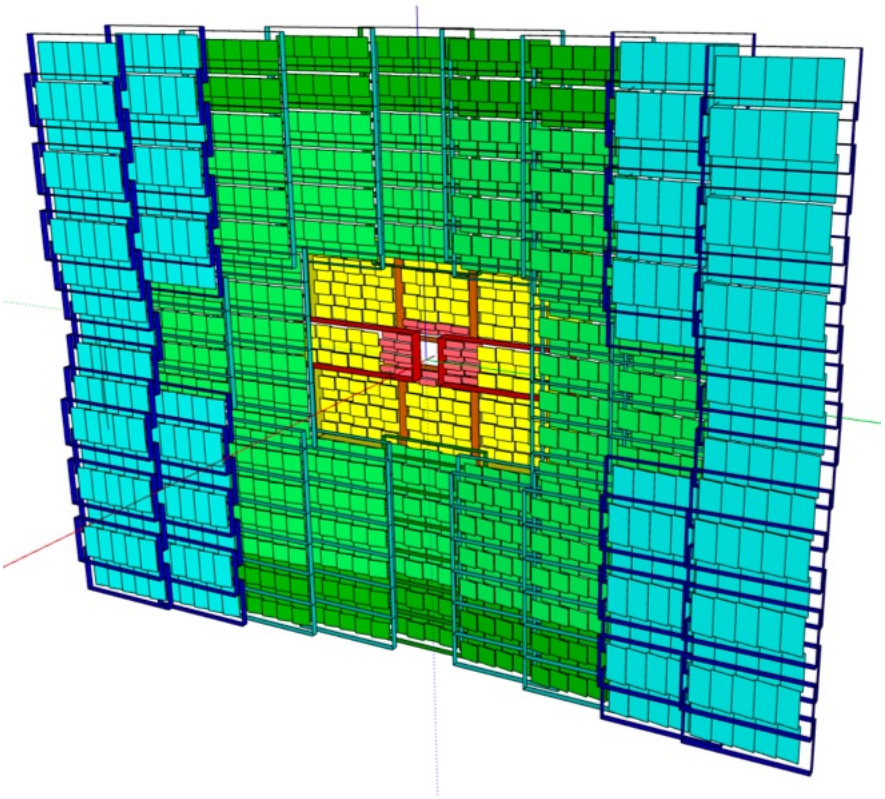

Figure 1.12: Design of the CBM TOF detector system composed of Multi-gap Resistive Plate Chambers (MRPC). In the middle, there is a beam pipe hole [36].

1.3.8.1 Particle identification in CBM

CBM will have the opportunity to measure both the di-lepton channels by using MuCh and RICH detector subsystems. The MuCh setup will consist of several hadron absorbers and tracking detectors for muon detection. It will be replaced with the RICH detector for electron identification. It is crucial to measure both the leptons and hadrons simultaneously in order to obtain a complete picture of the reaction [57]. The simultaneous measurement is possible in CBM with SIS100 electron setup, which will consist of MVD, STS, RICH, TRD, TOF, and PSD, as shown in Figure 1.4.

In this work, one million events of 12 AGeV Au-Au central collision are taken. These are generated using the UrQMD (Ultra relativistic Quantum Molecular Dynamics) event generator [58, 59] with the transport engine GEANT3. The CBMROOT (APR20 version) framework and the SIS100 electron setup are used for this study.

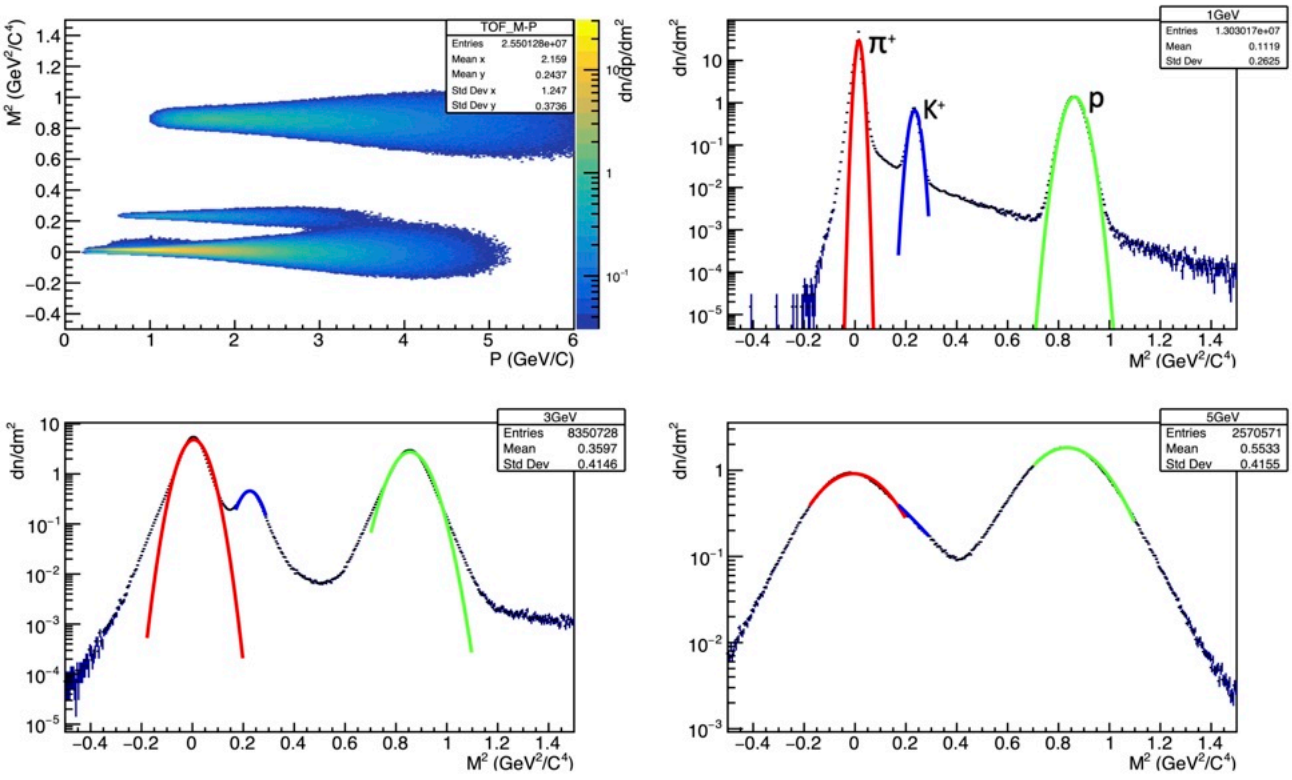

Figure 1.13: Mass^2 vs. momentum distributions for all types of particles (top left). The mass^2 distribution is in different momentum segments: 0< P <1 GeV/c (top right), 1< P <3 GeV/c (bottom left), 3 <P <5 GeV/c (bottom right)

For particle identification, the square mass is plotted against momentum distributions for all types of particles. In Figure 1.13, M represents the mass calculated from the TOF detector. If we take a different momentum range and plot the mass^2 distribution, we can see different peaks corresponding to different particles. From Figure 1.13, we can say that beyond 3 GeV/c momentum, identification of particles is not possible by this method.

The energy loss of charged particles in the detector volumes can also be used for particle identification. The energy loss distribution of all charged particles in the STS layers is shown in Figure 1.14.

This distribution is done for one million events of 12 AGeV Au-Au minimum bias collision, which are generated using the DCM-QSM-SMM (Dubna Cascade Model, Quark-Gluon String Model, and Statistical Multi-fragmentation Model) event generator [60] and transported through the SIS100 electron setup using the GEANT3 transport engine.

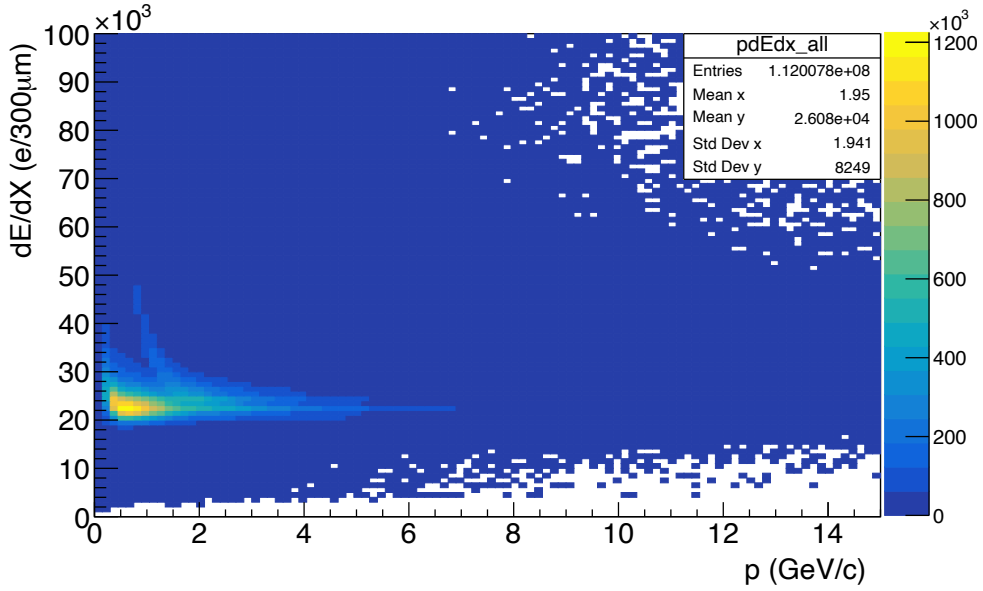

Figure 1.14: Energy loss profile for all types of particles in the STS layers.

By the energy loss method, we can separate the particles with the same m/Z ratio *e.g.*, H^2 and He^4, which cannot be identified by looking at the momentum and mass^2 distribution.

1.3.9 Forward Wall

According to the recent status, the Czech scientist group, who was involved in building of previously planned Projectile Spectator Detector (PSD) [61], come up with a new scintillator-based forward detector system with Silicon photo-multiplier (SiPM) readout [62]. Which is under discussion within the collaboration.

1.4 Aim of the thesis

In the CBM experiment at FAIR, the MuCh detector system will be used to detect the di-muon produced in the collision. MuCh will consist of several hadron absorbers and active detector triplets (called stations) in between the absorbers to track the muons. First, two stations of CBM-MuCh will consist of triple GEM detectors to handle a particle rate $\sim$ 1 MHz/cm^2 and $\sim$ 0.1 MHz/cm^2 respectively for 8 GeV per nucleon central Au-Au collision.

From the simulation, it has been found that for the interaction rate of 10 MHz, particle flux on the 3^{rd} and 4^{th} stations of the CBM-MuCh will be $\sim$ 15 kHz/cm^2 and 5.6 kHz/cm^2, respectively, for central Au-Au collisions at 8 AGeV. Single gap RPC is a strong candidate for the 3^{rd} and 4^{th} stations of CBM-MuCh. To cope-up with this high particle rate, the RPC is to be built with low electrode resistive plates and to be operated in the avalanche mode. The usage of electrodes made with low bulk resistivity seems to be a promising way to adapt the RPC to the high-rate environment of the upcoming CBM experiment.

Performances of RPCs can be improved based on different parameters. Based on the required rate of particle detection, RPCs can be built with low resistive (bulk resistivity $\sim$ 10^8 - 10^{10} Ω cm) materials. The reason behind the use of low resistive material is that it will reduce the charge-up time after each discharge and hence will reduce the dead-time fraction.

R&D on the choice of resistive materials is an important component of RPC development. Extensive R&D is going on towards improving the other parameters of the detector. There are still many open questions on RPC. Some of these are as follows:

- Study of the material used to make electrodes of RPC;

- Surface treatment of the electrodes;
- Optimisation of gas mixture;
- The mode of operation (streamer or avalanche) for high-rate operation;
- Extensive studies on time resolution and efficiency;
- Study on RPC stability;

Therefore, a detailed study is required to understand the properties of RPC and to make improvements, keeping the CBM experiment in mind. It needs to be emphasised that the R&D we plan to carry out for this detector type targets at yet uncharted scientific territory. To our knowledge, RPC detectors, in particular, bakelite RPCs, have not yet been tested or operated in such an environment.

The aim of this particular R&D program which is described in this thesis, are as follows:

- Study on the material used to make electrodes of RPC and it's surface treatment, mode of operation (avalanche or streamer). Before the building of a chamber, the study of its electrical and mechanical properties are very important. Mechanical properties include uniformity of thickness of the electrode plates and most importantly the surface uniformity. The electrical properties to be measured are the bulk resistivity and surface resistivity and their uniformity over the whole electrode surface area. The proposed R&D program will start with a selection of materials by measuring the mechanical and electrical properties of different bakelite samples.
- Improvement of efficiency, time resolution, rate capability, long term stability by varying conditions like temperature, gas composition, or radiation dose. After selecting a suitable material, RPC prototype detectors will be built with different dimensions. The basic characteristics such as efficiency, noise rate, time resolution, cross-talk, and charge sharing need to be studied in the laboratory with cosmic rays.
- Study on the composition of the fill gas and optimisation of gas mixture for Resistive Plate Chamber (RPC) is also required. The detectors need to operate stably for a few

years with good efficiency at a high particle rate. It requires fast and non-ageing gas mixtures.

- The long-term stability of the RPC detectors over a period of time is also required. For low-rate applications, the glass RPCs are found to be more stable, even though some erosion effects are found for such cases, particularly when these glass RPCs are operated in the streamer mode [63]. In the streamer mode of operation, this has been attributed to the corroding of the glass surface due to the large charge build up. At the end of the nineties, it was found that the bakelite RPCs show serious ageing effects reducing the efficiency drastically [64]. Detailed investigations revealed that the use of linseed oil for the treatment of inner surfaces of the bakelite electrode plates in such cases was the main reason for this efficiency reduction [65, 66]. Subsequently several efforts were made to look for alternatives to linseed oil treatment or to develop bakelite sheets that can be used without any application of linseed oil [67]. However, it has been found that for several experiments *e.g.* CMS, bakelite based RPCs are chosen as preferred options mainly due to the cheaper cost of fabrication.

  Ageing of gaseous detectors may occur because of chemical properties or the interaction of radiation with the materials, gases, and components. RPCs are quite robust in terms of its ageing. Once a particular material is selected and the detector is build, its ageing study and long-term stability test are very important. The stability of the performance of the chamber includes the stable operation of the detector for a reasonable long period of time.

Since India has the responsibility to build the detectors and electronics for the CBM-MuCh it will be very much beneficial for us to build the chamber indigenously.

Bibliography

[1] http://www.fair-center.eu/

[2] https://fair-center.eu/user/experiments/appa

[3] https://fair-center.eu/user/experiments/nustar

[4] https://panda.gsi.de/

[5] https://www.cbm.gsi.de/

[6] S. Chattopadhyay, Nuclear Physics A 931 (2014) 267.

[7] S. Chakraborty *et al.*, Nucl. Instr. and Meth. A 936 (2019) 424.

[8] S. Chakraborty *et al.*, CBM Progress report 2018, 67. ISBN: 978-3-9815227-6-1 DOI: 10.15120/GSI-2019-01018.

[9] S. Biswas *et al.*, Nucl. Instr. and Meth. A 617 (2010) 138.

[10] M. John *et al.*, 2022 JINST 17 P04020.

[11] https://www.gsi.de/en/researchaccelerators/fair/the_machine

[12] P. Spiller and G. Franchetti, Nucl. Instr. and Meth. A 561 (2006) 305.

[13] B. Friman *et al.*, The CBM Physics Book : Compressed Baryonic Matter in Laboratory Experiments. Springer-Verlag Berlin Heidelberg, 2011.

[14] https://www.gsi.de/fileadmin/oeffentlichkeitsarbeit/bilddatenbank/fair/FAIR-beschriftet_MSV_EN_Aug_2021.jpg

[15] Technical Design Report for the CBM, Muon Chambers (MuCh), November 2014.

[16] https://edms.cern.ch/file/2893949/LATEST/FAIR*.mp4

[17] Tetyana Galatyuk, Nuclear Physics A 982 (2019) 163.

[18] Ablyazimov, T., Abuhoza, A., Adak, R.P. *et al.*, Challenges in QCD matter physics –The scientific programme of the Compressed Baryonic Matter experiment at FAIR, Eur. Phys. J. A (2017) 53: 60.

[19] P. Senger, J. Phys.: Conf. Ser. 50 357 (2006).

[20] D. Kresan, PoS CPOD2009 (2009) 031.

[21] P. Senger and V. Friese, Nuclear Matter Physics at SIS-100, Technical report, GSI, Darmstadt, 2012.

[22] C Höehne J. Phys. G. Nucl. Part. Phys. 35 104160 (2008).

[23] A Kiseleva *et al.*, *Indian J. Phys.* 85 (1) 211-216 (2011).

[24] Claudia Höhne, EPJ Web of Conferences 171, 12002 (2018).

[25] D. Blau, I. Selyuzhenkov, V. Klochkov, KnE Energ.Phys. 3 (2018), 195.

[26] P Senger, J. Phys. G : Nucl. Part. Phys. 31 S1111 (2005).

[27] Evgeny Lavrik, AIP Conference Proceedings 2163, 030009 (2019).

[28] Talk by Piotr Gasik. https://indico.cern.ch/event/1346892/attachments/2758998/4804474/gasik_Det_Sem_24112023pptx.pdf

[29] I. Kisel, EPJ Web Conf. 108 (2016) 01006.

[30] CBM Progress report 2022, ISBN: 978-3-9822127-1-5 DOI: 10.15120/GSI-2023-00384.

[31] P. Kurilkin *et al.*, EPJ Web of Conferences 138, 12001 (2017).

[32] Technical Design Report for the CBM, Micro Vertex Detector (MVD), December 2021.

[33] D. Pfeifer *et al.*, Magnetic field simulations for the CBM dipole magnet, CBM Progress Report 2022.

[34] M. Shiroya *et al.*, New concept for the Silicon Tracking System: STS-3+5, simulation geometry and performance, CBM Progress Report 2022.

[35] Technical Design Report for the CBM, Ring Imaging Cherenkov (RICH) detector, June 2013.

[36] CBM Progress report 2021, ISBN: 978-3-9822127-0-8 DOI: 10.15120/GSI-2022-00599.

[37] S. Biswas *et al.*, Nucl. Inst. and Meth. A 718 (2013) 403.

[38] S. Biswas *et al.*, 2013 JINST 8 C12002.

[39] A.K. Dubey *et al.*, Nucl. Inst. and Meth. A 755 (2014) 62.

[40] S. Biswas *et al.*, Nucl. Inst. and Meth. A 800 (2015) 93.

[41] S. Biswas *et al.*, Nucl. Inst. and Meth. A 824 (2016) 504.

[42] R.P. Adak *et al.*, 2016 JINST 11 T10001.

[43] R. P. Adak *et al.*, Nucl. Inst. and Meth. A 846 (2017) 29.

[44] S. Roy *et al.*, Nucl. Inst. and Meth. A 936 (2019) 485.

[45] S. Chatterjee *et al.*, Nucl. Inst. and Meth. A 936 (2019) 491.

[46] S. Chatterjee *et al.*, Nucl. Inst. and Meth. A 977 (2020) 164334.

[47] S. Chatterjee *et al.*, J. Phys.: Conf. Ser. 1498 (2020) 012037.

[48] S. Chatterjee *et al.*, 2020 JINST 15 T09011.

[49] S. Chatterjee *et al.*, Nucl. Inst. and Meth. A 1014 (2021) 165749.

[50] S. Chatterjee *et al.*, Nucl. Inst. and Meth. A 1045 (2023) 167573.

[51] S. Chatterjee *et al.*, Nucl. Inst. and Meth. A 1046 (2023) 167747.

[52] S. Chatterjee *et al.*, Nucl. Inst. and Meth. A 1049 (2023) 168110.

[53] M. Mondal *et al.*, Nucl. Inst. and Meth. A 1025 (2022) 166042.

[54] E. Nandy *et al.*, Proc. of the DAE-BRNS Symp. on Nucl. Phys. 61 (2016) 1024.

[55] Technical Design Report for the CBM, Transition Radiation Detector (TRD), January 2017.

[56] Technical Design Report for the CBM, Time - of - Flight System (TOF), October 2014.

[57] Anna Senger, International Journal of Modern Physics E. Vol. 29, No. 2 (2020) 2030003.

[58] S.A. Bass, M. Belkacem, M. Bleicher *et al.*, Prog. Part. Nucl. Phys. 41 (1998) 255.

[59] M Bleicher *et al.* J. Phys. G: Nucl. Part. Phys. 25 (1999) 1859.

[60] M. Baznat, A. Botvina, G. Musulmanbekov *et al.*. Monte-Carlo Generator of Heavy Ion Collisions DCM-SMM. Phys. Part. Nuclei Lett. 17, 303-324 (2020).

[61] Technical Design Report for the CBM, Projectile spectator detector (PSD), July 2015.

[62] N. Herrmann, Executive Summary: Status of the CBM Experiment, CBM Progress Report 2022.

[63] G. Bruno, Eur Phys. J. C 33 (2004) s1032.

[64] J. Va'vra, Nucl. Inst. Methods. A 515 (2003) 354.

[65] F. Anulli *et al.*, Nucl. Inst. and Meth. A 508 (2003) 128.

[66] F. Anulli *et al.*, Nucl. Inst. and Meth. A 515 (2003) 322.

[67] J. Zhang *et al.*, Nucl. Inst. and Meth. A 540 (2005) 102.

Chapter 2

Introduction to Resistive Plate Chamber (RPC)

The gas detector era started with the invention of the Geiger counter about 100 years ago [1]. Afterward, many developments are made. However, the major breakthrough happens with the invention of multi-wire proportional chambers (MWPCs) in the year 1968 [2]. Georges Charpak was awarded the Nobel Prize in 1992 for the invention of MWPC. The Resistive Plate Chamber (RPC) detector was first introduced by Rinaldo Santonico and Roberto Cardarelli at the beginning of 1980 [3] for triggering and tracking, whereas the micro-pattern gaseous detectors (MPGDs) were subsequently developed to handle high particle rate. Gas Electron Multiplier (GEM) in 1997, introduced by F. Sauli is the first among the MPGDs [4].

RPCs have some advantages due to their high resistive electrode plates. High resistivity protects the spark and helps to contain the discharge in a localised area. Single gap RPCs have position resolution $\sim$ 1 cm to $\sim$ 100 μm and time resolution can be achieved of the order 1 ns.

RPCs are developing day by day and it is already been used in several experiments. The design and dimensions were different in different experiments to meet the experimental need. In the Large Hadron Collider (LHC) at the European Organization for Nuclear Research (CERN) RPCs were also used that cover the total area $\sim$ 10000 m^2. Different cosmic ray experiments also use RPCs. In the Astrophysical Radiation with Ground-based Observatory at YangBaJing (ARGO-YBJ) experiment the total area coverage was $\sim$ 10000 m^2 [5, 6, 7]. Not only these

RPCs are nowadays explored for different applications like flight-positron emission tomography (TOF-PET), homeland security, flame detection, etc., and also for medical imaging purposes.

2.1 Cylindrical gaseous detector vs. parallel plate chamber

In the gaseous detector having cylindrical geometry as shown in Figure 2.1, there is a central anode wire where electrons are collected and the avalanche occurs close to the wire. The metallic cylinder is used as the cathode.

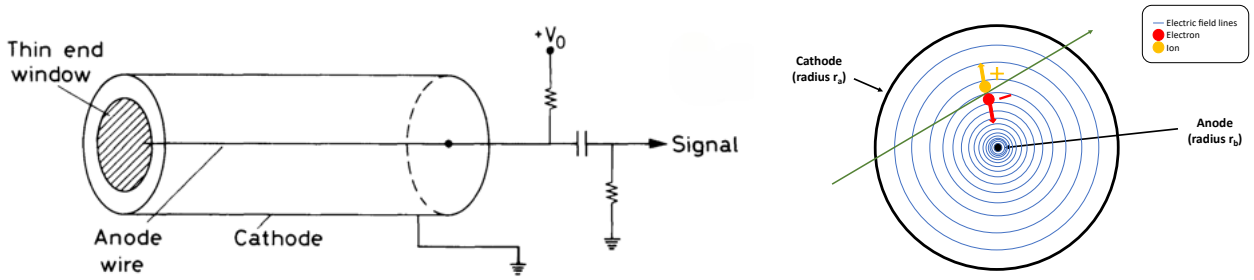

(a) Cylindrical geometry [8] (b) Cross sectional view

Figure 2.1: Cylindrical geometry detector and its cross-sectional view

The electric field in the cylindrical detector is inversely proportional to the distance from the anode wire. The electric field is very high close to the central anode wire and decreases rapidly as it approaches the cylindrical cathode surface. The electric field at a distance r from the anode wire varies according to the formula

$$E(r) = \frac{V}{r ln \frac{r_a}{r_b}}; \tag{2.1}$$

where V is the potential difference between the cathode and anode, r_a is the radius of the cylindrical metallic tube and r_b is the radius of the central anode wire. r denotes the distance from the central anode wire to the point of consideration.

On the other hand, for the parallel plate structure (as shown in Figure 2.2), the electric field varies as follows

$$E = \frac{V}{d}; \tag{2.2}$$

where V is the potential difference between the electrode plates and d is the separation between them.

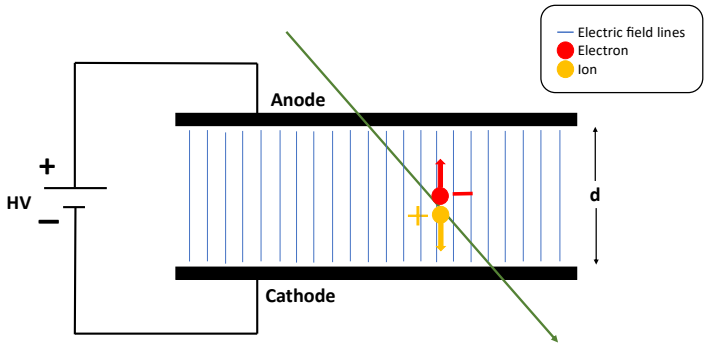

Figure 2.2: Parallel plate ionisation chamber

The main difference between a cylindrical gaseous detector and a parallel plate chamber is that in the first case, the electric field decreases inversely with the distance from the central anode wire, whereas, in the second case, the electric field is uniform. So, for the cylindrical detector, the probability of the formation of the avalanches is very high, only close to the central wire. On the other hand, in the case of parallel plate chamber, the whole volume is available for the formation of an avalanche and every point has the same probability for the formation of the avalanche.

Though the main process is the same for both cases, *i.e.* ionisation of the gas medium due to the passage of ionising particles *e.g.* X-rays, gamma rays, charged particles, neutrons, etc., the planer detector shows better time resolution. The reason can be described from the electric field configuration and the charge mobility due to that field. The primary ionisation can take place anywhere in the gas volume for both cases. But for the cylindrical geometry, the primary electrons will have to drift for a fluctuating time, depending on the position they were generated, before reaching the region close to the wire where they can form an avalanche and produce a detectable signal. The time between the creation of the primary electrons and the formation of the output signal will be intrinsically affected by fluctuations due to the fact that different primary electrons will have to travel different distances depending on where they were generated.

For the parallel plate geometry, a primary electron can produce an avalanche immediately after its generation. In this case, the electrons do not need to move to the so-called intense electric field region, as the whole gas volume is available for amplification and favourable for the production of the avalanche. So, in summary, for parallel-plate detectors, there is practically no separation between the drift and multiplication regions, and this extraordinarily reduces the fluctuations in timing. Furthermore, the output signal is the cumulative sum of the signals produced by the various avalanches, and this further reduces the timing fluctuations [9].

The planer geometry RPC detector has many advantages compared to the classical cylindrical gaseous detector. Some of the following features are listed below.

- The electrode materials are very common and easily available in the market, such as bakelite, glass, and ceramic [10, 11, 12]. Only high resistive material is needed with a very smooth surface. The resistivity is of the order $\sim 10^8$ to $\sim 10^{12}$ Ω cm depending on the requirement of rate handling.
- Glass is very fragile in nature, so the handling needs special care. Bakelite electrode plates suffer from surface roughness issue. Ceramic RPCs still need to be explored extensively.
- Detector geometry is very simple. That is why it is very easy to fabricate the chamber.
- As the materials are very cheap and fabrication is also very easy, they are suitable for large area coverage. Many cosmic ray experiments are using RPC for their large area coverage.
- The fabrication cost per unit area is very low.
- Position resolution of this type of detector is reasonable. Position resolution can vary between cm to a few hundreds of μm [13, 14, 15]. So, this type of detector can be used for medical imaging purposes also.
- RPC has extremely good time resolution. For single gas gap RPC, the time resolution is $\sim$ 1-2 ns, whereas, for multi-gap configuration, a few 10s of ps time resolution can be achieved.

- The detector can be operated continuously. No pulsed HV for discharge quenching is needed.
- Signal pickup system is very simple. Either strip readout or pad readout can be used. Also, two dimension readout can be used to obtain both X and Y positions from the same chamber.
- If discharge occurs in the detector, it will be localised due to high resistive electrode surface, and the dead area will be very small. The remaining gas volume will be available for avalanche formation and will be active.
- RPCs can be used for other applications like TOF-PET, flame detection [16, 17], etc.
- RPC can be used for long-term operation without any degradation in the performance.

In this chapter, the general structure of the RPC, its basic working principle, different modes of operations and their applications in the past and presently ongoing experiments are discussed.

2.2 General structure of RPC

The first gas-filled detector was ionisation chamber and the very first detectors were cylindrical in geometry. Later planer geometry was also explored. The detectors can have different dimensions depending on the experimental requirements, but the basic working principle of any gas-filled detector is the same, and the principle is ionisations of the gas medium.

The main advantage of parallel plate detectors is that they provide less jitter and offer excellent timing characteristics.

The modern RPC detector was first introduced by Rinaldo Santonico and Roberto Cardarelli at the beginning of 1980. The first prototype was built with phenolic laminate compressed at high pressure that had a gas gap of 1.5 mm and operated with a gas mixture of argon and butane at ordinary pressure [3].

The single gap RPC has planner geometry and requires two resistive electrode plates for fabrication. The schematic of the RPC is shown in Figure 2.3. The electrode plates have bulk

resistivity $\sim 10^8$ - 10^{12} Ω cm. These plates are separated uniformly by high-resistive materials called spacers. Generally, spacers have two to three orders higher bulk resistivity than the resistivity of the electrode plates. Depending on the requirement of the experimental design, the gas volumes have different thicknesses ($\sim$ 1 - 9 mm). The spacers are glued using adhesive epoxy. The gap thickness depends on the thickness of the spacers. There are at least two gas nozzles: One is used for the gas inlet, and another is used for the gas outlet. More than two gas nozzles can be used depending on the dimension of the detector. Gas nozzles are also used as part of the side spacers. There are also button spacers used to maintain the uniform gas gap and to resist the sagging of the gas volume. Depending on the dimension, the number of button spacers varies.

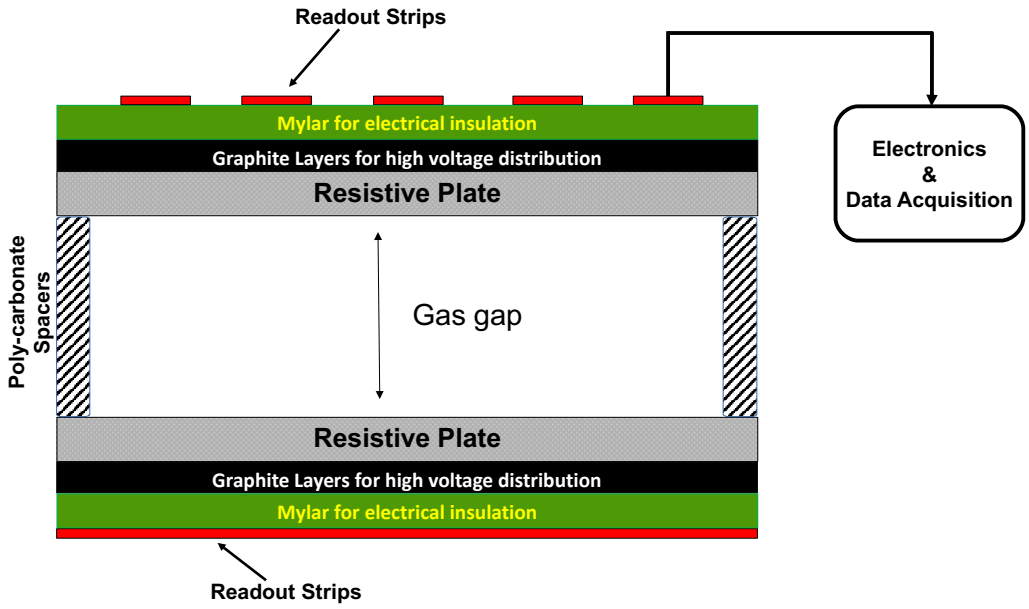

Figure 2.3: Schematic of the RPC detector. There are two resistive electrode plates separated by spacers. At the outer electrode surfaces, there is graphite coating for high-voltage distribution. Outer surfaces are covered by mylar insulators. Orthogonal readout strips are placed on the top and bottom to collect induced signals.

After making the gas gap, the gas tightness is ensured. At the outer edges, a thin layer of adhesive is sometimes applied if required to prevent gas leakage. Final gas tightness is checked using digital probes or the water displacement method (discussed in a later section 3.2.1). After proper cleaning of the outer surfaces of the electrode plates, a very thin layer of graphite

coating ($\sim$ μm) is done for the high voltage distribution. The conductivity of Graphite is slightly lower than metals [18]. So, the application of graphite does not shield the generated induced signals. Moreover, nowadays, people are using different coatings other than graphite for high voltage distribution [13, 19]. Small pieces ($\sim$ 1 cm $\times$ 1 cm) of copper layers are posted at diagonal positions on the graphite layers and high-voltage wires are soldered to apply high voltage. Finally, outer surfaces are covered with the mylar layer (thickness $\sim$ 100 μm) for the electrical insulation from the graphite layer to the readouts. Pickup strips are placed on the top and bottom of the detector in an orthogonal position for the X-Y readout of the induced signal.

2.3 Basic principle of RPC

The simplified geometry of a RPC detector is described in the section 2.2. The gas gap is filled with a suitable gas mixture, typically at atmospheric pressure. High voltage of opposite polarities are applied in the electrode plates, and the electric field is generated.

After the application of high voltage for the first time, the detector is conditioned for sufficient time. When ionising particles pass through the detector, primary electrons are produced because of the collision of particles with the gas molecules. Free electrons and ions start drifting, following the direction of electric field lines. Under sufficiently high ($\sim$ E $>$ 10^6 V/m) electric field, the primary electrons start to ionise more and more neutral atoms. During the drift, electrons encounter stochastic collisions and a large number of ion-electron pairs are produced. After creation by radiation interactions, both the electrons and ions undergo many such collisions with neutral gas molecules until they are collected. Subsequently, the pair production dominates due to the influence of a strong electric field. If the electric field is very strong, electrons get sufficiently high kinetic energies between the collisions and eventually can ionise neutral molecules. This production of ion-electron pairs occurs in a multiplicative way. The kinetic energy gain in an electric field depends only on charge and does not depend on mass. When a large number of electrons are produced at a small volume in a cascaded way, an electron cluster is formed, and avalanche formation is initiated. This formation of avalanche is called the Townsend avalanche. The electric field must be stronger than the threshold during the

avalanche formation process. The fractional increase in the total number of electrons per unit path length is governed by the Townsend Equation:

$$dn(x) = n(x)\alpha dx; \tag{2.3}$$

where, *n(x)* = number of electrons at a distance x from the starting of ionisation.

α = First Townsend coefficient is defined as the probability for an electron to generate additional ion-electron pairs per unit length. α depends on the electric field. For a spatially constant field, such as within parallel plates, α is a constant.

Integrating the equation 2.3 one can obtain

$$n(x) = n_0 e^{\alpha x}; \tag{2.4}$$

where, n_0 is the number of primary electrons located at a distance x=0. *n(x)* is the total number of electrons after traversing a distance x. The equation 2.4 also shows that the number of electrons increases exponentially with the distance.

The total number of electrons is therefore multiplied and this amplified electron cluster induces a detectable signal at the readout.

Depending on the applied voltage to produce the electric field, the operation of gas-filled detectors can be divided into several regions, as shown in Figure 2.4.

Recombination region : At low voltage, the electric field is not sufficiently large to accelerate electrons and ions. Only a small portion of the created electrons and ions reach the appropriate electrodes because the electrons and ions can quickly recombine due to their own electrical attraction after they are formed. Yet, a growing portion of the generated ions will contact the electrodes as the detector voltage rises. Up until the "saturation" voltage is reached, this increase keeps going. Because it is impossible to precisely estimate the number of recombinations or the number of initial ion pairs formed, detectors are not operated in this region.

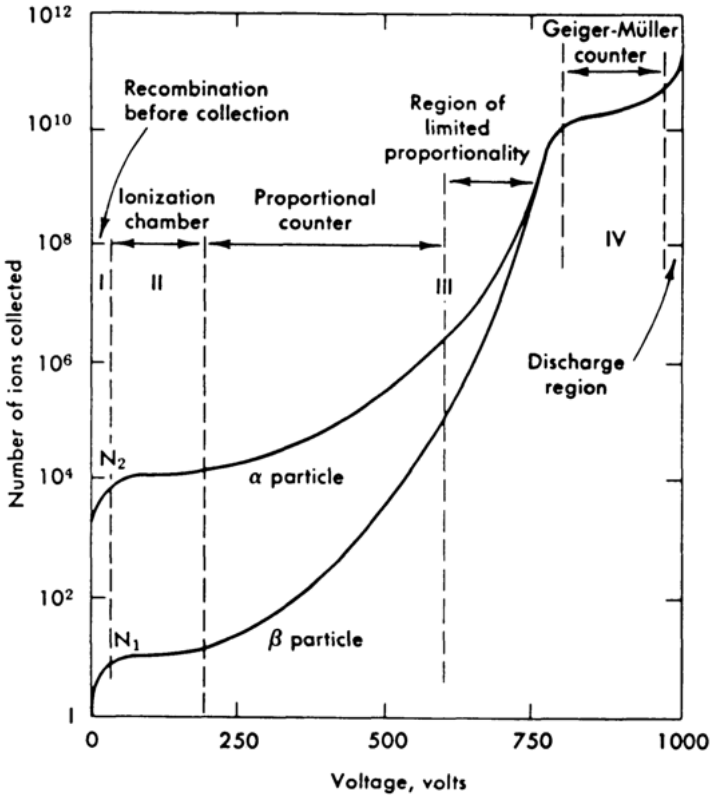

Figure 2.4: Different operation regions of gas-filled detectors. The plotted pulse amplitude as a function of the applied voltage is shown for two different particles depositing different amounts of energy on the gas volume. [8]. In the proportional region, the secondary number of electrons increased linearly with the primary no of electrons and the pulse height increased exponentially with applied voltage.

Ionisation region : An increase in voltage stops the recombination process and more number of ion-electron pairs reach the electrode. Thus the current begins to increase. The number of ion pairs generated by the incident radiation and the number of ions collected by the electrodes are equal. The type and energy of the particles or rays in the incident radiation determine it. The curve is hence flat in this area. The voltage needs to be higher than the limit at which recombining ion pairs is possible. But the voltage isn't high enough to result in gas amplification (secondary ionisation). As the electric fields used by the detectors in the ionisation region are weak, no gas multiplication takes place. The applied voltage has no effect on their current.

Proportional region : As the detector voltage is raised higher in the proportional area, the charge collected rises while the quantity of primary ion pairs stays constant. The primary

electrons are given enough energy and acceleration as the voltage is raised to ionise more atoms in the medium. The Townsend avalanche or cascade effect, which generates a single, powerful electrical pulse, is brought on by the acceleration of the secondary ions that are produced. The number of electron-ion pairs is proportional to the number of primary electrons, despite the fact that there are many secondary ions for each primary event. The current is then amplified proportionally, with a multiplication factor that depends on the operating voltage. The output signal is substantially bigger than that from an ionisation chamber but is still proportional to the initial ionisation generated in the detector. This factor can reach up to 10^6. It is crucial because the primary ionisation depends on the type and energy of the particles or rays in the field of radiation that was intercepted. The gas amplification factor is calculated by dividing the total number of ion pairs collected by the total number of ion pairs generated by primary ionisation. The overall amount of ionisation in this area may rise to a measurably high level due to the gas amplification. The detector's signal-to-noise ratio is significantly improved by the charge amplification technique. The gas amplification factor does not alter if a voltage stays constant. Instruments for proportional counter detection are extremely sensitive to very low radiation levels. Moreover, proportional counters can measure energy and identify particles. As different radiation intensities and types have vastly varying primary ionisations, it is possible to distinguish between them by looking at the pulse height.

Limited proportional region : The increase in the applied voltage results in an increase in the electric field and nonlinear effects comes into the picture. The gas amplification factor stops rising proportionally to the voltage in the limited proportional zone. With a specific applied voltage, additional ionisations and nonlinear effects do not result in a signal output that is proportionate to the energy deposited. The free electrons are quickly collected due to high mobility, while positive ions move very slowly, which takes a long time and during the period when travel ions collect electrons. During the collection of the electrons, a slow-moving cloud of positive ions is created, which disperse slowly as it moves towards the cathode. If the positive ion concentration is sufficiently high, the space charge is formed and the electric field is distorted, which leads to distortion in gas multiplication, and non-linearity effects are observed.

Geiger-Mueller region : Secondary avalanches are possible in the Geiger-Mueller region because of the voltage and resulting extremely high electric field. Photons released by excited atoms and the avalanche formation can be triggered. Since these photons are not impacted by the electric field, they may interact a long way from the initial avalanche, involving the entire Geiger tube. These avalanches provide a strong signal that has shape and height independent of the primary ionisation and photon energy (the amplification factor can reach about $10^{10)}$. Gamma rays and any other kind of charged particle that can enter a detector can be detected by Geiger-Mueller detectors. These instruments' principal benefit is that they frequently don't need signal amplifiers. A positively charged ion cloud disrupts the electric field and stops the avalanche process because positive ions do not travel far from the avalanche location. In actuality, the application of "quenching" tactics can improve the avalanche's formation. In reality, a plateau with minimal count rate variation characterises the Geiger voltage zone. The effectiveness of the quencher in the gas determines how wide the plateau is. Geiger counters, in contrast to proportional counters, cannot distinguish between the energy of incident radiation particles since the output signal is independent of the amount or nature of original ionisation.

Discharge region : Ultimately, the electric field creates a continuous discharge of the medium, with or without radiation, above the Geiger-Mueller area at much higher voltages, rendering the chamber insensitive to any incident ionisation. Ionising radiation cannot be detected in this area or measured there. When at the end of the plateau, the Geiger tube voltage is increased; For that case, the count rate quickly rises until the start of continuous discharge, at which point the tube loses its ability to detect radiation and might sustain damage.

The RPC detectors are operated in the Limited Proportional region. At higher voltages, the space charge effect comes into play and the electric field is significantly distorted. In this region, though the pulse height increases but the secondary number of electrons are not proportional to the number of primary electrons.

2.4 Mode of operation

The choice of gas mixture plays an important role in the operation of RPC, as the drift of ions and electrons heavily depends on the mixture used. If Argon (Ar) based gas mixture is used, then the produced signal will be very large. In this case, the produced charge is of the order of 100 pC. On the other hand, the Tetrafluoroethane ($C_2H_2F_4$) is itself an electronegative gas due to the presence of Fluorine component and in $C_2H_2F_4$ based mixture, the produced charge is of the order of 1 pC.

Depending on the gas mixture used, the produced charge varies, and the modes of operations are broadly classified into two categories. One is called the "Avalanche" mode, where the produced charge is of the order of 1 pC and the other one is called the "Streamer" mode, where the produced charge is of the order of 100 pC. These two modes are discussed briefly in the following sections.

2.4.1 Avalanche

When ions and electrons drift toward the respective electrodes, they collide with neutral gas molecules. If they have sufficient kinetic energy, they ionise those neutral gas molecules. The threshold value of the electric field above which the secondary ionisation will occur is typically 10^6 V/m at atmospheric pressure. During their subsequent drift, they can create additional ionisation.

This gas multiplication process, therefore, takes the form of a cascade and known as the "Townsend avalanche" in which each free electron created in such a collision can potentially create more free electrons by the same process. Thereby in a cascaded way, a cluster of electrons is created, and a signal generates. The amplification of the signal inside the gas gap is small in this process. The fractional increase in the number of electrons per unit length is governed by the equation 2.3.

The produced charge inside the gas gap is low ($\sim$ 1 pC) in the Avalanche mode of operation. Therefore the detector can also work in the high particle flux environment and moderate to high counting rate capability ($\sim$ Hz/cm^2) is achieved. This is possible by employing $C_2H_2F_2$

gas as the active medium. This gas is intrinsically electronegative in nature and, therefore, can quench a small amount of electrons. Sometimes, SF_6 is also added in a very small fraction to quench electrons further and improve the performance. Due to low charge production, the output signal is small and it requires sophisticated electronics and a pre-amplifier to get the signal.

2.4.2 Streamer

In most of the gaseous detectors, at some total critical charge in the avalanche, a transition from the primary avalanches to sparks is observed [20]. Scrupulous studies performed by Raether showed that for the parallel-plate detectors, this happens when

$$An_0 \gtrsim 10^8 \quad electrons; \tag{2.5}$$

where A is the gain of the detector and n_0 is the primary number of electrons.

In the streamer mode of operation, a number of large nonlinear effects can be seen compared to the linear mechanism. In contrast to the Avalanche mode, the physics of the streamer is very difficult to understand.

In this mode, the generated signal is large ($\sim$ 100 pC). Therefore, no signal amplification is required using external electronic circuits. The readout system of Streamer mode RPCs is quite simple, as the signal can be directly fed to the electronics and can be discriminated by choosing the appropriate threshold voltage. But there is an issue. As the spark can happen easily in this mode with a large amount of charge resulting in a large dead area for each such spark, the rate capability is low and limited to a few hundred Hz/cm^2 [21].

2.5 Classification of RPCs

Since the invention of RPCs, people have been very enthusiastic about the improvement of this detector. They were in search of the spark protective versatile detector. The design of the

resistive plate chamber is flexible as per the requirement. This creates different types of RPCs to quench the thirst of innovative minds.

RPCs are broadly categorised into two types. The first one is classified according to the design and the second one is classified according to the application of the detector. The Single-gap, Wide-gap, and Multi-gap go under the design category, and the Trigger and Timing RPCs go under the application category. These different types of RPCs are discussed briefly in the following sections.

2.5.1 Classification by design

2.5.1.1 Single-gap RPC

The first developed RPC by R. Santonico and R. Cardarelli was the single gap RPC [3]. The single gap RPC is the simplest in design and that's why very easy to fabricate. The first RPC was built with bakelite plates with a uniform gas gap of 2 mm. After that, there were several improvements done to this detector [22, 23, 24].

2.5.1.2 Wide-gap RPC

The two main functions of the gas gap in RPCs are a) to produce the primary ionisation cluster and b) to obtain the gas gain. The accumulated charge in a RPC signal depends on the width of the gas gap. To improve the efficiency, a wide gap structure was introduced. The single gap RPC or narrow gap RPC usually has a gas gap $\sim$ 2 mm, whereas for the wide gap RPCs, the gas gap is usually $\sim$ 8 mm or 9 mm. The wide gap RPCs are superior in terms of rate capabilities, but their timing resolution is poor compared to the narrow gap RPCs. The main reason behind this is the lower dynamic range of the produced charge; this causes the smaller current to flow through the gas gap and through resistive electrodes. In wide gap RPCs, a large amplitude signal is produced in avalanche mode. The time resolution is poor due to the fact that the larger path introduces larger fluctuations in the signal arrival time. Wide gap RPCs also lag behind the narrow gap in terms of power dissipation produced inside the gas gap. It is almost ten times lower compared to the narrow gap RPCs [25].

2.5.1.3 Multi-gap RPC

This is a new type of RPC and as the name suggests that this type of RPC has multiple gas gaps as shown in Figure 2.5. Though the gas gap number is multiple, the width of each gas gap is very small; generally, it is of the order 0.2 mm to 1 mm in each gap. The primary idea is to improve the timing performance of the detector. In multi-gap RPC (MRPC), the total gas volume is segmented into a number of small gas gaps of equal width by introducing some intermediate resistive plates of high resistivity in between the two outermost resistive electrode plates. A passing charged particle creates an avalanche in the gas. For the single or narrow gap RPC, there is only one gas volume available for the avalanche to take place and thus, the size of the avalanche fluctuates. In contrast, for MRPC, multiple gas volumes are available for the avalanche to take place.

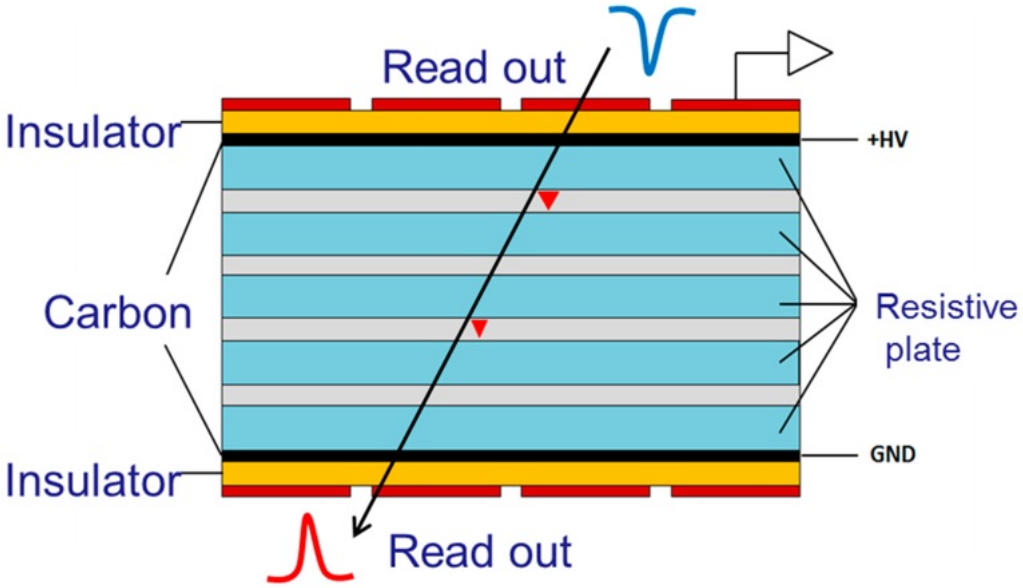

Figure 2.5: Multi-gap resistive plate chamber (MRPC) detector schematic. Positive signals (red pulse) are induced on the bottom cathode electrodes by the avalanches (red triangles in the gaps), whilst negative signals (blue pulse) are induced on the top anode electrodes. (Picture is taken from ref. [26]).

High voltages are applied only to the external electrode plates of each stack of resistive plates, and the intermediate plates remain electrically floating. Thus one can build the detector by stacking plates one after another, separated by very thin spacers. Sometimes the stack of electrode plates is separated by fishing wires and kept in a gas-sealed box to build the detector

module. Pickup strips are located outside the stack and insulated from the high-voltage electrodes. Signals on the pickup electrodes are induced by the movement of charge inside the gas volume. The induced signals can be generated by the movement of charges in any of the gas gaps between the anode and the cathode pickup strips.

2.5.1.4 Hybrid RPC

A suitable combination of metallic and resistive electrode plates (as shown in Figure 2.6) can be used to build a new type of RPC called the Hybrid RPC. These types of detectors are simple and mechanically stable. For such detectors time resolution is generally very good (< 50 ps σ) and detection efficiency is also good ($> 95\%$) [27].

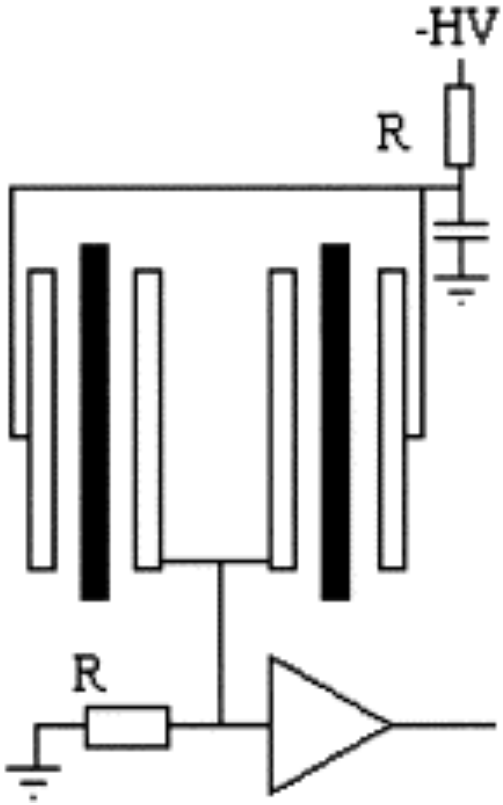

Figure 2.6: Schematic of a hybrid RPC. White electrodes are metallic and black electrodes are resistive. (Picture is taken from Ref. [28]).

The Parallel Plate Chamber (PPC) detector, made of two metallic plates, suffers from the spark problem, and by introducing resistive plates, this problem was diminished. This type of RPCs can find application in TOF and PET imaging.

2.5.2 Classification by application

2.5.2.1 Trigger RPC

Single gap RPC with 2 mm gas gap as shown in Figure 2.7 or double gap RPC can achieve very high efficiency ($\sim$ 98 - 99%) and good time resolution ($\sim$ 1 - 1.5 ns (σ)) [29]. Generally, these types of RPCs are used for triggering the Minimum Ionising Particles (MIPs) such as muons. These varieties of RPCs are called Trigger RPCs. In real experiments to identify beam bunch responsible for a particular event and also for eliminating noises from random events trigger, such trigger RPCs are used.

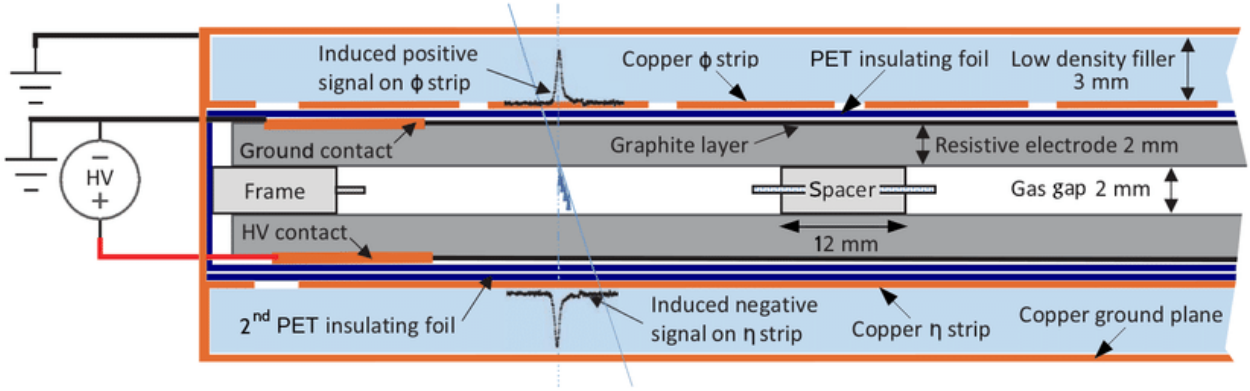

Figure 2.7: Single gap RPCs used in the ATLAS experiment at the Large Hadron Collider for the first-level (L1) muon trigger in the barrel region. (Picture is taken from ref. [30]).

2.5.2.2 Timing RPC

These types of RPCs are generally multi-gap in configuration and have a large area for the Time Of Flight (TOF) measurements. The gas gap is usually 0.2 - 0.3 mm. These types of RPCs are operated in the avalanche mode with an electric field of 100 kV/cm. These types of RPCs provide an efficiency $\sim$ 99% with a time resolution of $\sim$ 50 ps (σ) or better. The time resolution of the timing RPC is much better than the trigger RPC.

2.6 Gas composition for RPC

The choice of the proper gas mixture for any gaseous detector is the most important factor. As the electric field increases with voltage, the secondary ionisation of gas molecules takes place more and more. During the migration of positive and negative charges, such secondary ionisation occurs. So, in the next step, multiplication in electrons and ions occurs and an avalanche is formed. For this, the choice of gas mixture plays an important role in the proper operation and selection of the mode of operation of a gas-filled detector.

Usually, noble gases are used as the principal component, and one or two additional gas components are used for the quenching purpose. The quenching gases are those which strongly or partially suppress the secondary processes during the gas ionisation and thereby reduce noise.

In the conventional single gap RPC, a mixture of Argon (Ar), isobutane (i-C_4H_{10}), and Tetrafluroethane ($C_2H_2F_4$) gases in widely varying proportions is used at atmospheric pressure in the streamer mode of operation. The isobutane is used to prevent the secondary streamer by quenching the photon, and $C_2H_2F_4$ is used to limit the streamer size from spreading in the transverse direction. In the avalanche mode of operation, mixtures of $C_2H_2F_4$ with 2 - 5% of i-C_4H_{10} are used. Sometimes, Sulphur Hexafluoride SF_6 is also used in a very small fraction ($\sim$ 0.2 - 0.5%) due to its strong electron affinity. But the gases $C_2H_2F_4$ and SF_6 are not environment-friendly gas as they have very high global warming potential (GWP).

Nowadays, most of the European countries impose restrictions on the use of $C_2H_2F_4$ gas due to its high GWP (GWP: $\sim$ 1430). Also, it is chemically reactive with K, Ca, powdered Al, Mg, Zn. Under some environments (*e.g.* high-temperature circumstances), Carbon monoxide, Carbonyl fluoride, and Hydrogen fluoride can be formed [31].

People are looking for alternative eco-friendly gas mixtures for the RPC. One of the interesting articles by A. Bianchi *et al.* [32] shows isomers of fluorinated propene called Hydro-Fluoro-Olefins (HFOs) gas mixtures are showing promising results [33]. With this gas mixture, produced avalanches are more wider and also carry more charges [34]. Still, many R&D is going on for a suitable alternative.

2.7 RPC used so far

RPCs have been used in many High-Energy Physics experiments for their high efficiency and good time resolution. Not only the efficiency and time resolution are good, but people also use RPCs because of their robustness. Many experiments use RPCs by employing different materials and different configurations. The construction techniques, designs, shapes, operating conditions, etc., were also different. Due to the flexibility of design, the application of RPCs is increasing day by day. Because of their parallel plate geometry, the time resolution of this type of detector is very good, and as a result, they are mostly used for timing and triggering purposes. Different cosmic ray experiments also use RPCs as these detectors can cover large detection areas. The Table 2.1 contains a brief summary of different experiments with different RPCs and their configurations and application modes.

Table 2.1: A list of different past and present experiments that use RPC with different materials, configurations and operational modes [21, 80].

Experiment	Application	Area (m^2)	Electrode material	Volume resistivity (Ω cm)	No. of gaps	Gap (mm)	Mode of operation
BaBar	Trigger	2000	Bakelite	10^{11} - 10^{12}	1	2	Streamer
Belle	Trigger	2000	Glass	$> 10^{12}$	2	2	Streamer
ALICE-Muon	Trigger	140	Bakelite	3×10^{9}	1	2	Streamer
ALICE-TOF	Timing	150	Glass	10^{13}	10	0.25	Avalanche
ATLAS	Trigger	6550	Bakelite	(1-4) $\times$ 10^{10}	1	2	Avalanche
CMS	Trigger	4000	Bakelite	$\sim10^{10}$	2	2	Avalanche
STAR	Timing	60	Glass	10^{12} - 10^{13}	6	0.22	Avalanche
PHENIX	Trigger	-	Bakelite	10^{10}	2	2	Avalanche
OPERA	Trigger	3200	Bakelite	$>5\times10^{11}$	1	2	Streamer
BESIII	Trigger	1200	Bakelite	10^{9} - 10^{13}	1	2	Streamer
YBJ-ARGO	Trigger	5600	Bakelite	(0.5-1) $\times$ 10^{12}	1	2	Streamer
HARP	Timing	10	Glass	10×10^{12}	4	0.3	Avalanche
HADES	Timing	8	Glass	5×10^{12}	4	0.3	Avalanche
FOPI	Timing	5	Glass	10^{12}	6	0.3	Avalanche
CBM-TOF	Timing	120	Glass	(3-4) $\times$ 10^{10}	6	0.22	Avalanche
NeuLAND	Timing	4	Glass	1×10^{13}	3	0.3	Avalanche
CBM	Timing	-	Bakelite	$\sim10^{10}$	1	2	Avalanche

Some of the early experiments where RPCs were used are NADIR (Neutron Antineutron Doublet Investigation by Reactor at the TRIGA MARK II reactor of the University of Pavia) [35], electron-positron experiment FENICE (1986 -1993) [36], E771 (fixed target experiment at Fermi National Accelerator Laboratory), WA92 (fixed target experiment at CERN), and MINI (a horizontal cosmic ray telescope equipped with RPC) [37].

During the last few years, Resistive Plate Chambers (RPC) [3, 38, 39, 40] have been widely used in high energy physics experiments for trigger and tracking because of a) relatively low cost of materials used in making of RPCs, b) robust fabrication procedure and handling and c) excellent time and position resolution. RPC is a gas-filled detector utilising a constant and uniform electric field produced by two parallel electrode plates made of a material with high bulk resistivity.

RPCs are primarily used for generating faster triggers for muon detection [41], time of flight (TOF) [42, 43, 44, 45] measurement, and tracking capabilities in multi-layer configurations. They were used in the forward-backward muon spectrometer of the L3 at the Large Electron Positron (LEP) collider at CERN [46]. They are successfully used in BELLE [47], BaBar [48, 49], BESIII [50], ALICE-Muon [51], and several other LHC experiments (ATLAS, CMS, etc.) [52, 53, 54, 55, 56]. Different cosmic ray experiments *e.g.* ARGO-YBJ [57, 58], COVER-PLASTEX [59], Daya Bay [60] also using RPCs for the muon detection. RPCs are used in neutrino experiments *e.g.* OPERA, where its good tracking capabilities and excellent time resolution are explored [61]. The RPCs are also being exploited for use in the TOF-PET imaging [62], detection of uncharged neutrons [63, 64] and γ-rays [65] over a large area.

Conventionally the RPCs are made up of high resistive electrode plates (*e.g.* glass, bakelite, etc.) having bulk resistivity $\sim 10^{10}$ -10^{11} Ω cm, which help to contain the cluster of electrons created by the passage of charged particles or ionising radiation in the gas volume. To collect the resulting induced signals, pickup strips are used. Typical time resolution for a single gap RPC is $\sim$ 1 - 2 ns [66, 67]. The time resolution in such a detector can be reduced to $<$ 100 ps, by reducing the gas gaps between the electrode plates or by using a multi-gap configuration [68, 69].

The RPCs are operated in two modes, viz., the avalanche mode and the streamer mode [70]. In avalanche mode, it can typically handle particle flux $\sim$ 10 kHz/cm^2 [71]. In the streamer

mode of operation, the amount of charge produced in a cluster is considerably larger, that creates induced signals of a larger magnitude. In this mode, the recovery time is larger and the irreversible damage caused by the accumulated charge reduces the life of the RPC detector. However, several remedial measures are taken to prolong its life time under the streamer mode of operation. Careful choice of electrode materials, smoothness of the inner surfaces of the electrodes to avoid localisation of excess charges, surface treatment of the inner sides of the electrode plates to reduce the surface resistivity, or providing alternate leakage paths for post-streamer recovery are adopted in the major HEP experimental collaborations.

In the proposed India-based Neutrino Observatory (INO), the RPCs have been chosen as the prime active detector for muon detection in an Iron Calorimeter (ICAL) [72]. A 50 kton ICAL is expected to consist of about 27000 RPC modules of dimension 2 m $\times$ 2 m. Lots of R&D on Resistive Plate Chamber (RPC) are being carried out both using glass and bakelite for the future India-based Neutrino Observatory (INO) [67, 73, 74, 75, 76, 77, 78, 79].

2.8 Open questions

We are now standing about 40 years after the invention of RPC in 1981. A lot of R&D on the basic characteristics are done. Some long-term behaviour studies are also performed in different experiments. Most of the results are predicted well with the existing theory and are well established now. There is huge number of scientific publications also on new design ideas, principles of operations, characterisation, and performance studies. Many more are coming in recent days. There are still many more open questions remaining still to be answered. Some future prospects, both on hardware and simulations, are discussed below in a very brief way.

2.8.1 Hardware

Ageing study : People have learned something about the ageing of the RPCs, but still, there is no solid conclusion exists. As we are moving toward large experiments, high interaction rates in the ageing study seem to be a crucial factor. How the ageing effect the detector materials, the ageing due to gas and linseed oil interactions, or the gas and electrode material interaction, and gas and spacers material interaction is still to be learned by us.

Optimisation of gas mixture : One of the essential tasks is to find a new and suitable gas mixture for the RPCs. Tetrafluoroethane gas causes a tremendous greenhouse effect. Another component is Sulphur Hexafluoride which is very expensive and also causes global warming. Many R&D is going on, but we are still apart from any solid conclusion. Though some eco-friendly gas mixtures based on HFO are showing promising results, the long-term effect is still unknown.

Suitable material : Though several prototypes have been tested with different materials, a suitable material is still not found. We can not conclude about the specific resistivity needed for RPC. Same as the previous, we are still unable to say about the thickness of the electrodes and the proper dielectric conductivity of the material needed. The major concern is to develop the techniques for large-size material production with proper configuration.

Material characterisations : A complete thorough study should be done on the variation of performance of the detector with bulk resistivity of the electrode plates, oil coating technique, the coated oil thickness, and surface morphology. Also, performance variation with the coating thickness is to be studied. Complete knowledge of the variation of resistivity due to high rate environment and long-term operation is still missing.

Optimisation of electronics : Electronics always play a major role in gaseous detectors. Proper optimisation of the electronics and the detector is needed as we are moving towards the high rate and high luminosity experiments. In the avalanche mode, the signal amplitude is very low and needs proper amplification. This amplification needs better accuracy for proper detection of the signal. Compared to that, in streamer mode, RPC can generate large signals of some pC to few nC. This huge amount of charge can damage sensitive electronics. So, in streamer mode, little or no amplification is needed. Depending on the specific application, we must choose good electronics with proper bandwidth.

New geometry : As the resistive electrode is spark-protective, we can dream of a new type of detector geometry. Micro-pattern detectors offer good rate handling capabilities, and parallel plate detectors offer good position and time resolutions. Maybe in the future, a hybrid detector

can be designed that can offer both good resolutions and can be operated at a high rate. Some people are already exploring the feasibility of using resistive electrodes in micro-pattern detectors. So, in the near future, we can expect a spark-protected micro-pattern detector.

Technology development : Different materials have been tested satisfactorily with the small prototype. For future upcoming experiments, more large-size detectors are needed. Technological development is essential for the production of large-size and uniform material production.

2.8.2 Simulation

Gas properties study : As the finding of a suitable gas mixture is crucial, the study of transport phenomena in new gases is important. If there is any interaction with oil coating to the gas mixture can be interesting to study.

Oil coating optimisation : The properties of linseed oil and its behaviour in high interaction rate are unknown to the community. The study of polymerisation phenomena is very important to understand for the long-term operation of the detector. Coating thickness optimisation is still not done. Simulating all these may shed some light on new directions and techniques.

It can also be explored if we can find any other replacement for linseed oil. Maybe by finding any suitable replacement, we can mitigate the polymerisation effect. We may get new ideas about the coating technique that is still to be developed.

Mode of operation : Some theories exist for the Avalanche mode operation of RPCs. Theory predicts well the avalanche formation in the gas gap. But the avalanche to streamer transition dynamics is still missing. Streamer mode operation is very critical, and no theories exist as of now for reliable prediction. Again the avalanche formation study in the different eco-friendly gas mixtures would be very appreciated.

Material optimisation : Different materials depending on the thickness and conductivity, are already simulated. Still, some critical study is not done. Particularly the study of leakage current has to be understood. The conduction current details in different electrodes are also unknown to the people.

Framework development : As of now, there is no single model framework only for the RPC. One can develop a common simulation model for RPC to understand the different dynamics of RPC in different states. Specifically, the study of behavioural change of RPC for long-term operation can then be possible through simulation.

Outside of these hardware and simulation activities in high-energy physics, RPC can be used for various societal applications. Among them, Positron Emission Tomography (PET) and Muon Tomography are very important and popular applications, and many R&D are going on. This detector can be suitable for homeland security applications, detection and determination of the position of flame and spark. Neutron detection is also possible with RPCs. It can also detect photons. The CALIC (Calorimeter for Linear Collider Experiment) group also built and tested Calorimeter based on the RPCs [81]. The revolution can happen if RPCs can be employed properly for medical imaging purposes. RPCs have the potential and several improvements that can replace classical scintillation-based detectors. As we can detect photons using this detector, X-ray photon counting is also possible, and in this way, we can provide a proper as low as possible X-ray dose to the patients. Already a Swedish company has built a low-dose mammographic device with high-rate narrow gap RPCs, that is commercially available.

Researches are ongoing worldwide to address these open questions.

Bibliography

[1] E. Rutherford and H. Geiger (1908), Proceedings of the Royal Society (London), Series A, vol. 81, no. 546, pp. 141-161.

[2] G. Charpak *et al.*, Nucl. Inst. and Meth. A 62 (1968) 262.

[3] R. Santonico and R. Cardarelli, Nucl. Inst. and Meth. A 187 (1981) 377.

[4] F. Sauli, Nucl. Inst. and Meth. A 386 (1997) 531.

[5] `https://argo.na.infn.it/`

[6] P. Bernardini *et al.*, Proc. of 29th International Cosmic Ray Conference Pune (2005) 6, 153.

[7] P. Bernardini *et al.*, Journal of Physics: Conference Series 120 (2008) 062022.

[8] William R. Leo, Techniques for Nuclear and Particle Physics Experiments - 2nd edition. Springer-Verlag Berlin Heidelberg GmbH, 1994.

[9] Abbrescia M., Peskov V., and Fonte P., Resistive Gaseous Detectors. Wiley-VCH, 2018. ePDF ISBN: 978-3-527-69872-1.

[10] A. Sen *et al.*, 2020 JINST 15 C06055.

[11] G.C. Trinchero *et al.*, Nucl. Inst. and Meth. A 508 (2003) 102.

[12] A. Laso Garcia *et al.*, 2012 JINST 7 P10012.

[13] Y. Jin *et al.*, Nucl. Inst. and Meth. A 591 (2008) 411.

[14] Q. Li *et al.*, Nucl. Inst. and Meth. A 663 (2012) 22.

[15] P. Baesso *et al.*, 2013 JINST 8 P08006.

[16] U. Amaldi *et al.*, Nucl. Inst. and Meth. A 778 (2015) 85.

[17] G. Charpak *et al.*, 2009 JINST 4 P12007.

[18] https://en.wikipedia.org/wiki/Semimetal#:~:text=As%20semimetals%20have%20fewer%20charge,lower%20electrical%20and%20thermal%20conductivities

[19] L.M.S. Margato *et al.*, 2021 JINST 16 P07009.

[20] H. Raether, Electron avalanches and breakdown in gases. Butterworth, London, 1964.

[21] S. Bheesette, Design and Characterisation Studies of Resistive Plate Chambers, Ph.D. Thesis, 2009.

[22] G. Aielli *et al.*, 2016 JINST 11 P07014.

[23] A. Paoloni *et al.*, 2017 JINST 12 P05020.

[24] R. Ganai *et al.*, Nucl. Inst. and Meth. A 936 (2019) 505.

[25] E. Cerron Zeballos *et al.*, Nucl. Inst. and Meth. A 373 (1996) 35.

[26] Appl. Sci. 2021, 11, 111. https://dx.doi.org/10.3390/app11010111

[27] P. Fonte *et al.*, Nucl. Inst. and Meth. A 602 (2009) 850.

[28] P. Fonte et al., Nucl. Instr. and Meth. A 449 (2000) 295.

[29] S. K. Park *et al.*, 2012 JINST 7 P11013.

[30] G. L. Alberghi *et al.*, 2019 JINST 14 C06007.

[31] G. Saviano *et al.*, 2018 JINST 13 P03012.

[32] A. Bianchi *et al.*, 2019 JINST 14 P11014.

[33] R. Guida *et al.*, Nucl. Inst. and Meth. A 958 (2020) 162073.

[34] G. Proto *et al.*, 2021 JINST 16 C02001.

[35] G. Bressi *et al.*, Nucl. Inst. and Meth. A 261 (1987) 449.

[36] http://www.lnf.infn.it/esperimenti/fenice.html

[37] M. Abbrescia *et al.*, Nucl. Inst. and Meth. A 336 (1993) 322.

[38] Yu. N. Pestov, Nucl. Inst. and Meth. A 196 (1982) 45.

[39] W. B. Atwood *et al.*, Nucl. Inst. and Meth. A 206 (1983) 99.

[40] M. Anelli *et al.*, Nucl. Inst. and Meth. A 300 (1991) 572.

[41] Gy. L. Bencze *et al.*, Nucl. Inst. and Meth. A 340 (1994) 466.

[42] R. Cardarelli *et al.*, Nucl. Inst. and Meth. A 263 (1988) 20.

[43] A. Blanco *et al.*, Nucl. Inst. and Meth. A 513 (2003) 8.

[44] M. Spegel *et al.*, Nucl. Inst. and Meth. A 453 (2000) 308.

[45] E. Cerron Zeballos *et al.*, Nucl. Inst. and Meth. A 374 (1996) 132.

[46] M. Alviggi *et al.*, Nucl. Inst. and Meth. A 456 (2000) 113.

[47] A. Abashian *et al.*, Nucl. Inst. and Meth. A 479 (2002) 117.

[48] BaBar Technical Design Report, BaBar Collaboration, SLAC Report SLAC-R-95-457, March 1995.

[49] F. Anulli, *et al.*, Nuclear Physics B (Proc. Suppl.) 61B (1998) 244.

[50] The BESIII Detector, IHEP-BEPCII-SB-13, IHEP, Beijing.

[51] A. Ferretti *et al.*, 2019 JINST bf 14 C06011.

[52] The ATLAS collaboration *et al.*, 2021 JINST 16 P07029.

[53] ATLAS Technical Design Report, Muon Spectrometer, CERN/LHCC/97-22, Geneva, 1997.

[54] G. Chiodini *et al.*, Nucl. Inst. and Meth. A 581 (2007) 213.

[55] CMS Collaboration, Muon Project, CERN/LHCC 97-32.

[56] CMS - Technical Proposal, CERN/LHCC/94-38, December 1994.

[57] P Bernardini and (for the ARGO-YBJ Collaboration) 2008 J. Phys.: Conf. Ser. 120 062022.

[58] G. Aielli *et al.*, Nucl. Inst. Methods. A 562 (2006) 92.

[59] G.A. Agnetta *et al.*, Nucl. Inst. and Meth. A 381 (1996) 64.

[60] Q. Zhang *et al.*, Nucl. Inst. and Meth. A 583 (2007) 278.

[61] M. Guler *et al.*, OPERA, an appearance experiment to search for ν_μ-ν_τ oscillations in the CNGS beam, CERN/SPSC 2000-028.

[62] M. Couceiro *et al.*, Nucl. Inst. and Meth. A 580 (2007) 915.

[63] M. Abbrescia *et al.*, Nucl. Phys. B (Proc. Suppl.) 125 (2003) 43.

[64] M. Abbrescia *et al.*, Nucl. Inst. and Meth. A 506 (2003) 101.

[65] P. Camarri, Nucl. Inst. and Meth. A 572 (2007) 476.

[66] A. D. Bhatt *et al.*, Nucl. Inst. and Meth. A 844 (2017) 53.

[67] S. Biswas *et al.*, Nucl. Inst. and Meth. A 617 (2010) 138.

[68] P. Fonte *et al.*, Nucl. Inst. and Meth. A 449 (2000) 295.

[69] A. Blanco *et al.*, Nucl. Inst. and Meth. A 535 (2004) 272.

[70] G. Bruno, Eur Phys. J. C 33 (2004) s1032.

[71] R. Arnaldi *et al.*, Nucl. Physics B (Proc. Suppl.) 78 (1999) 84.

[72] INO Project Report, INO/2006/01, June 2006, ⟨http://www.imsc.res.in/∼ino/⟩.

[73] V.M. Datar *et al.*, Nucl. Inst. and Meth. A 602 (2009) 744.

[74] S. Biswas *et al.*, Nucl. Inst. and Meth. A 602 (2009) 749.

[75] S. Biswas *et al.*, Nucl. Inst. and Meth. A 604 (2009) 310.

[76] S. Biswas *et al.*, Nucl. Inst. and Meth. A 661 (2012) S94.

[77] K.K. Meghna *et al.*, 2012 JINST 7 P10003.

[78] K.K. Meghna *et al.*, Nucl. Inst. and Meth. A 816 (2016) 1.

[79] S. Chakraborty *et al.*, Nucl. Inst. and Meth. A 936 (2019) 424.

[80] S. Biswas, Development of High Resolution Gas Filled Detector for High Energy Physics Experiments, Ph.D. Thesis, 2010.

[81] M. Chefdeville *et al.*, The CALICE Collaboration, Nucl. Inst. and Meth. A 939 (2019) 89.

Chapter 3

R & D of bakelite RPC

The main goal of this study is the systematic R&D of the RPC detector for the 3^{rd} and 4^{th} station of the Muon Chamber (MuCh) of CBM experiment. Bakelite sheets, commercially available in India, have been explored to build the RPC modules. Electrical properties of different grades of bakelite plates are studied. Prototype detectors are tested for efficiency, noise rate, and time resolution, using cosmic rays with different gas mixtures. Radiation hardness is also tested using gamma source in the laboratory. All the details of the fabrication of modules, systematic development, experimental setup, different measurements and test results are discussed in this chapter.

3.1 Measurement of the volume (or bulk) resistivity of the material

The bulk resistivity of the bakelite plate is measured by the two probe method. A sample piece of the electrode material of dimension 3 cm $\times$ 3 cm is cut from a large bakelite sheet. Two small square pieces of copper tape (the dimension of each tape is 2.5 cm $\times$ 2.5 cm) are pasted on two opposite surfaces of the bakelite sample. The voltage is applied between two copper tapes and the corresponding current is noted. Both the voltage and current readings are noted from the display attached in the power supply. From Ohm's law, the resistance is calculated and subsequently the resistivity is calculated using formula 3.1.

$$R = \frac{V}{I} = \frac{\rho l}{A}; \quad \Rightarrow \quad \rho = \frac{VA}{Il}; \tag{3.1}$$

Where V is the applied voltage, I is the measured current, l is the thickness of the sample and A is the cross sectional area of the sample through which current is flowing.

The circuit diagram for the bulk resistivity measurement is shown in Figure 3.1 and the experimental setup is shown in Figure 3.2.

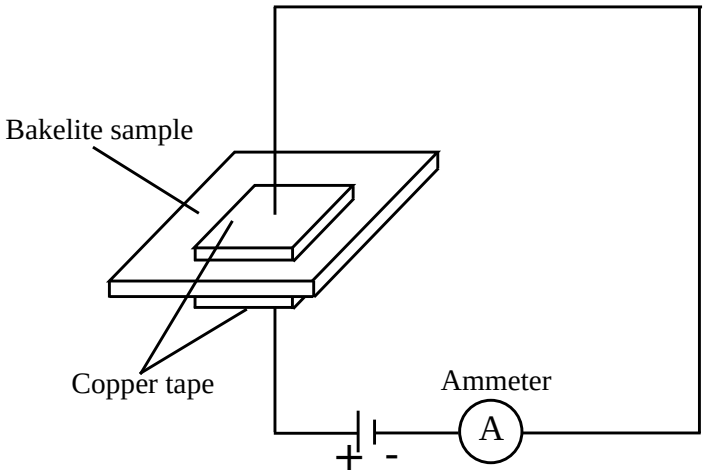

Figure 3.1: Circuit diagram for the bulk resistivity measurement

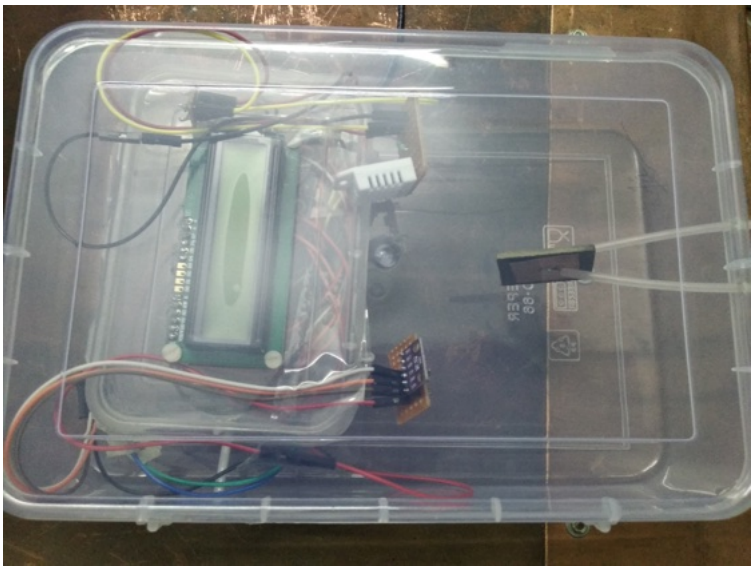

Figure 3.2: Measurement setup for the bulk resistivity

The bulk resistivity is shown as a function of applied voltage for two bakelite samples in Figure 3.3. It is found that the bulk resistivity of sample 1 is $\sim 2 \times 10^{11}$ Ω cm at a temperature $\sim$ 22 °C and relative humidity $\sim$ 60%, whereas for sample 2, the bulk resistivity is $\sim 3 \times 10^{10}$ Ω cm at the same temperature and relative humidity.

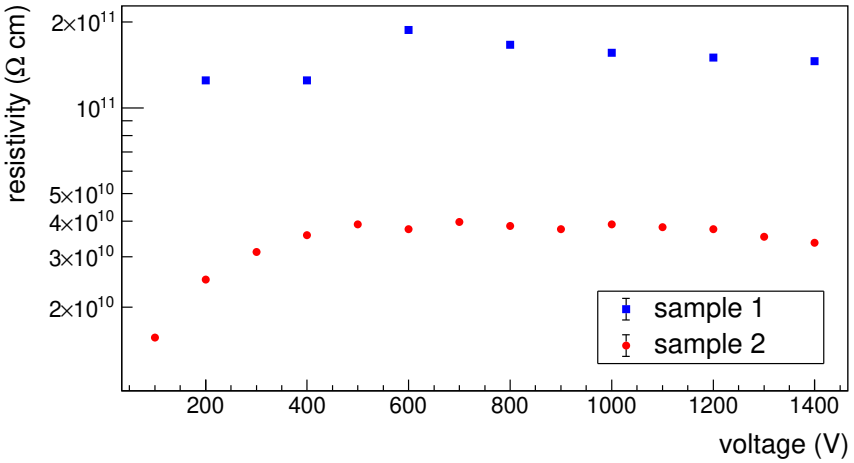

Figure 3.3: Bulk resistivity as a function of applied voltage for two different samples. Error bars are smaller than the marker size

Two samples are obtained from two different companies. Sample 1 is brown in colour and sample 2 is a white coloured material with more glossy surface compared to the sample 1. Since two materials are obtained from two different companies their compositions (the bakelite sheets are phenolic resin bonded paper laminates) are not exactly same. That is why there is a difference of about one order of magnitude in the bulk resistivity. It is observed from Figure 3.3 that in two samples resistivity varies with voltage differently. However, in sample 2 the variation of resistivity with voltage is more prominent. The performance of the detector does not depend on such a small variation (2×10^{11} - 4×10^{11} Ω cm) of bulk resistivity. Such variations of different materials are also reported earlier [1].

3.2 Fabrication of detector

Two bakelite plates, each of dimension 30 cm $\times$ 30 cm and thickness 2 mm, are separated by 2 mm spacers made of polycarbonate (resistivity $\sim 10^{15}$ Ω cm). Four edge spacers of dimension 30 cm $\times$ 1 cm and one button spacer of diameter 1 cm at the middle are glued on one plate using

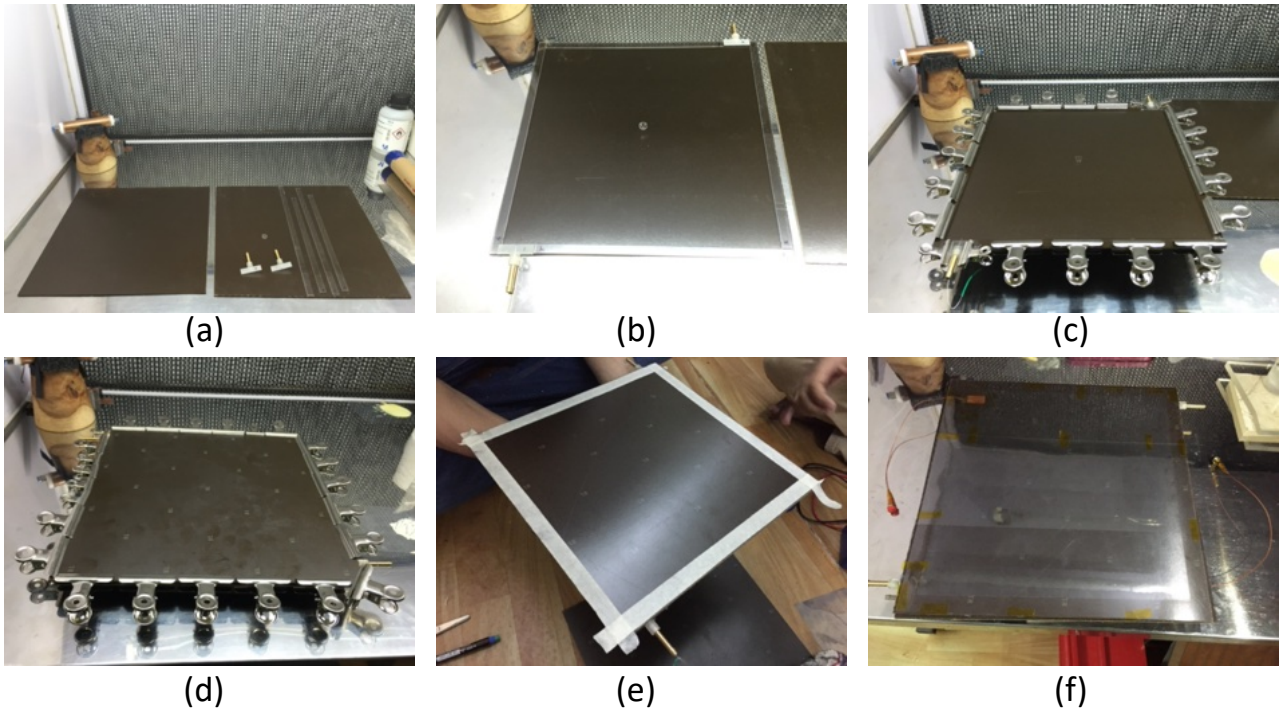

Figure 3.4: (a) Components of RPC, (b) Spacers are placed for marking on one bakelite plate before gluing, (c) Gluing of spacers and nozzles on one plate, (d) Gluing of the second plate to complete the gas gap, (e) Masking for the graphite coating, (f) Complete RPC with graphite coating, covering with the mylar sheet and connecting the HV lead

Araldite epoxy adhesive. The glued plates are kept for 24 hours for curing. Two gas nozzles, also made of polycarbonate, are used for the gas input and output and they are also used as a part of the edge spacers. The other bakelite plate is glued on it to complete the gas gap and kept for curing again for 24 hours. A thin layer of graphite is applied to the outer surfaces of the electrode plates for the distribution of voltage. Two 1 cm $\times$ 1 cm copper tapes are pasted on two diagonally opposite corners on the graphite layer to apply the high voltage (HV). HV of opposite polarities are applied on two sides. The components of the detector, different steps of fabrication and complete RPC module are shown in Figure 3.4. After building the chamber, the leak is checked by the water displacement method. No significant leak is found.

Copper pick-up panels are used to collect the signals. Pick-up panels are made of 2.5 cm wide strips with a separation of 2 mm between two consecutive ones. 100 μm thick copper tapes are pasted on one side of a 2 mm thick G-10 board and the ground plane is made with aluminium foil of thickness 10 μm on the other side of the G-10 board. Usually the G-10 board

is taken having the same dimension of the RPC chamber under test. The length of each copper strip is made the same as that of the RPC. Finally, both the copper and aluminium sides are wrapped with a 100 μm thick mylar foil. The signals from the strips are collected through RG-174/U coaxial cables. The strips and the ground plane of a typical pick-up panel are shown in Figure 3.5.

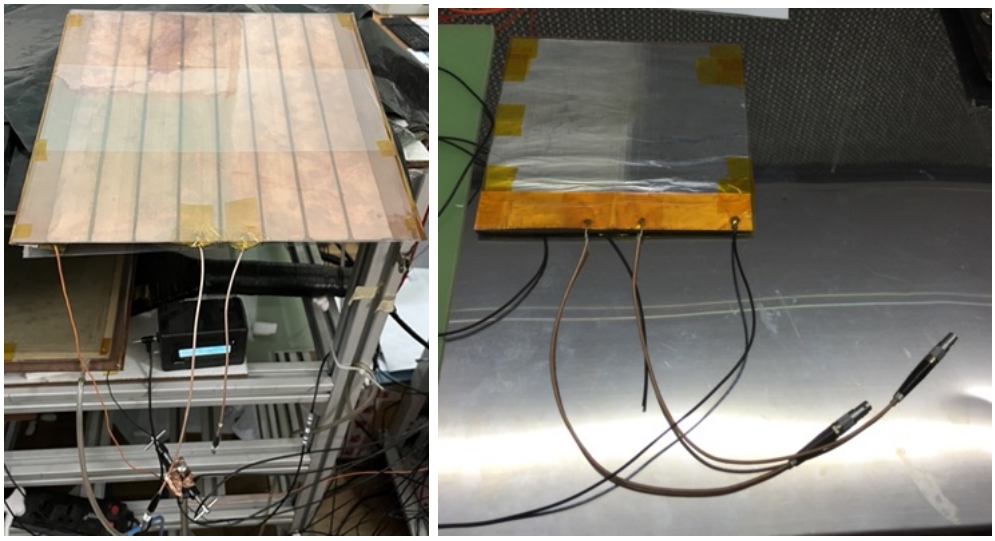

(a) (b)

Figure 3.5: (a) Pick-up strips made of copper, (b) Ground plane made of aluminium

3.2.1 Leak Test of the Detector

After fabrication of the detector, leak test is done using the water displacement method to ensure that no leak is there in the chamber. A Tygon tube has been employed as the U-tube and water is poured into it. A gas cylinder is connected from one end of the detector while the other end is connected to the U-tube. A small amount of gas is flown from the gas cylinder and immediately after this the gas inlet end is closed to create a small overpressure (a few millibars) inside the detector. The water height difference between the two arms of the U-tube is measured as a function of time. It is seen that the pressure difference decreases with time. The arrangement and results are shown in Figure 3.6(a) and 3.6(b) respectively.

From Figure 3.6(b) it is seen that the pressure difference between the U-tube arms is decreasing with time. Gas leak rate is defined as $V\frac{dp}{dt}$. Where V is the volume of the container, dp is the pressure difference and dt is the change in time.

Initially the leak rate for this chamber is found to be - 0.22 mbar*l/min whereas that after some time it reduces to - 0.01 mbar*l/min. Actually this measured non zero leak rate depends not only because of small leaks in the chamber but also on the number of junctions in the gas line. This much of leak rate is acceptable for such a detector. However, it is expected that for a system consist of metal tubings the leak rate will be smaller.

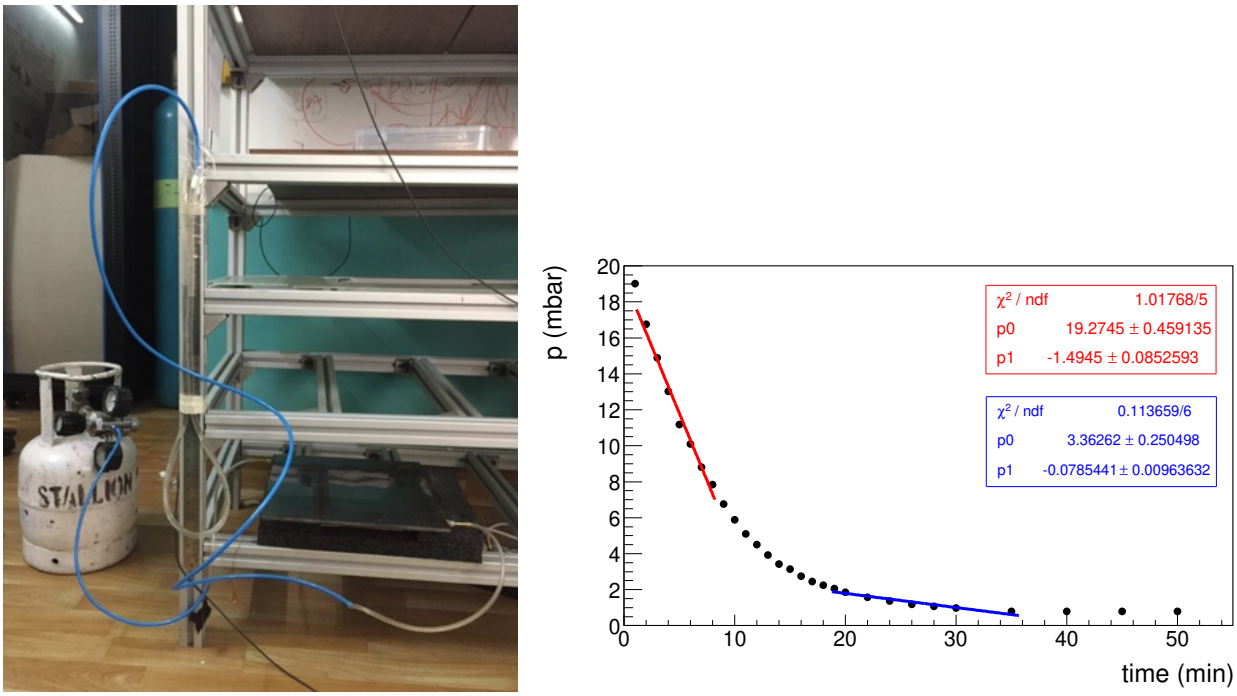

(a) (b)

Figure 3.6: (a) Setup for leak test (b) Pressure difference as a function of time

3.2.2 Surface resistivity measurement of the graphite coating

As mentioned in section 3.2, graphite layers are coated on both the outer sides of the chamber for the distribution of the HV over the outer surfaces of the module. After making the chamber, the surface resistivity of the graphite layers are measured. For this measurement, one H-shape metallic jig made of aluminium bar is employed. The length and the separation between the two aluminium bars of the jig are kept at 3 cm. The aluminium bars are separated by the G-10 insulator (bulk resistivity $> 10^{14}$ Ω cm). A little pressure is applied onto the jig so that it properly touches the surface under study. Two probes of a multimeter are connected to the aluminium bars and the resistance is measured. In Figure 3.7 the surface resistivity,

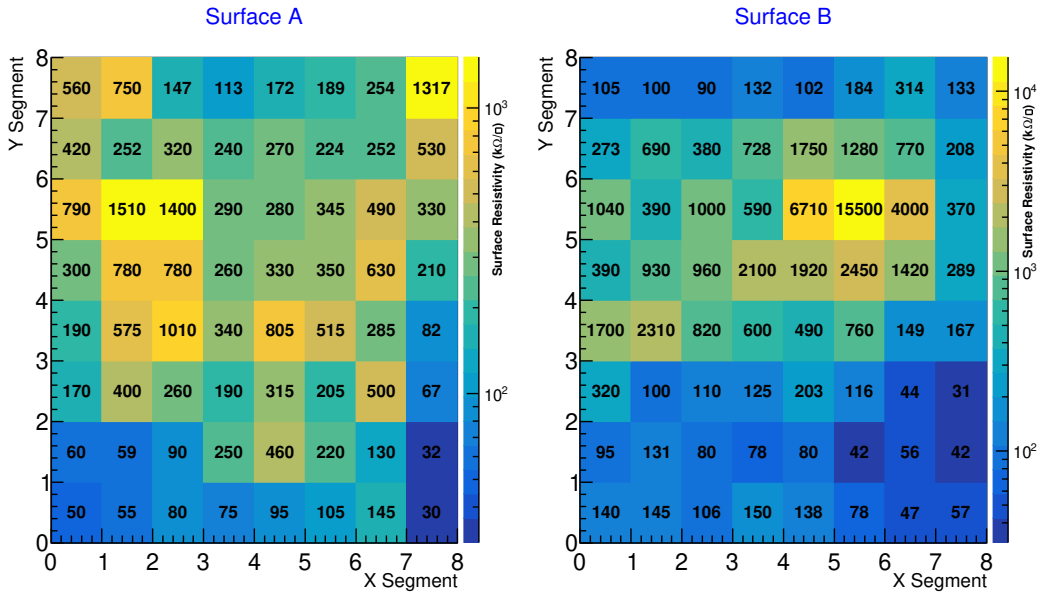

Figure 3.7: Surface resistivity of the outer sides of the bakelite RPC

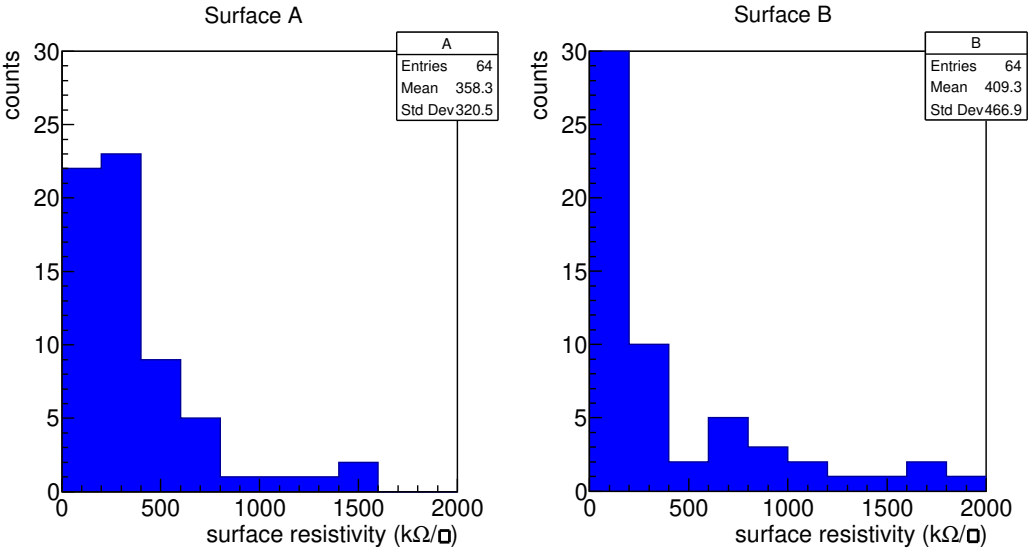

Figure 3.8: Surface resistivity distribution of graphite coating of the outer surfaces of the RPC

measured on two outer surfaces of the first module, is shown and the distributions are shown in Figure 3.8. The average surface resistivity of surface A and surface B of the chamber are found to be $\sim$ 358 k$\Omega/\square$ and $\sim$ 409 k$\Omega/\square$ respectively.

3.3 I-V characteristics

The work is initiated by a study of the characteristics of the first module using a non-conventional RPC gas mixture of Ar/CO_2 in 70/30 volume ratio. To check the detector response, first the I-V characteristics are studied. The I-V characteristic curves, as obtained on different days in May and June of 2019, are shown in Figure 3.9. For each set of data, the temperature and the relative humidity (RH) are also monitored. The RH range and average temperature of each data set is shown in Figure 3.9. From Figure 3.9, it is seen that due to the Ar/CO_2 gas mixture, the breakdown occurs at a comparatively lower voltage. In normal RPC gas mixtures, *e.g.* Tetrafluoroethane mixed with Iso-butane, the breakdown occurs at around 6 - 8 kV. Although, initially the breakdown is seen at about 4 kV but some abnormal behaviour is also observed later on. At 5 kV a typical signal of amplitude $\sim$ 20 mV with a rise time of 10 ns is observed in the oscilloscope with 10 mV/div, 100 ns/div, 50 Ω terminations and shown in Figure 3.10.

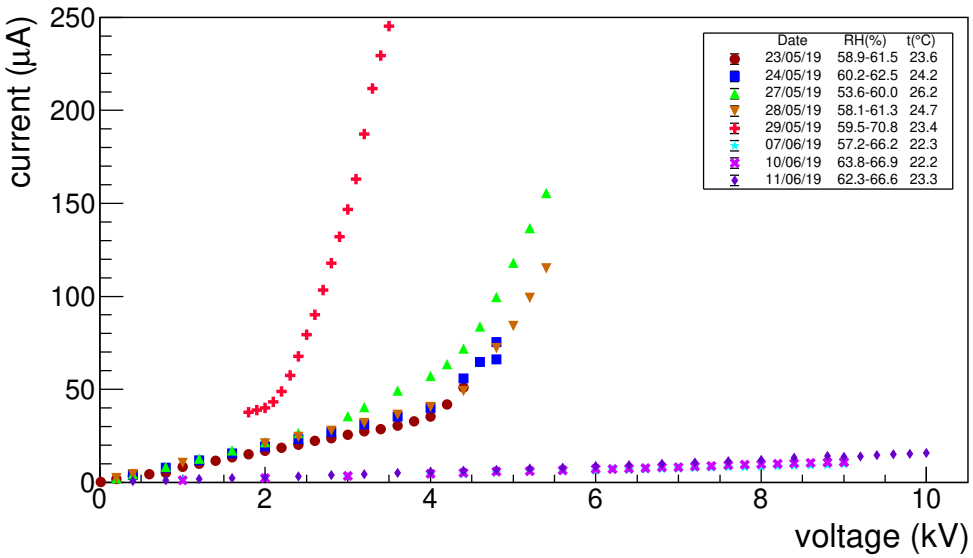

Figure 3.9: I-V Characteristics with Ar/CO_2 gas mixture in 70/30 volume ratio measured on different days. Error bars for the current are smaller than the marker size

The induced RPC signals from the pick-up strips are put to a 10x fast amplifier and the amplified signals are fed to a leading edge discriminator (LED). The LED signals are counted by a NIM scaler. The noise rate (or the singles count rate) is defined as the number of pulses obtained per unit time per unit area of the pick-up strip.

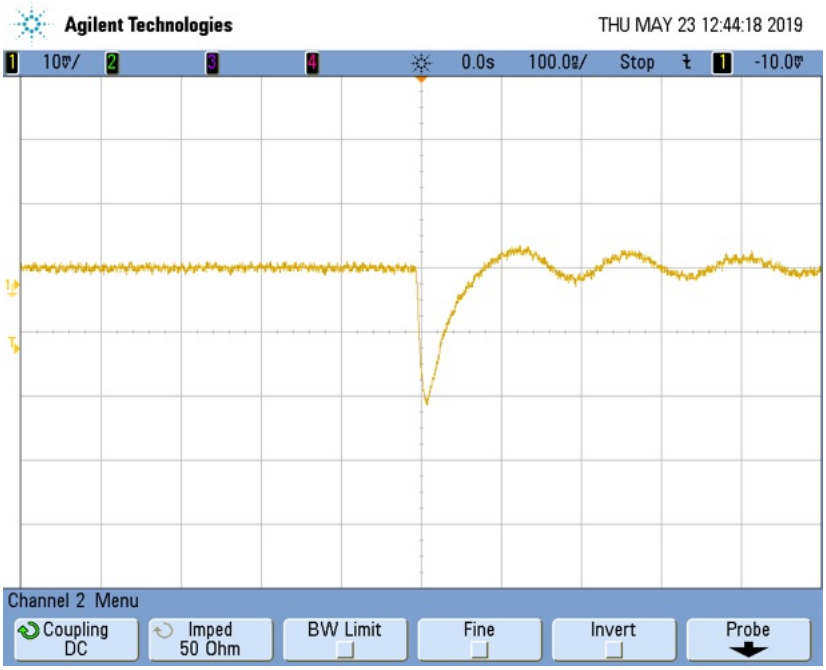

Figure 3.10: Typical induced pulse on a pick-up strip at 5 kV observed in the oscilloscope with 10 mV/div, 100 ns/div and 50 Ω termination for Ar/CO_2 gas mixture in 70/30 volume ratio

The noise rate as a function of the voltage is also measured on two different days keeping the threshold to the discriminator at - 15 mV and is shown in Figure 3.11. It is seen that the noise rate follows the same trend as that of the leakage current.

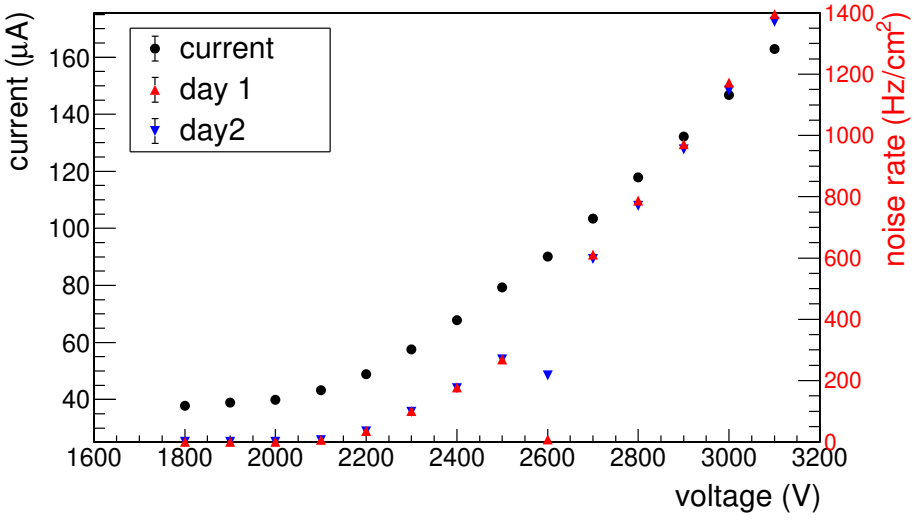

Figure 3.11: Current and noise rate as a function of the applied voltage. Error bars are smaller than the marker size

Using the 3-fold coincidence signal from the scintillator as a trigger, the efficiency of this RPC prototype is measured with cosmic muons using conventional NIM electronics (the detailed procedure is described in section 3.4.1 and 3.6.1.1). A maximum efficiency $\sim 5\%$ is achieved which is not at all acceptable for any experiment.

After a few days, the detector shows an ambiguous nature of I-V characteristics as shown in Figure 3.9. As a result, we moved to build a second module with a different bakelite grade.

3.4 Further development

The second module is built with bakelite plates having the bulk resistivity $\sim 3\times\ 10^{10}\ \Omega$ cm. The surface resistivity of the graphite layers is measured to be $\sim 500\ k\Omega/\square$ for both the sides.

3.4.1 Efficiency and noise rate measurement

The signals from the pick-up strips of the RPC module are fed to a 10x fast amplifier and then to the LED. The cosmic ray master trigger is made using three fast plastic scintillators. Among them, two scintillators (with dimensions 10 cm $\times$ 10 cm (SC 1) and 2 cm $\times$ 10 cm (SC 2) respectively) are placed above the RPC module and one (with dimension 20 cm $\times$ 20 cm (SC 3)) is placed below. The scintillators make a trigger window of area 2 cm $\times$ 10 cm (area of the finger scintillator SC 2). Thresholds to the discriminators are set to - 15 mV for all the scintillators and also for the RPC. The width of the 3-Fold scintillator master trigger is set at 150 ns. Finally, the discriminated RPC signal from one single strip under the finger scintillator is taken in coincidence with the 3-Fold master trigger and a 4-Fold NIM signal is obtained. The ratio of the 4-Fold signal and the 3-Fold scintillator signal is defined as the efficiency of the detector. The single RPC signals are also counted for a particular duration and the noise rate is defined as the number of single counts per unit time per unit area. Figure 3.12 shows the schematic of the cosmic ray test set-up for the RPC module. The arrangement of the scintillation detectors and the RPC in the cosmic ray test bench is shown in Figure 3.13 and the electronic modules used in this study is shown in Figure 3.14.

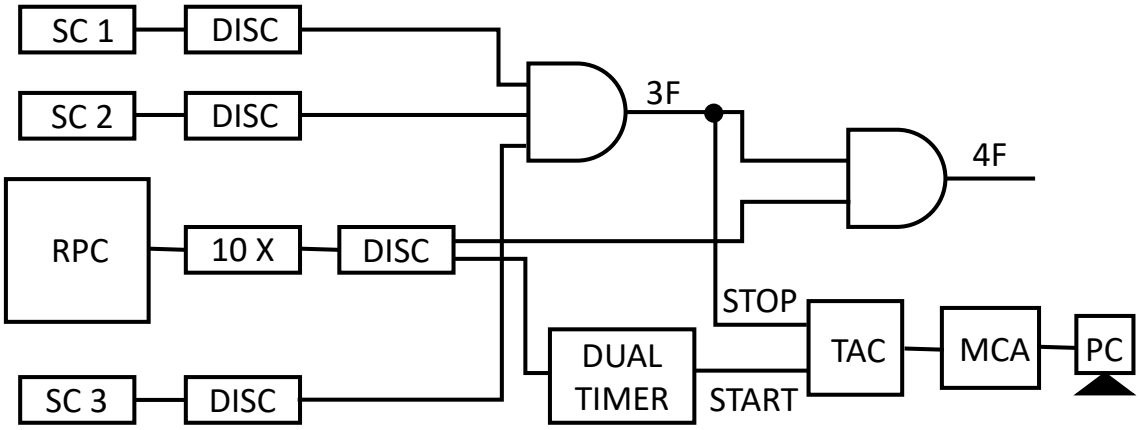

Figure 3.12: Schematic representation of the cosmic ray test set-up. SC 1, SC 2 (Finger) and SC 3 are the plastic scintillators of dimensions 10 cm × 10 cm, 2 cm × 10 cm and 20 cm × 20 cm respectively. DISC, 10X, TAC, MCA and PC are the Leading Edge Discriminators (LED), 10x fast amplifier, Time to Amplitude Converter, Multi-Channel Analyser and Personal Computer respectively.

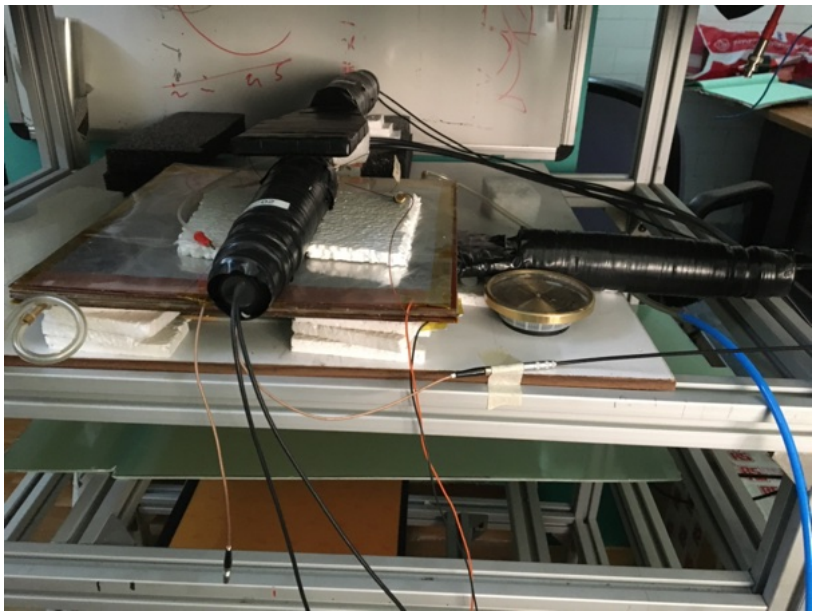

Figure 3.13: Arrangement of the scintillation detectors and the RPC in the cosmic ray test bench

The efficiency, noise rate, time difference of RPC signal and master trigger and the time resolution of the oil-less bakelite RPC prototype as functions of voltage are measured with cosmic rays. The detector current as a function of the bias voltage is shown in Figure 3.15 for two gas compositions; *i.e.* with 100% Tetrafluoroethane ($C_2H_2F_4$) and Argon/CO_2 mixture in the

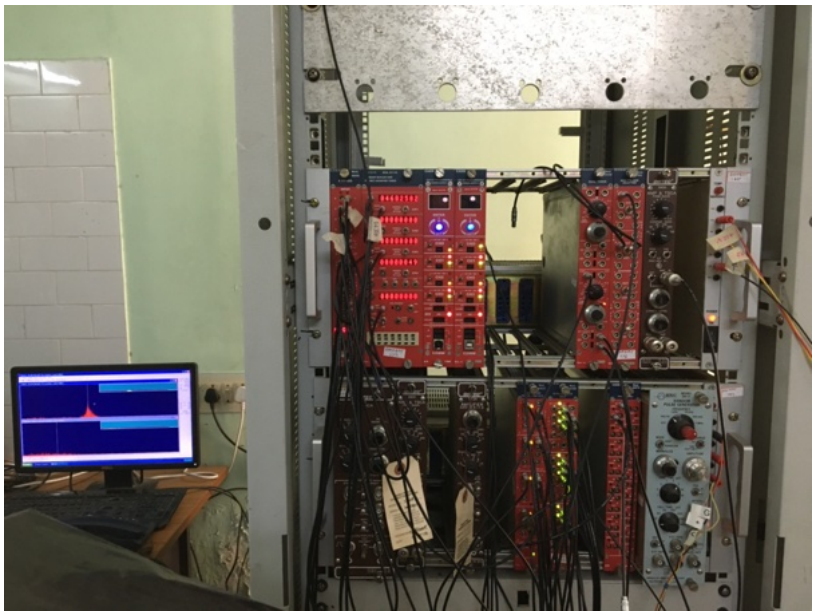

Figure 3.14: Electronic modules used in this study

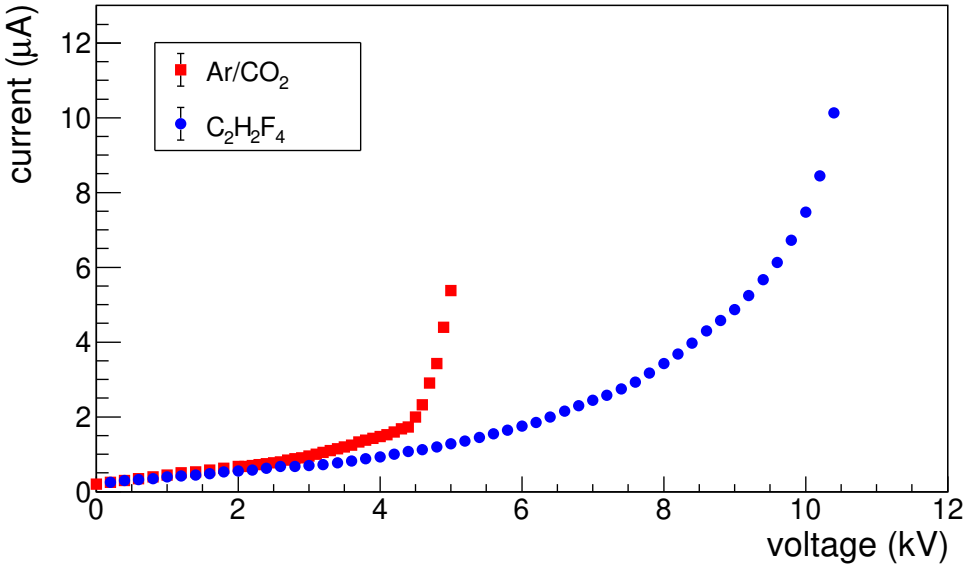

Figure 3.15: I-V characteristics of the second module with two different gas compositions. Error bars are smaller than the marker size

70/30 volume ratio. It is visible that for 100% $C_2H_2F_4$ initially the current increases slowly with the voltage and above 8 kV across the gas gap the increase becomes rapid. At a voltage difference of 8 kV across the gas gap, a signal of amplitude $\sim$ 10 - 15 mV is observed in the

oscilloscope at 50 Ω termination. A sharp breakdown in the I-V characteristics resulted with the Argon/CO_2 mixture also, but at a lower voltage compared to that with the 100% $C_2H_2F_4$.

For 100% $C_2H_2F_4$, the noise rate as a function of voltage is measured on two consecutive days keeping the discriminator threshold at - 15 mV; the results are shown in Figure 3.16. It is seen that on both days the noise rate increases with applied voltage but on the second day, the noise rate is found to be much less than that of the first day, because of better conditioning. The conditioning is done with a continuous gas flow with a voltage difference of 4 kV, kept across the gas gap overnight. It is to be mentioned here that, for conventional linseed oil treated RPCs, the noise rate with cosmic rays is found to be one order of magnitude lower in some cases [2] and even two orders of magnitude lower for RPCs with higher resistivity, when operated in the streamer mode [3, 4, 5].

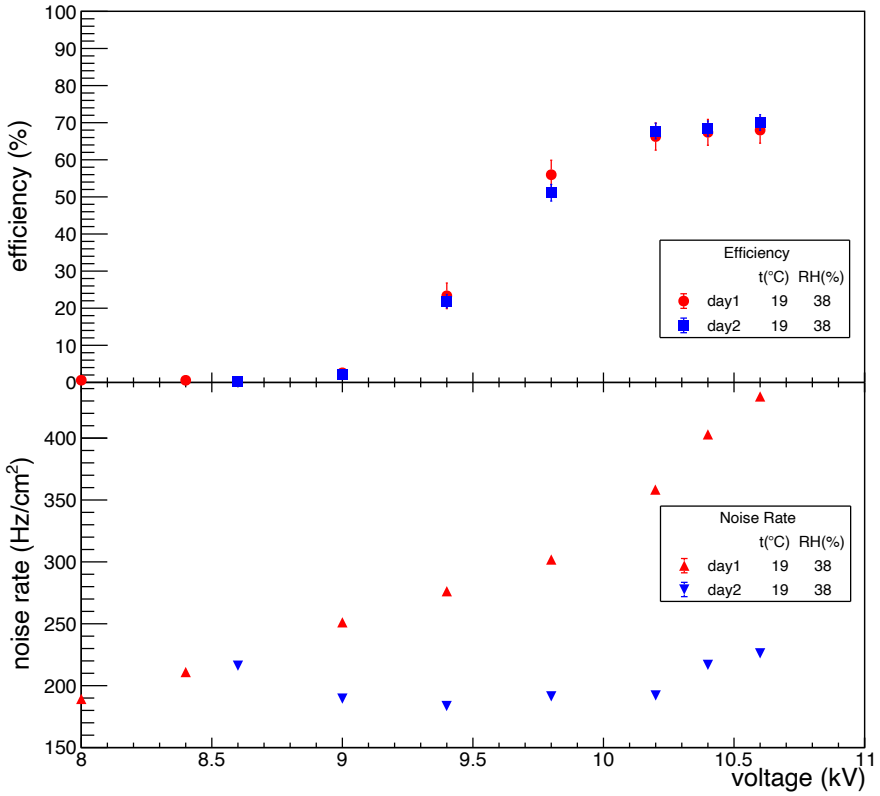

Figure 3.16: Efficiency and noise rate as a function of voltage for 100% $C_2H_2F_4$

From Figure 3.16, it can also be seen that the efficiency starts increasing from above 9 kV and saturates at a value of $\sim$ 70% from 10.2 kV onwards. The same result is observed for efficiency on both days.

3.4.2 Time resolution measurement

To measure the timing properties of the RPC, the same cosmic ray set-up is used. The discriminated RPC signal is stretched by a dual timer and used as the START signal of the Time to Amplitude Converter (TAC). The 3-Fold scintillator coincidence signal is taken as the STOP signal of the TAC. The output of the TAC is fed to the Multi Channel Analyser (MCA) and the spectra are stored in a Personal Computer (PC). Figure 3.12 shows the block diagram of the electronics set-up for time resolution measurement of the RPC module using cosmic rays.

During the whole measurement of the chamber, the temperature and relative humidity inside the laboratory are maintained at $\sim$ 18 - 20°C and 37 - 40% respectively whereas the atmospheric pressure is monitored to be 1009 - 1020 mbar.

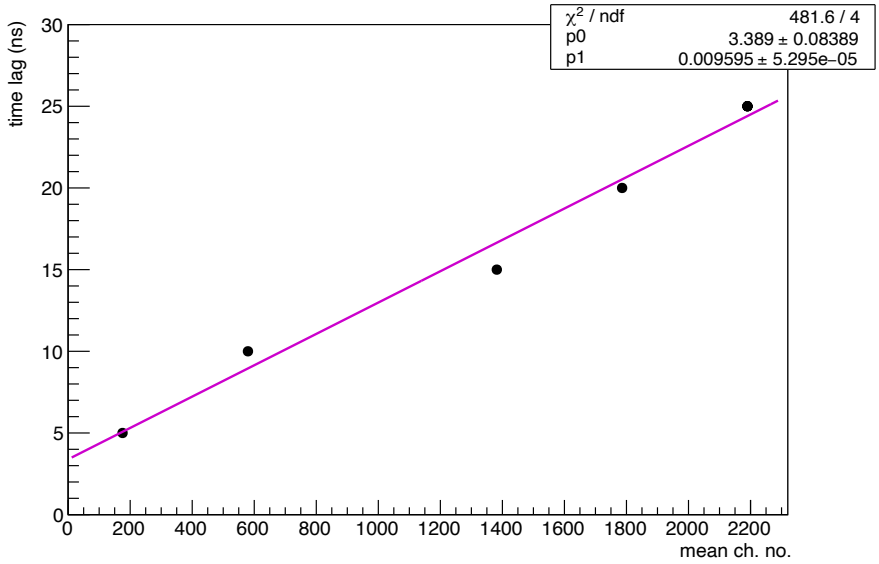

Figure 3.17: Calibration curve: Mean ADC channel no vs known delay (time lag)

While measuring the time resolution, the RPC signal is stretched to 500 ns in order to avoid the effect of double pulses or reflection pulses if there is any. The full scale of the TAC is set at 100 ns.

First, the TAC is calibrated applying known delay between the same signal splitted into two *i.e.* one signal from the LED is fed to the START of the TAC and other output of the same LED channel is fed to the STOP of the TAC after known delay. For each delay setting the

spectrum is stored. The calibration curve *i.e.* mean ADC channel no vs the delay in ns is shown in Figure 3.17.

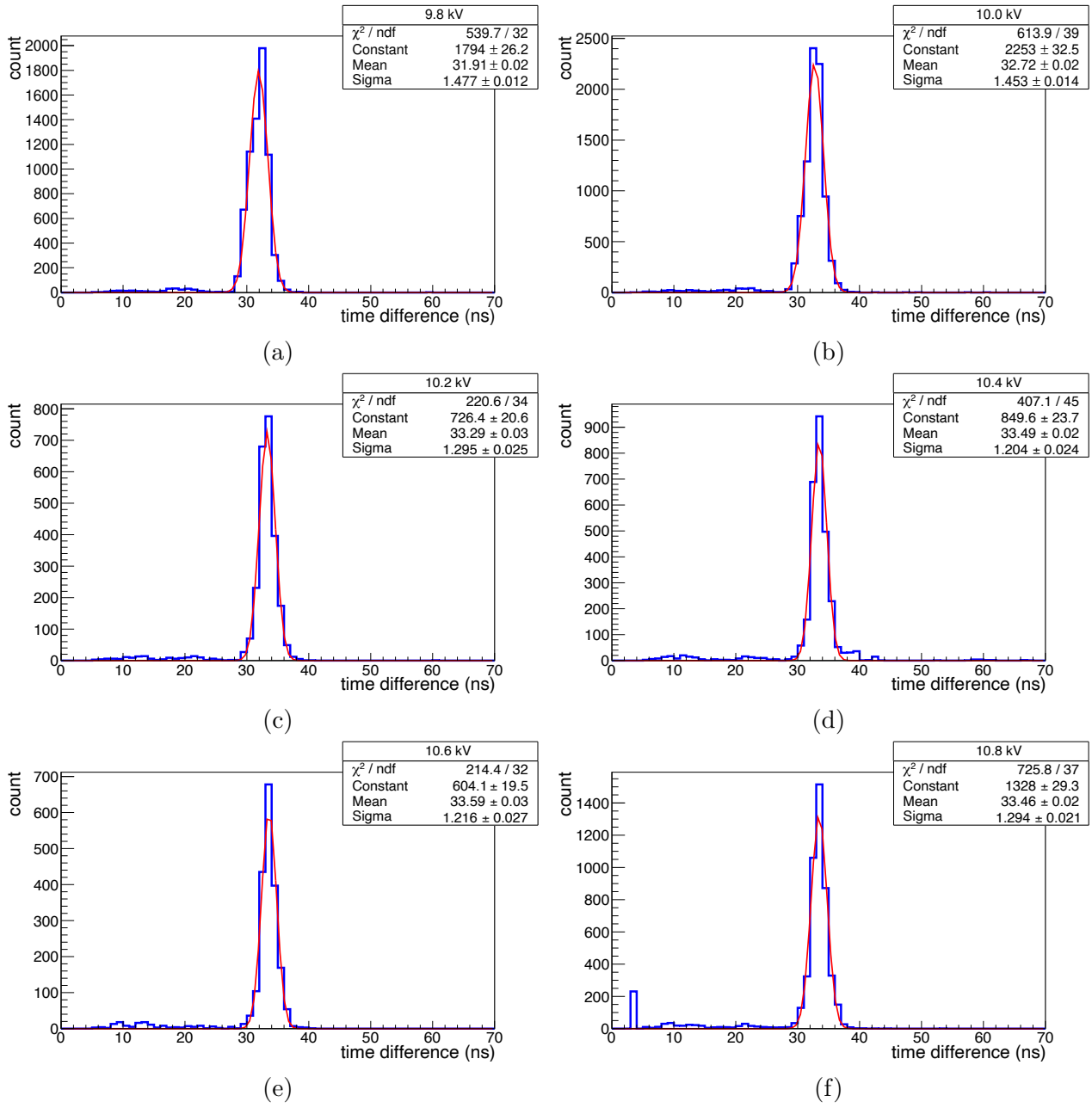

Figure 3.18: Time spectrum of RPC at different voltage differences across the gas gap for 100% $C_2H_2F_4$: (a) 9.8 kV (b) 10.0 kV (c) 10.2 kV (d) 10.4 kV (e) 10.6 kV (f) 10.8 kV voltage differences across the gas gap

The typical time spectra for the RPC are shown in Figure 3.18 for different voltage of the RPC. The distribution of the time difference between the RPC signal and the master trigger is fitted

with the Gaussian function. Finding the σ_{12} of the distribution and subtracting in quadrature the contribution from the scintillator, the intrinsic time resolution of the RPC is calculated[1]

The time difference of the RPC signal with respect to the master trigger and the time resolution (σ) of the RPC as a function of the applied voltage are shown in Figure 3.19 for 100% $C_2H_2F_4$. The RPC signal is used as the START signal and with the increase of the applied voltage the electric field inside the RPC becomes stronger, the electrons travel faster and the signals arrive earlier. As a result, with the increase of applied voltage, the time difference increases and reaches a plateau from 10.2 kV onwards. The time resolution (σ) decreases and a value $\sim$ 1.2 ns is obtained at 10.2 kV.

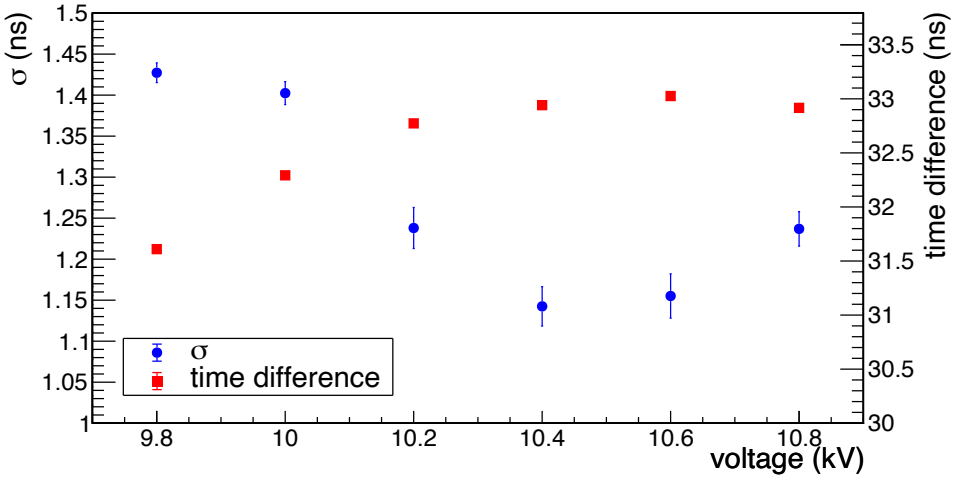

Figure 3.19: Time resolution and time difference of the RPC signal and the master trigger as a function of voltage for 100% $C_2H_2F_4$. Error bars for the time difference are smaller than the marker size

3.5 Linseed oil & bakelite electrode plates

Linseed oil is used for curing the bakelite electrode plates. It completely dried out and makes the surface more smooth. Some properties of linseed oil and the real life problems faced by people are discussed in the following sections.

[1]Let us consider σ_{12} is the combined time resolution for the RPC and the scintillator whereas σ_1 and σ_2 are the intrinsic time resolution for the RPC and scintillator respectively. So, σ_{12} is related to σ_1 and σ_2 as $\sigma_{12}^2 = \sigma_1^2 + \sigma_2^2$ and the intrinsic time resolution of the RPC is calculated as $\sigma_1 = \sqrt{\sigma_{12}^2 - \sigma_2^2}$.

3.5.1 Linseed oil

The linseed oil is a fatty acid (R-COOH), an organic acid that contains the glycerides of linolenic, linoleic, oleic, stearic, and palmitic acids with a high degree of unsaturation of its fatty acid radicals [6]. The structure of this compound is shown in Figure 3.20. It is extracted from flax seeds and appears yellowish in colour. Though flaxseed oil and linseed oil are both extracted from flax seeds, the processing techniques are different.

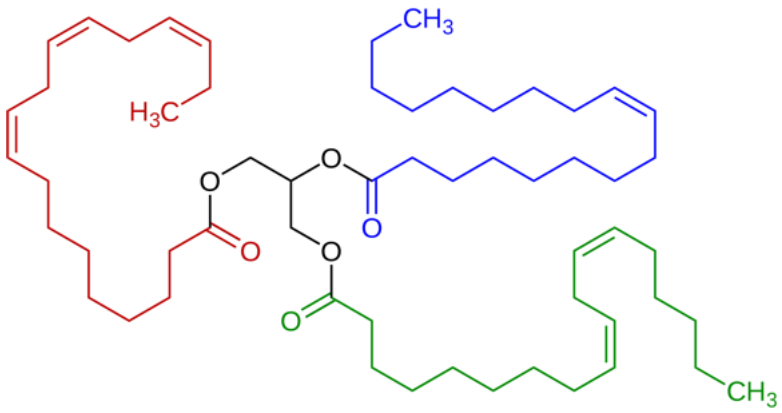

Figure 3.20: Structure of lineed oil. It is a triglyceride. It contains triply unsaturated α-linolenic acid (51.9 - 55.2 %), saturated acids palmitic acid ($\sim$ 7 %) and stearic acid (3.4 - 4.6 %), monounsaturated oleic acid (18.5 - 22.6 %), doubly unsaturated linoleic acid (14.2 - 17 %) [7]

This oil has drying properties due to polymer formation. It dries very slowly and uniformly over the surfaces. Thats why it is generally used in the wooden surfaces varnishing to give a glowing effect. This oil is also used in the painting that makes it more fluid and glossy. Linseed oil keeps materials, that are hydrophobic in nature, safe from water damage. Therefore, its principal application is found as drying oil in the paint and linoleum industries. Flaxseed is also a rich natural source of the omega-3 fatty acid and food-grade linseed oil is sometimes taken as a nutritional supplement for human body, and can be used in cooking.

As the oil contains di- and tri-unsaturated esters, it forms polymer in the presence of oxygen molecules in the air. This polymerisation makes a hard uniform layer over the surface which makes bakelite surface smoother. Though the oil layer looks dry, it is not fully cured and water vapour can bypass it almost completely.

3.5.2 Advantages of linseed oil coating

Many analyses are done also for electrode material study. An article by C. Lu [10] describes well about the surface structure study of the electrode materials.

Surface structure of the electrode plates is studied by Atomic Force Microscopy (AFM). In this article it is described that, "Pin" type defect is the most dangerous for bakelite plates. The study says that if rough surface structure is coated with thinned linseed oil, the surface becomes smoother and if the surface is coated with less thinned (diluted with 2-propanol) linseed oil then it becomes very smooth. Therefore, linseed oil coating plays a very important and crucial role for the bakelite plates. Oil coating removes the surface morphological defects by drying and forming a hard uniform layer over the entire surface. Thereby the electrode surface becomes less sensitive to field emission which is a source of high dark current and subsequently reduces the high single count rates / noise rates.

When a high potential difference is applied across the gas gap, a strong electric field is generated and it increases the photoelectric disturbance. The UV photons created, due to the avalanche or streamer, can reach and hit the electrode surfaces. But to reduce the high after-pulse / noise rate it is recommended to use the least UV sensitive materials as the electrode. Linseed oil has some intrinsic properties to quench UV photons. Therefore, an oil coating can reduce the UV sensitivity of bakelite materials and performance of the detector can be improved.

Hydrofluoric acid (HF) is produced within the RPC gas volume due to the decomposition of $C_2H_2F_4$ gas. $C_2H_2F_4$ is the major component for RPC gas mixtures for the avalanche mode operation. It is a chemical compound of hydrogen and fluorine. With the chemical reaction with water vapour it can produce HF acid. HF can corrode many different materials. To have some idea of such corrosive effects, various materials were dedicatedly exposed to the HF vapour environment. One bakelite material of the BaBar RPC that has two different surfaces, one side having marble pattern, and another side having uniform brown colour, was taken for the study. The marble pattern was completely ruined after 24 hrs HF vapour deposition whereas after linseed oil coating on the same material there was no deformation seen even with exposure of HF vapour. Surface resistivity was also reduced due to exposure of HF vapour as the study says. So, the study concludes that the HF acid plays a major role in damaging the

inner electrode surfaces, which improves when the surface is coated with linseed oil. This issue has been addressed in detail by Santonico et al. in Ref [11]. Thus linseed oil treatment can effectively protect the electrode plates.

3.5.3 Problem with bakelite electrode

Serious operational problems were observed in the linseed oil coated bakelite RPCs in the BaBar experiment. In this experiment electrode side spacers and button spacers were built in a "mushroom-like" shape for the improvement in HV behaviour. The gaps near the spacers acted as hidden storage cavities and uncured linseed oil was trapped into these cavities. Moreover, it was observed that the conducting paths formed through the gas gap, mainly around the spacers, created due to the formation of stalagmites by the polymerisation of uncured linseed oil droplets. Along with this, due to continued HV operations with the uncured liquid linseed oil inside the active region of the detector, there was some very thin bridges forming inside some regions. These short paths created sparks during the operation, even with nominal operation. Therefore, uncured oil degrades the efficiency as well as performance of the detector and trigger discharges thereby resulting in irreversible damage to the bakelite plates [6, 8, 9, 10, 12, 13, 14].

The charge flow mechanism through the linseed oil layer and bakelite electrodes is due to ions and this linseed oil contains fatty acid which conducts very well. A possible reaction mechanism of linseed oil in presence of high electric field is prescribed by J. Va'vra in the article [6]. The process is described below.

1. R-COOH + potential (HV) $\rightarrow$ H^++R-COO^-;
2. either R-COO^- ion delivers the charge to anode and R-COO returns to fluid or R-COO^- ion transfers a charge to OH^- ion via a reaction R-COO^-+H_2O $\rightarrow$ R-COOH+OH^- ; R-COOH returns the fatty acid back into the cycle and OH^- transfers the charge to anode;
3. H^+ ion delivers the charge to the cathode, where it forms an H_2 molecule and escapes;
4. 2OH $\rightarrow$ H_2O+2O, and 2O $\rightarrow$ O_2, which delivers oxygen near the anode.

Again that water moleculea can conduct through the gas volume and oxygen near the anode surface could react with the graphite layer.

Furthermore, the bakelite plates are made of phenol-formaldehyde polymer, has also ionic origin. Degradation may be caused due to bakelite itself also. For bakelite, the deformation mechanism is also prescribed by J. Va'vra [6], as described below.

1. phenol + potential (HV) $\rightarrow$ H^+ + benzene-O^-;
2. either benzene-O^- ion delivers the charge to anode and benzene-O returns to the fluid, or benzene-O^- ion transfers a charge to OH^- ion via a reaction benzene-O^- + H_2O $\rightarrow$ phenol+OH^-; phenol returns into the cycle and OH^- transfers the charge to the anode;
3. H^+ ion delivers the charge to the cathode, where it forms an H_2 molecule and escapes;
4. 2OH $\rightarrow$ H_2O+2O, and 2O $\rightarrow$ O_2, which delivers oxygen near the anode.

Here also produced oxygen at the anode plate could react with a graphite layer. The bulk resistivity can be changed in presence of water molecules.

3.6 New technique of linseed oil coating

Even with the second RPC module made with bakelite plates having bulk resistivity $\sim 3\times\ 10^{10}\ \Omega$ cm, a high efficiency of ($\sim$ 90%) which is required for any high energy physics experiment is not achieved [16]. Subsequently, it was decided to use the linseed oil coating on the inner surfaces of the electrode plates which is commonly used in bakelite RPC.

A new technique is introduced here to do the linseed oil coating on the bakelite plates before making the gas gap. The prototype is built with indigenous bakelite plates having bulk resistivity $\sim 3\times\ 10^{10}\ \Omega$ cm; this is also the same material used for the second module.

As mentioned earlier, the inner surfaces of the bakelite plates that face the filled gas are usually coated with linseed oil. The linseed oil is a fatty acid (R-COOH), an organic acid that contains the glycerides of linolenic, linoleic, oleic, stearic, and palmitic acids with a high degree of unsaturation of its fatty acid radicals [6]. The linseed oil coating reduces the spurious micro

discharge on the inner surfaces. If the micro discharge probability is reduced, we can have a better performance as compared to the RPC without oil coating [10, 12, 17]. To reduce the after-pulse / noise rate, a low UV sensitive material for the electrode is desirable. As reported earlier, the linseed oil coating reduces the surface UV sensitivity dramatically [10]. Hydrofluoric Acid (HF), produced by the interaction of fluorine with the water vapour, is chemically very reactive. It can affect different materials and has corrosive action. In RPCs fluorine based gas mixtures are commonly used and it is reported that the linseed oil coating on the bakelite surface can effectively protect it from the HF vapour attack [10]. That means the linseed oil treatment on the inner surfaces of the bakelite electrodes is an essential process for the optimum performance (high efficiency and low noise level) of the RPC. For this treatment, usually the RPC gas gap is filled with low viscous linseed oil and thinner solution, and the liquid is drained out slowly. Dry air is flown through the gas gap to cure the thin linseed oil layer left on all the inner surfaces of the plates as well as those of the spacers [8, 9, 13].

However, serious operational problems were observed in the bakelite RPCs in the BaBar experiment. It was observed that the conducting paths through the gas gap, mainly around the spacers, created due to the formation of stalagmites by the polymerisation of uncured linseed oil droplets, trigger discharges thereby resulting in irreversible damage to the bakelite plates [6, 8, 9, 10, 12, 13, 14]. The process of linseed oil treatment was later changed by increasing the ratio of the solvent to produce a thinner coating (10-30 μm) on the surfaces [15]. Efforts were subsequently made to look for alternatives to the linseed oil treatment, or even to develop bakelite sheets having very smooth surfaces, that can be used without the application of linseed oil [13].

One of the main limitations of an RPC is its low particle rate handling capability [18]. Nowadays an RPC detector can handle a maximum particle rate $\sim$ 10 kHz/cm^2 in the avalanche mode of operation [19] but for future experiments, detectors with high particle rate handling capability ($\sim$ 15 kHz/cm^2) are required [20]. One of the ways of increasing the particle rate handling capability in an RPC is the use of low resistive electrode plates of the detector. The other ways are to operate the detector in the avalanche mode and to make RPC modules with thin electrode plates. It is to be mentioned here that the mode of operation depends on the used gas and the applied voltage [21]. For a high rate operation, the preferred option is the avalanche mode.

In the present work, we built a linseed oil coated bakelite RPC. However, in this work, we have adopted a different technique for the linseed oil treatment. Contrary to the conventional procedure, the bakelite plates are coated with linseed oil before making the gas gap to ensure whether the curing is properly done throughout the entire surface. After the linseed oil coating, the plates are cured for 15 days. The advantage of this procedure is that, after the linseed oil coating is done, the surface can be checked visually whether the curing has been properly done or any uncured droplet of linseed oil is present.

3.6.1 Fabrication of the chamber with new technique of linseed oil coating

Two bakelite plates having dimension 27 cm $\times$ 27 cm and thickness 2 mm are used as the electrodes. The bulk resistivity of the plates is $\sim 3 \times 10^{10}$ Ω cm at a temperature of 22°C and a relative humidity of 60%. At first, the bakelite plates are cleaned using isopropyl alcohol. Commercially available linseed oil is used for the inside coating. About 2 g of linseed oil is applied over the 27 cm $\times$ 27 cm area of each plate. Based on the specific gravity (0.930 at 15.5 °C) of the fluid, the estimated coating thickness is ~ 30 μm. The linseed oil is distributed over the surfaces and both the plates are left for 15 days in a sealed box for curing. The two plates are then cleaned again with dry air.

Uniform separation between the electrode plates is ensured by using four edge spacers each of dimension 27 cm $\times$ 1 cm and thickness 2 mm and one button spacer of diameter 1 cm and thickness 2 mm. All the spacers are made of polycarbonate (resistivity $\sim 10^{15}$ Ω cm). For gas inlet and outlet, two nozzles also made of polycarbonate, are used as part of edge spacers. In the gas nozzles cylindrical hole of diameter 1 mm is created in 2 mm thick Polycarbonate. The structure of edge spacers, button spacers and gas nozzles are shown in Figure 3.21. All the spacers are glued on one plate in the oil coated side using Araldite epoxy adhesive. One glued plate is kept for 24 hours for curing and the other plate is glued on it and kept again for curing for 24 hours. After gluing the spacers on the first plate metallic clips are used to fix. After gluing the second plate again metallic clips are used to fix and weight is applied at the middle of the chamber. All the gluing processes are carried out on a laminar flow table. After cleaning, a thin layer of graphite is coated on the outer surfaces of the bakelite plates for

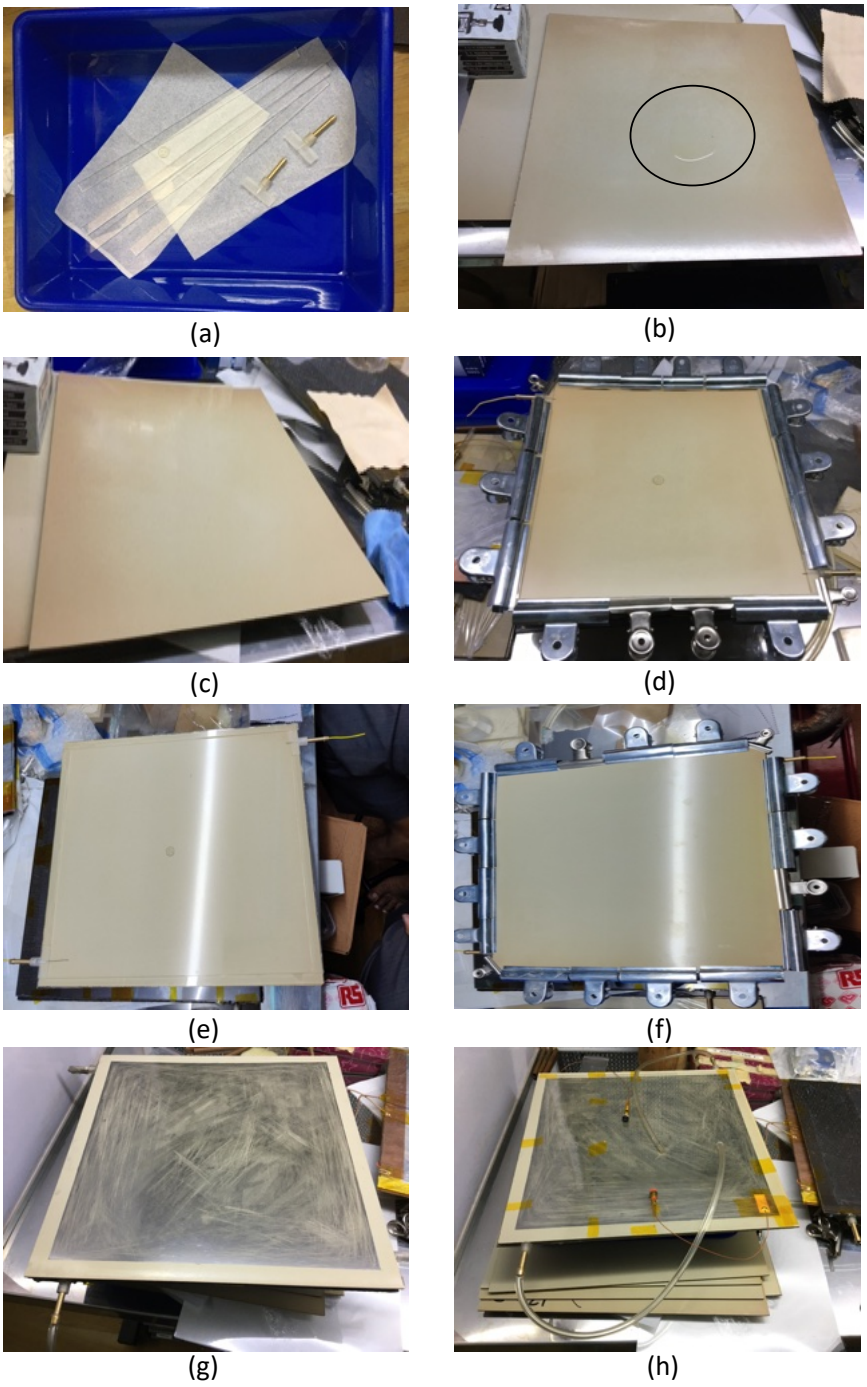

Figure 3.21: Steps of building the linseed oil coated RPC module (a) Components of RPC, (b) Application of linseed oil (marked in the figure), (c) Linseed oil coated bakelite surface, (d) Gluing of spacers and nozzles on one plate, (e) First electrode plate after gluing and curing, (f) Gluing the second plate, (g) Outer surface of the RPC after the graphite coating, (h) Complete RPC with graphite coating, covered with mylar sheet and connecting the HV lead and flexible gas tube.

the distribution of voltage. A gap of 1 cm from the edges of the plates to the graphite layer is maintained to avoid external electrical discharge. The average surface resistivity of the two graphite layers are found to be $\sim$ 510 k$\Omega/\square$ and 540 k$\Omega/\square$ respectively. Two 1 cm $\times$ 1 cm copper tapes of thickness $\sim$ 20 μm each are pasted at two diagonally opposite corners to apply high voltage (HV). The HV cables are soldered on these copper strips. These copper strips are covered with Kapton tapes for isolation. Equal HVs with opposite polarities are applied on two surfaces. The steps of building of the module are shown in Figure 3.21.

The pick-up strips are placed above the graphite layers in order to collect the accumulated induced charge. 2.5 cm wide and 100 μm thick copper tapes (each fabricated having a 2 mm separation among two consecutive strips) are pasted on one side of a 2 mm thick G-10 board and the ground plane is made with aluminium foils of thickness 10 μm each on the other side of the G-10 board to make the pick-up panel. The strips are covered with 100 μm thick mylar foils to isolate them from the graphite layers. The signals from the strips are collected through RG-174/U coaxial cables.

3.6.1.1 Cosmic ray test set-up

Three plastic scintillation detectors, two placed above the RPC module and one placed below, are used to obtain the trigger from the incoming cosmic rays. The coincidence signal obtained from the topmost paddle scintillator (SC1) having dimension 10 cm $\times$ 10 cm, a finger scintillator (SC2) of dimension 10 cm $\times$ 2 cm and the paddle scintillator (SC3) having dimension 20 cm $\times$ 20 cm are taken as the trigger (3-fold). The RPC is placed in between the finger (SC2) and the paddle scintillator (SC3). All the scintillators are operated at +1550 V and a -15 mV threshold is applied to the leading edge discriminator (LED).

The RPC signal from the pick-up strip is first fed to the 10x fast amplifier and the output of it then goes to the LED. Different thresholds are applied to the LEDs to reduce the noise. From the LED, one output goes to the scaler to count the number of signals from the RPC which is known as the noise count or singles count of the chamber. The other output from LED goes to the dual timer where the discriminated RPC signal is stretched to avoid any double counting of the pulses and also to apply the proper delay to match the signal with the trigger. The output of the dual timer is put in coincidence with the trigger and this is defined as the 4-fold. The

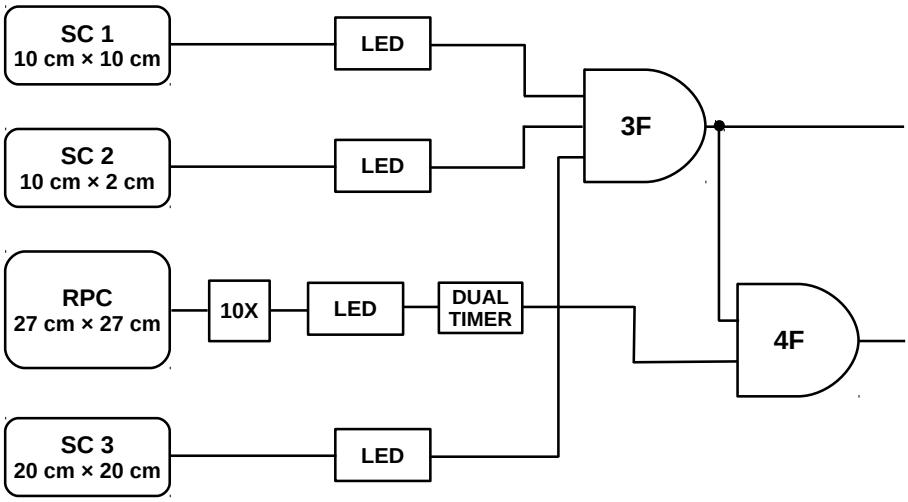

Figure 3.22: Schematic of the electronics set-up of the cosmic ray test

window of the cosmic ray test set-up is of area 10 cm × 2 cm. The detailed block diagram of the electronics set-up is shown in Figure 3.22.

To characterise the chamber initially 100% $C_2H_2F_4$ gas is used as the active medium. A typical gas flow rate of 2 ml/min, equivalent to 6 gap volume changes per day, is maintained by using two needle valves. However, later on, a $C_2H_2F_4$ and i-C_4H_{10} mixture in the 90/10 volume ratio is also used to test the detector.

3.7 Results of new RPC

The prototype is tested with cosmic ray using 100% $C_2H_2F_4$ gas and $C_2H_2F_4$, Iso-butane (i-C_4H_{10}) mixture in 90/10 volume ratio with conventional NIM electronics [22].

After building the chamber, 100% $C_2H_2F_4$ gas is purged for 24 hours before the application of HV. The HVs of equal value and opposite polarities, to the RPC module are applied at a ramp-up rate of 2 V/s on both sides. The leakage currents from both sides, as measured by the HV module are also recorded. The temperature and the relative humidity are also recorded at the time of measurement using a data logger, built-in house [23]. To check the performance of the detector, firstly the leakage current through the RPC module is measured as a function of the applied HV and shown in Figure 3.23. A breakdown of the gas, although not sharp, is

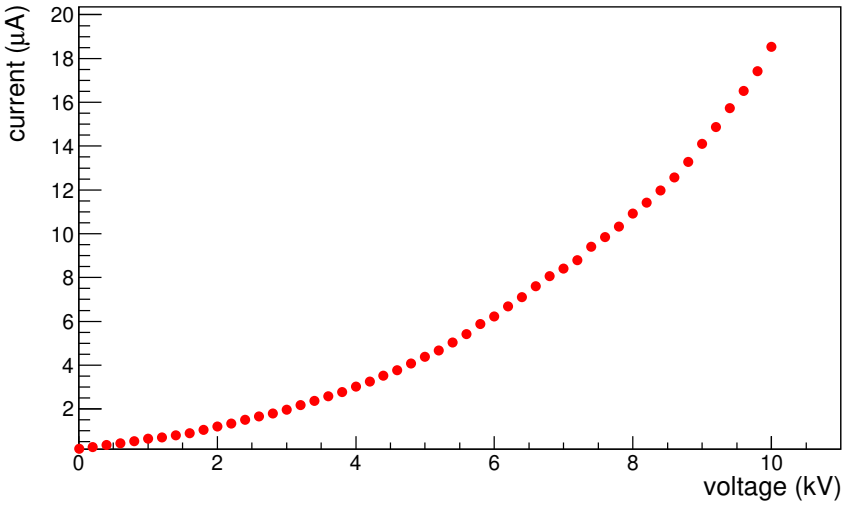

Figure 3.23: Leakage current as a function of the applied voltage for the RPC module with 100% $C_2H_2F_4$ gas. The error bars are smaller than the size of the markers

seen at about $\sim$ 8 kV. The gas gap behaves as an insulator in the low applied voltage range and hence the slope over this voltage region scales as the conductance of the polycarbonate spacers. At a higher value of the applied voltage, the gas behaves as a conducting medium due to the ionisation. Therefore, the slope over this range scales as the conductance of the bakelite plates. The curve of leakage current vs. voltage as found here is not only very similar to the curve for linseed oil coated bakelite RPC, as reported earlier [8], but the magnitude of current is also comparable.

As mentioned earlier, for the test using cosmic rays, the efficiency of the RPC is defined as the ratio of the 4-fold counts to the 3-fold trigger count of the plastic scintillator telescope for a fixed duration. The noise rate (or singles count rate) of the RPC is defined as the number of counts per unit area of the strip per second. The efficiency and the noise rate are studied by varying the applied HV. Both the efficiency and noise rate are measured for two different discriminator threshold settings, - 15 mV and - 20 mV respectively for the RPC. The temperature and relative humidity during these measurements are recorded and the average temperatures are found to be about 25 °C and 27 °C, respectively and the average relative humidity is found to be 44% in both the cases. The efficiency and the noise rate as a function of voltage are shown in Figure 3.24. For a - 15 mV threshold setting, the efficiency increases with applied voltage and reaches a plateau at $\sim$ 95% from 9.4 kV onwards, whereas for a - 20 mV threshold setting

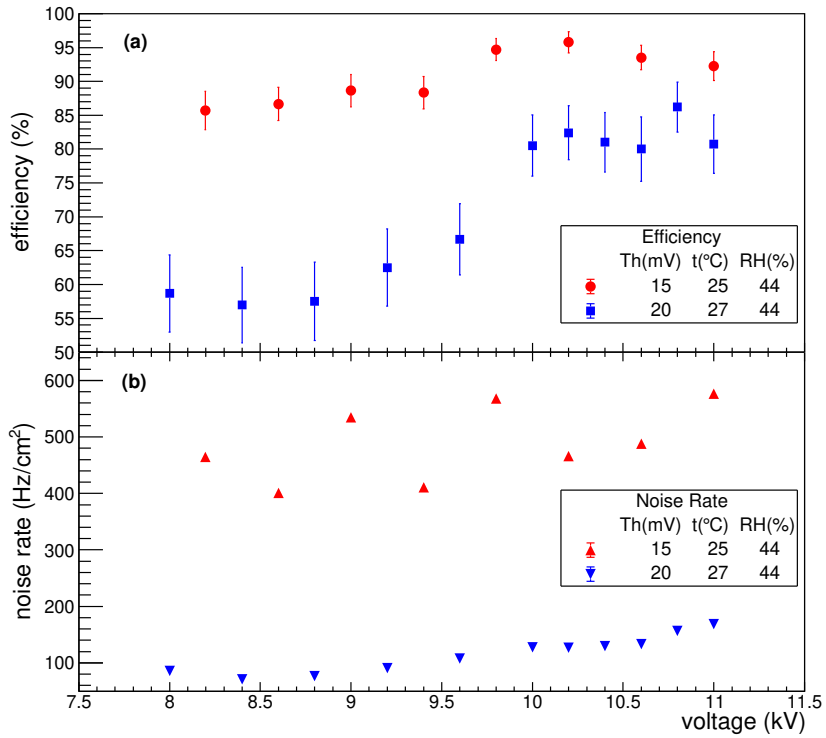

Figure 3.24: (a) Efficiency as a function of the applied voltage for the RPC, (b) Noise rate as a function of the applied voltage with 100% $C_2H_2F_4$ gas

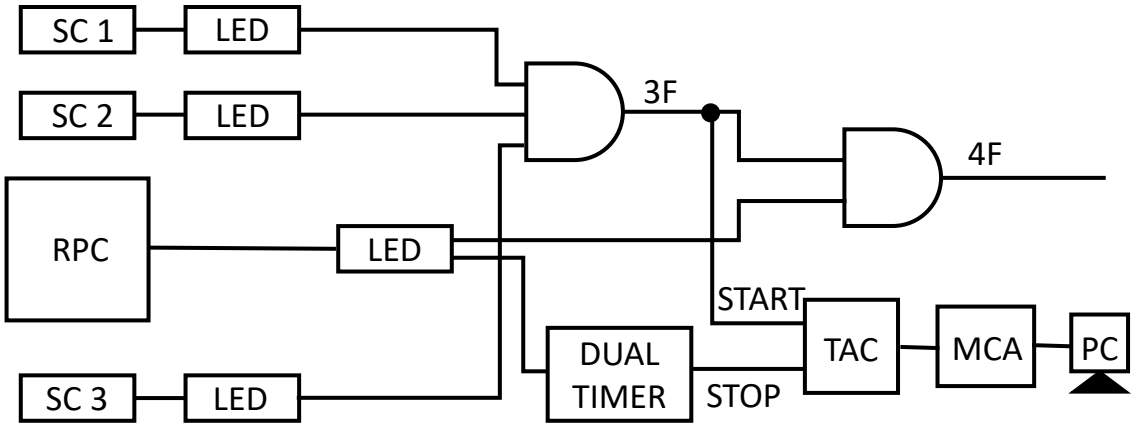

Figure 3.25: Schematic representation of the time resolution measurement set-up with cosmic rays. SC 1, SC 2 and SC 3 are the plastic scintillators of dimensions 10 cm × 10 cm, 2 cm × 10 cm and 20 cm × 20 cm. respectively. LED, TAC, MCA and PC are the Leading edge discriminators, Time to Amplitude Converter, Multi-Channel Analyser and Personal Computer respectively.

the efficiency saturates at $\sim$ 85% from the applied voltage of 10.1 kV onwards. The noise rate increases with the applied HV. The noise rate is measured to be much higher for the lower threshold with a maximum value of $\sim$ 500 Hz/cm^2. For a - 20 mV threshold, the maximum noise rate is found to be $\sim$ 200 Hz/cm^2.

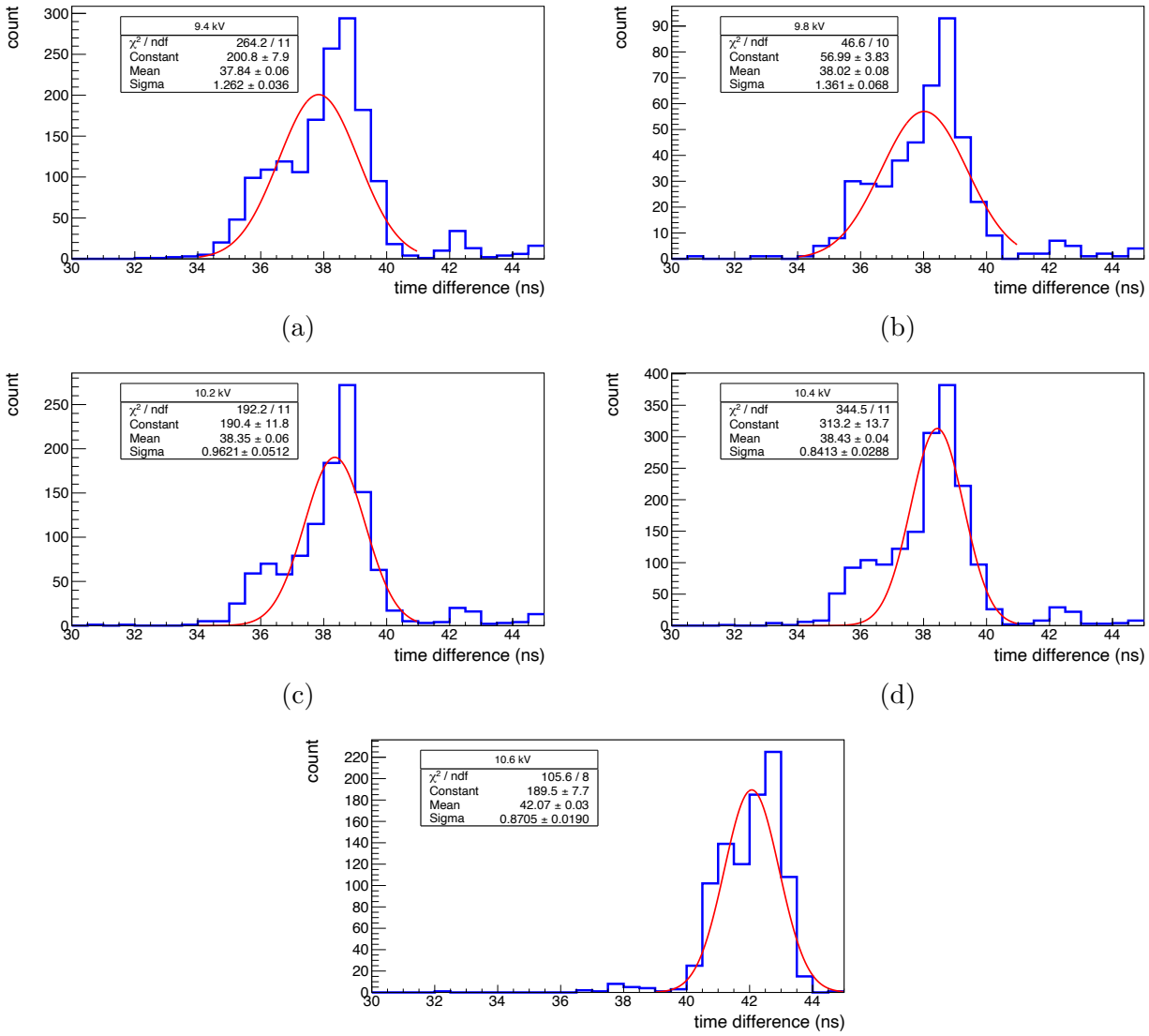

Figure 3.26: Time spectra of the linseed oil coated RPC at different voltage differences across the gas gap for 100% $C_2H_2F_4$: (a) 9.4 kV (b) 9.8 kV (c) 10.2 kV (d) 10.4 kV (e) 10.6 kV voltage differences across the gas gap

The time resolution of this RPC prototype is also measured. While measuring the time resolution in this case also, the RPC signal is stretched to 500 ns to avoid the effect of double

pulses or reflection pulses if there are any. The full scale of the TAC is set to 100 ns. The full electronics setup block diagram for time resolution measurement is shown in Figure 3.25 and typical time spectra for the RPC at different voltages are shown in Figure 3.26 with 100% $C_2H_2F_4$ gas. In this case the START signal of the TAC is taken from the 3-fold scintillator trigger and the STOP signal is taken from the RPC. The distribution of the time difference between the master trigger and the RPC signal is fitted with the Gaussian function. By finding the σ of the distribution and subtracting in quadrature the contribution from the scintillator as explained in section 3.4.2, the intrinsic time resolution of the RPC is calculated. For this measurement no amplifier is used for the RPC.

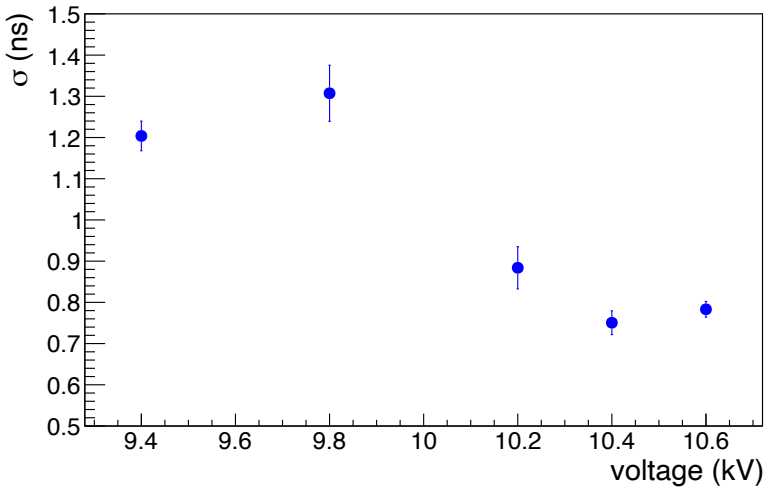

Figure 3.27: Time resolution (σ) of the linseed oil coated bakelite RPC as a function of voltage for 100% $C_2H_2F_4$.

The intrinsic time resolution (σ) of the RPC as a function of the applied voltage is shown in Figure 3.27 for 100% $C_2H_2F_4$. For this prototype also, with the increase of applied voltage, the time resolution (σ) improves.

The detector is further tested in the avalanche mode with a more conventional gas mixture of Tetrafluoroethane ($C_2H_2F_4$) and Iso-butane (i-C_4H_{10}) in the 90/10 volume ratio. Iso-butane has a high UV absorption coefficient and it prevents the formation of secondary discharges due to photoelectrons. The performance of the chamber is even found to be better with the application of the additional quencher. Both the current and noise rate are very low for this gas mixture, as compared to that with the 100% $C_2H_2F_4$ used for the same detector. The leakage

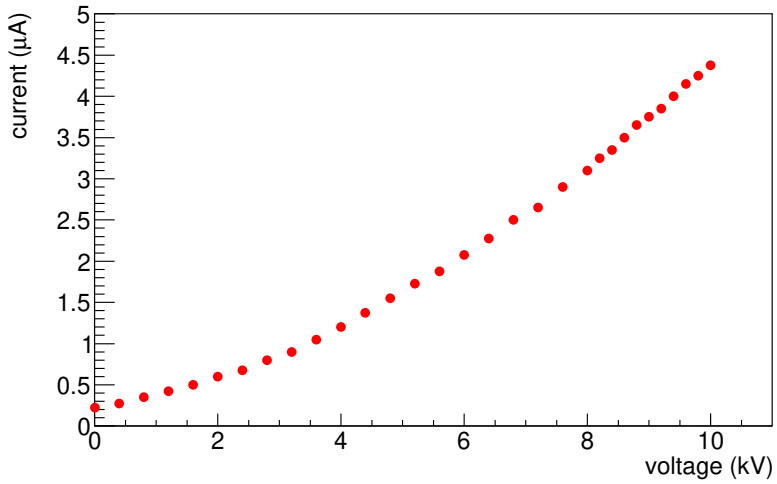

Figure 3.28: Leakage current as a function of the applied voltage with $C_2H_2F_4$ and i-C_4H_{10} gas mixture in 90/10 volume ratio.

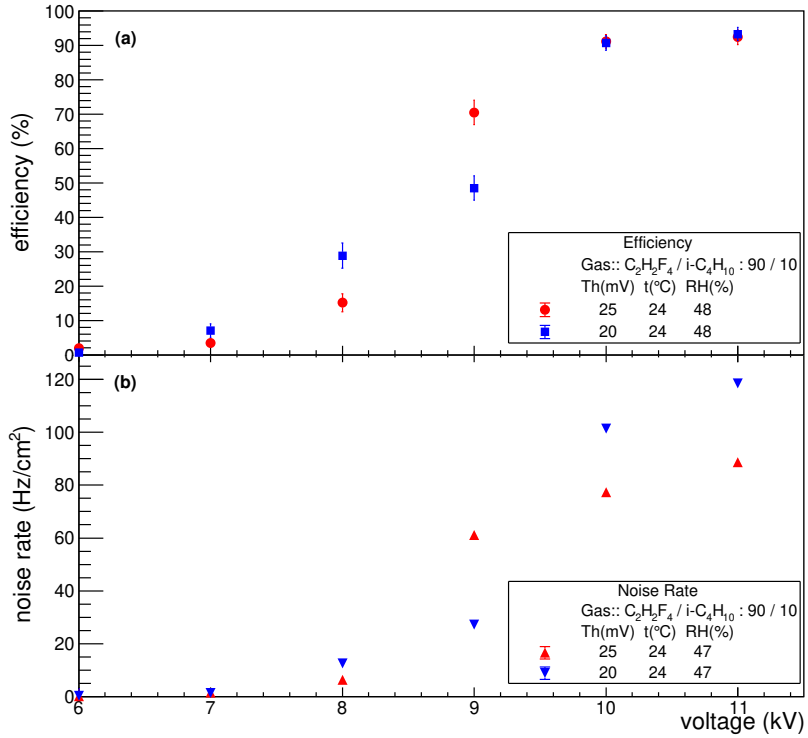

Figure 3.29: (a) Efficiency as a function of the applied voltage, (b) Noise rate as a function of the applied voltage for a gas mixture of $C_2H_2F_4$ and i-C_4H_{10} in the 90/10 volume ratio

current through the RPC module is measured as a function of the applied voltage and is shown in Figure 3.28. The current is found to be much lower compared to that with 100% $C_2H_2F_4$.

The efficiency and noise rate are studied by varying the applied HV. With this gas mixture, the RPC is tested with - 20 mV and - 25 mV threshold settings. The variation of efficiency and noise rate shown in Figure 3.29. An efficiency of $\sim$ 95 $\pm$ 2% is achieved from 10 kV onwards for both the threshold settings. The maximum noise rates are found to be 120 Hz/cm^2 and 80 Hz/cm^2 for the - 20 mV and - 25 mV thresholds respectively, as shown in Figure 3.29.

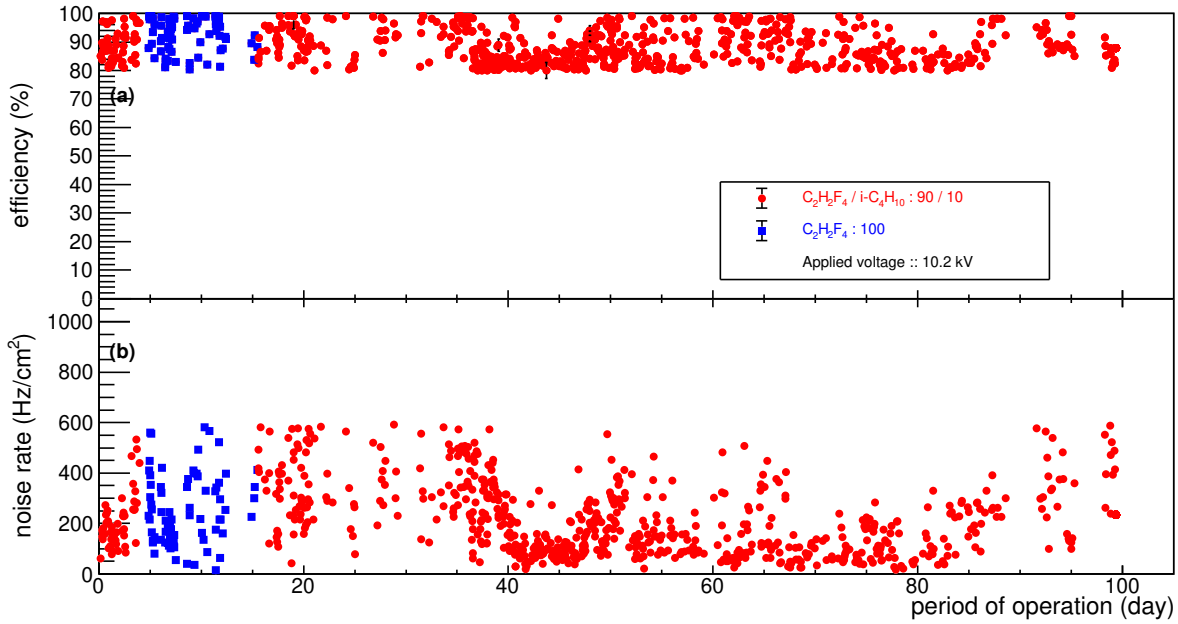

Figure 3.30: (a) Efficiency and (b) noise rate of the detector as a function of period of operation for two different gas composition. For some data points the error bars are smaller than the size of the markers.

The stability test is performed both with a $C_2H_2F_4$ and i-C_4H_{10} mixture in the 90/10 volume ratio and with 100% $C_2H_2F_4$. Initially, the detector is operated with a mixture of $C_2H_2F_4$ and i-C_4H_{10} and then it is continuously tested with 100% $C_2H_2F_4$ for next few days. After that it is again tested with the mixed gas. The measured efficiency and noise rate of the detector as a function of the period of operation for two different gas compositions for more than three months are shown in Figure 3.30. The distribution of efficiency and noise rate for two gas compositions are shown in Figure 3.31 and 3.32 respectively. It is found that for $C_2H_2F_4$ and i-C_4H_{10} mixture and 100% $C_2H_2F_4$ the average efficiencies are found to be 88 $\pm$ 6 % and 93 $\pm$ 6 % respectively whereas the average noise rates for two compositions are found to be 189 $\pm$ 131 Hz/cm^2 and 208 $\pm$ 129 Hz/cm^2. There are some gaps in the plot *e.g.* days 12-13 when HV was on but the data was not taken.

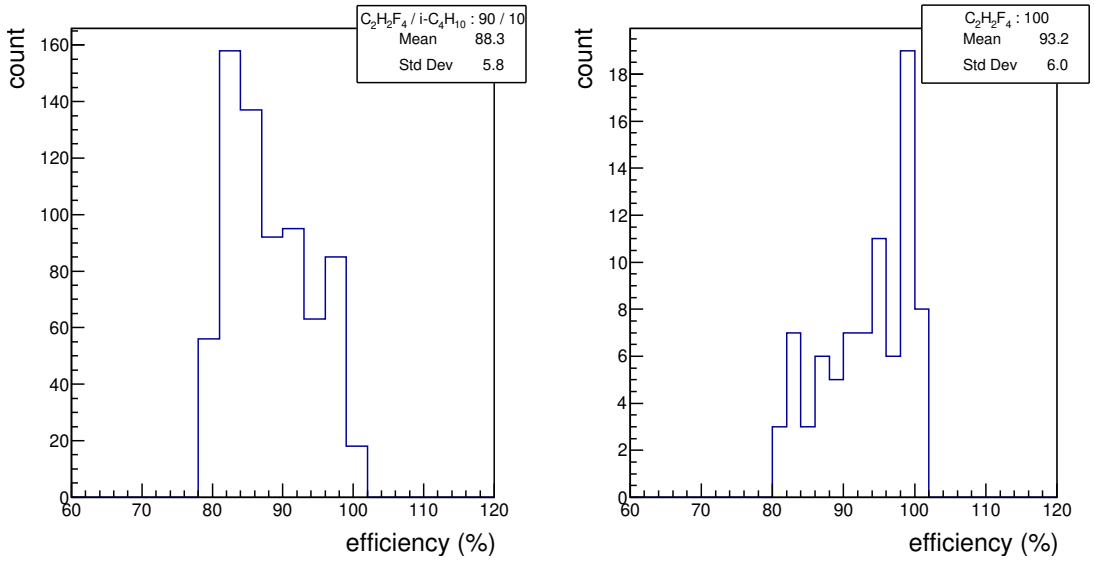

Figure 3.31: Distribution of the efficiency values of long-term measurements

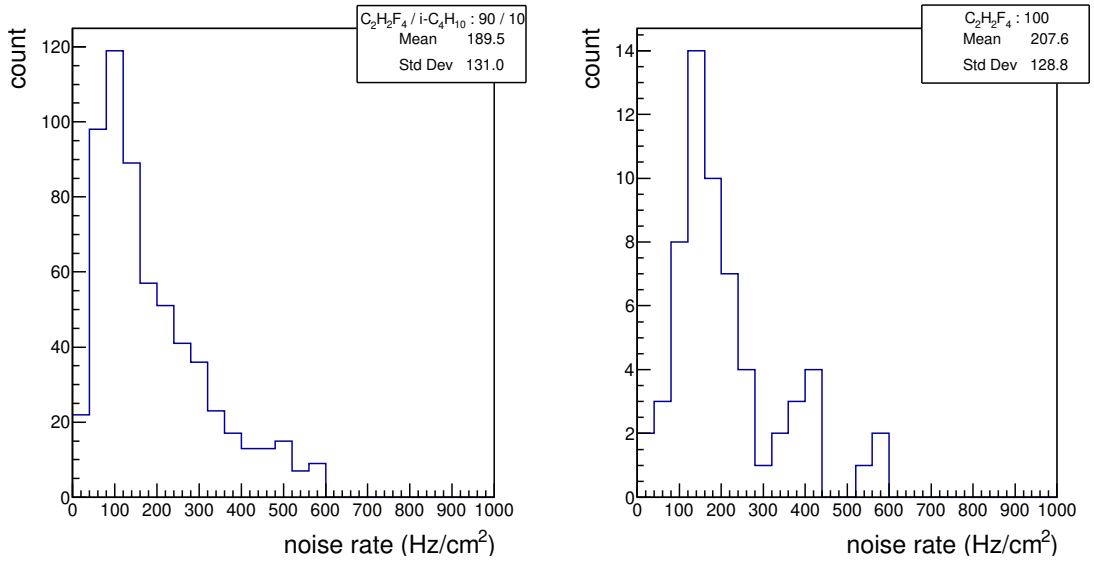

Figure 3.32: Distribution of the noise rates values of long-term measurements

For the oil-less RPC prototype, the efficiency is found to be $\sim 70\%$ and noise rate ~ 200 Hz/cm^2 (at around 10 kV; for day 2 in Figure 3.16) at -15 mV threshold with 100% $C_2H_2F_4$ gas. For the linseed oil coated prototype the efficiency improved to $> 85\%$ and $> 90\%$ with 100% $C_2H_2F_4$ gas and 90/10 :: $C_2H_2F_4$ / i-C_4H_{10} mixture respectively at threshold settings of -20 mV (at around 10 kV; Figure 3.24 and Figure 3.29). The nose rates are found to be ~ 400 Hz/cm^2 and

$\sim$ 100 Hz/cm^2 for the respective gas mixtures. So, with this new linseed oil coating efficiency improves but the noise rate is higher for 100% $C_2H_2F_4$ gas but the noise rate is lower when quencher is added. Though with oil coating and the mixed gas noise rate improves, still a detailed investigation is needed in future to understand the behaviour properly.

3.7.1 Measurement of charge sharing

Charge sharing is measured between the two consecutive readout strips varying the applied voltage with the $C_2H_2F_4$ and i-C_4H_{10} gas mixture in the 90/10 volume ratio. The charge sharing is defined as the ratio of the coincidence count of two consecutive readout strips taken in coincidence with the 3F scintillator trigger (5F) to the trigger count (3F). Actually for this measurement the finger scintillator of the trigger is placed just above one single strip (as explained in Sec. 3.4.1 and 3.6.1.1) from which the efficiency also measured for reference.

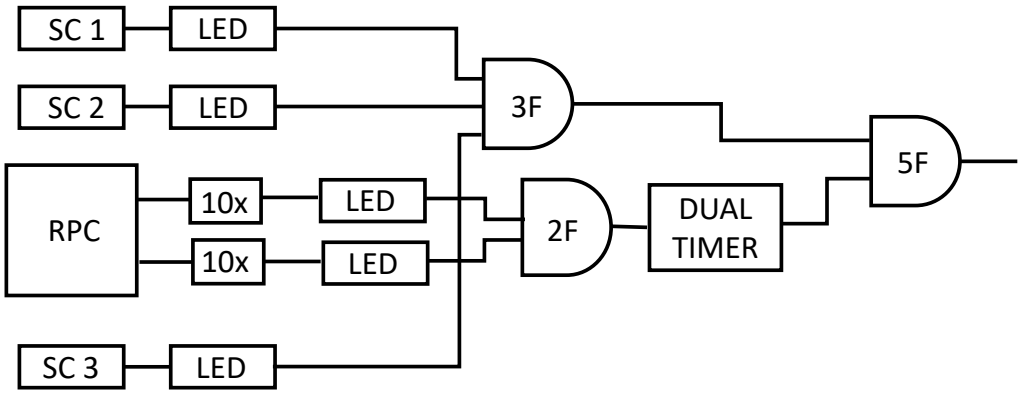

Figure 3.33: Circuit diagram for charge sharing measurement. The symbols have their usual meaning.

In Figure 3.33 the block diagram of the electronic circuit of charge sharing measurement is shown. For the measurement of charge sharing, signals from two consecutive pick-up strips are taken in coincidence. The discriminated signals from two consecutive strips are first fed to the coincidence module and the logic output is put to the dual timer for the delay matching. Dual timer output is then taken in coincidence with the trigger generated by the 3-Fold scintillator array.

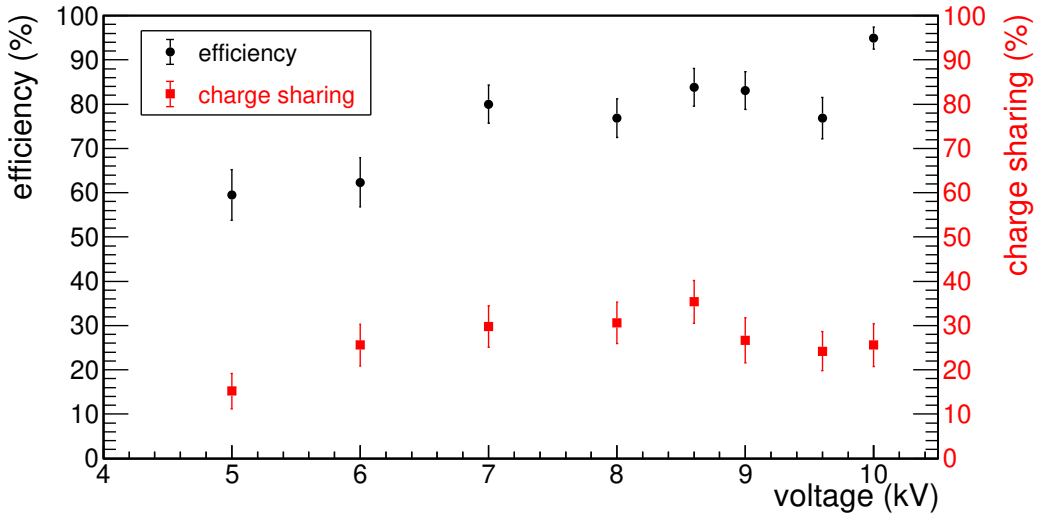

Figure 3.34: Variation of efficiency and shared charge between two consecutive strips with the voltage

Charge sharing between two consecutive strips as a function of applied voltage in shown in Figure 3.34. In the same plot the efficiency as a function of voltage measured on the same day is also shown for reference. One can see in Figure 3.34 that the shared charge is about $\sim 30\%$, when the efficiency measured from a single strip is $\sim 90\%$. With the increasing voltage the shared charge initially increased from 5 to 8 kV and then remains constant within the error bars. Although we have referred this measurement as charge sharing but the crosstalk between the strips are not eliminated for this particular measurement.

3.7.2 Radiation hardness test

Finally the prototype is tested in the high intensity gamma ray environment background. A ^{137}Cs source of activity $\sim$ 13.6 GBq is used for the this measurement. 662 keV photons incident on the detector from the source with an intensity of $\sim$ 46 kHz/cm^2. As shown in Figure 3.35(a) the source is placed on the top of the top scintillator paddle. The efficiency is measured for three voltage settings 9.0, 10.2 and 10.4 kV, respectively with and without the gamma source. The measurement is performed with the $C_2H_2F_4$ and i-C_4H_{10} gas mixture in the 90/10 volume ratio. The obtained efficiency value is shown in absence and presence of the gamma source in

Figure 3.35(b). It is observed that the efficiency decreased by only 1 % with a gamma ray flux of 46 kHz/cm^2 from the efficiency value without the source.

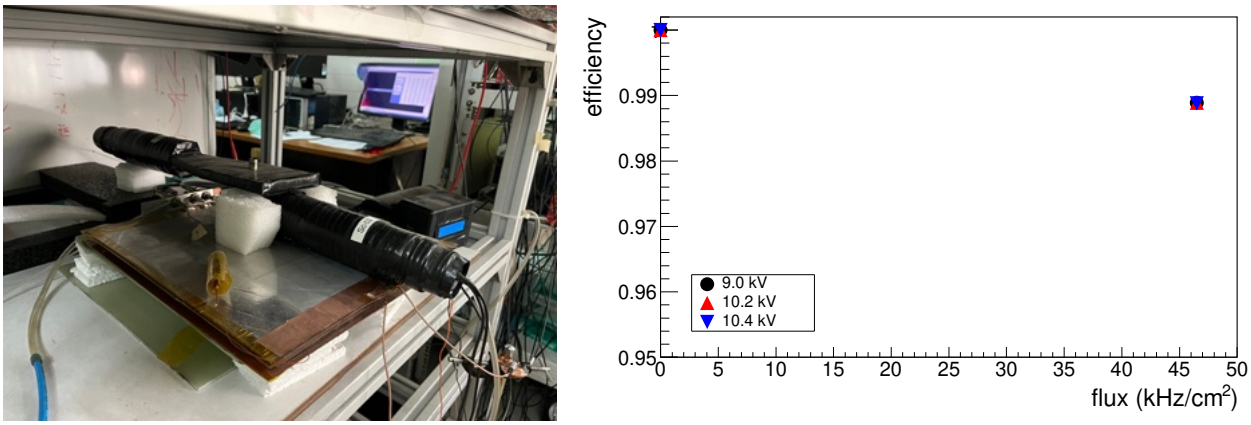

(a) (b)

Figure 3.35: (a) The experimental setup of characterisation in presence of gamma source, (b) Efficiency as a function of gamma ray flux. Error bars are smaller than the marker size

Bibliography

[1] Manisha *et al.*, Study of Glass and Bakelite properties as electrodes in RPCs, arXiv:1604.04130.

[2] B. Liberti *et al.*, *ATLAS RPC perfomance on a dedicated cosmic ray test-stand*, *Nuclear Physics B (Proc. Suppl.)* 177 (2008) 307.

[3] A. Bergnoli *et al.*, *Tests on OPERA RPCs*, *Nuclear Physics B (Proc. Suppl.)* 158 (2006) 93.

[4] A. Bergnoli *et al.*, *Tests on OPERA RPC Detectors*, *IEEE TRANSACTIONS ON NUCLEAR SCIENCE* VOL. 52, NO. 6, DECEMBER 2005.

[5] F. Bossu *et al.*, *Performance of the RPC-based ALICE muon trigger system at the LHC*, *JINST* 7 (2012) T12002.

[6] J. Va'vra, Nucl. Inst. and Meth. A 515 (2003) 354.

[7] `https://en.wikipedia.org/wiki/Linseed_oil`

[8] M. Abbrescia *et al.*, Nucl. Inst. and Meth. A 394 (1997) 13.

[9] B. Hong *et al.*, Journal of the Korean Physical Society, Vol. 48, No. 4, April 2006, 515.

[10] C. Lu, Nucl. Inst. and Meth. A 602 (2009) 761.

[11] R. Santonico, Nucl. Inst. and Meth. A 533 (2004) 1.

[12] S. Biswas *et al.*, Nucl. Inst. and Meth. A 604 (2009) 310.

[13] J. Zhang *et al.*, Nucl. Inst. and Meth. A 540 (2005) 102.

[14] F. Anulli *et al.*, Nucl. Inst. Methods. A 508 (2003) 128.

[15] F. Anulli *et al.*, Nucl. Inst. Methods. A 539 (2005) 155.

[16] CMS Physics, CMS TDR 8.1. ISBN: 92-9083-268-1, 978-92-9083-268-3

[17] R. Santonico and R. Cardarelli, Nucl. Inst. and Meth. A 187 (1981) 377.

[18] Y. Haddad *et al.*, Nucl. Inst. and Meth. A 718 (2013) 424.

[19] L. Pizzimento *et al.*, JINST 15 (2020) C11010.

[20] E. Nandy *et al.*, Proc. of the DAE-BRNS Symp. on Nucl. Phys. 61 (2016) 1024.

[21] K. K. Meghna *et al.*, Nucl. Inst. and Meth. A 816 (2016) 1.

[22] A. Sen *et al.*, Nucl. Inst. Methods. A 1024 (2022) 166095.

[23] S. Sahu *et al.*, 2017 JINST 12 C05006.

Chapter 4

Application of radiation detector

The plastic scintillation detectors which are used as the trigger detector for the RPC characterisation, are used to measure the cosmic ray muon flux at Kolkata and to see whether there is any correlation of muon flux with air pollutants after the lockdown to restrict COVID-19 was lifted. The cosmic ray muon flux is measured using the coincidence technique with plastic scintillation detectors before and after the lockdown. Due to the COVID-19 outbreak and nationwide complete lockdown, the laboratory was closed from the end of March 2020 till the end of May 2020. After lockdown, although the city was not in its normal state, we still were able to take data on some days. The lockdown imposed a strict restriction on the transport service other than the emergency ones and also most of the industries were shut down in and around the city. This lockdown has significant effect on the atmospheric conditions in terms of change in the concentration of air pollutants. The cosmic ray flux have been measured before and after the lockdown to observe the apparent change if any due to change in the atmospheric conditions. The whole measurement has been carried out at High Energy Physics Detector Laboratory at Bose Institute, Kolkata (22.58° N 88.42° E and 11 m above the Sea Level) along with the major air pollutants present in the atmosphere before and after the lockdown.

Cosmic ray consists of high energy particles that mostly originate from outer space, with some very high energy particles even thought to have an extragalactic origin. Primary cosmic rays consist of 90% protons, 9% alpha particles and of other heavier nuclei [1]. These primary cosmic rays interact with the gas molecules in the atmosphere and produce secondary cosmic rays. These secondary particles consist mostly of pions and some kaons. Neutral pions (π^0)

decay into gamma rays that generate electromagnetic showers (e^+, e^-, γ), which posses low penetration power. Charged pions (π^+, π^-) decay into muons and neutrinos. Neutrinos have a very small cross-section for interaction and typically pass through the earth without any further interactions. On the other hand, muons are heavy particles and thus loss of energy through bremsstrahlung is negligible for them. This makes the muon a very penetrating particle, unlike electron. The muon has a lifetime of 2.2 μs yet it still makes it down to detectors at the surface of the earth traversing through the atmosphere. This is because the muon travels at a speed that is close to that of light and thus experiences relativistic time dilation and therefore can be detected by our detectors. Since the secondary cosmic rays are mostly muons and they can travel large distance through the atmosphere before they are detected, it will be really interesting if any correlation of this cosmic ray muon flux with the change in atmosphere in terms of the concentration of air pollutants is found [2, 3, 4].

For this study, cosmic ray flux has been measured in our laboratory using plastic scintillation detectors before and after the imposition of lockdown due to the COVID-19 pandemic. The effects of atmospheric pressure and temperature on the muon flux has also been studied here. A brief description of the change of atmospheric parameters due to lockdown is discussed in the next section. The succeeding sections consist the details of the experimental setup, results followed by summary and discussions.

4.1 Effect due to lockdown

Along with many other countries in the world India was also at a critical stage in its fight against COVID-19 with large number of positive case and death [5]. The entire country was under complete lockdown from March 25 to April 14, 2020, for 21 days, which was further extended by the Government of India until May 3, 2020, followed by the third phase of lockdown till May 17, 2020, and the fourth phase till May 31, 2020, to tackle the spread of COVID-19. Restrictions on social gathering and travelling resulted in the shutdown of all the businesses which include industries, transport (air, water, and surface), markets, shops, tourism, construction and demolition, hotels and restaurants, mining and quarrying, etc. except the essential services like groceries, milk, medicines and emergency services like hospital, fire service and administration. In June 2020 Governments, both state and central, declared restricted unlocking

phase. While Unlock phases were started from 1^{st} June 2020, there were complete lockdown in West Bengal on some selected dates to combat against CO-VID19. The dates of lockdown are mentioned in Figure 4.1.

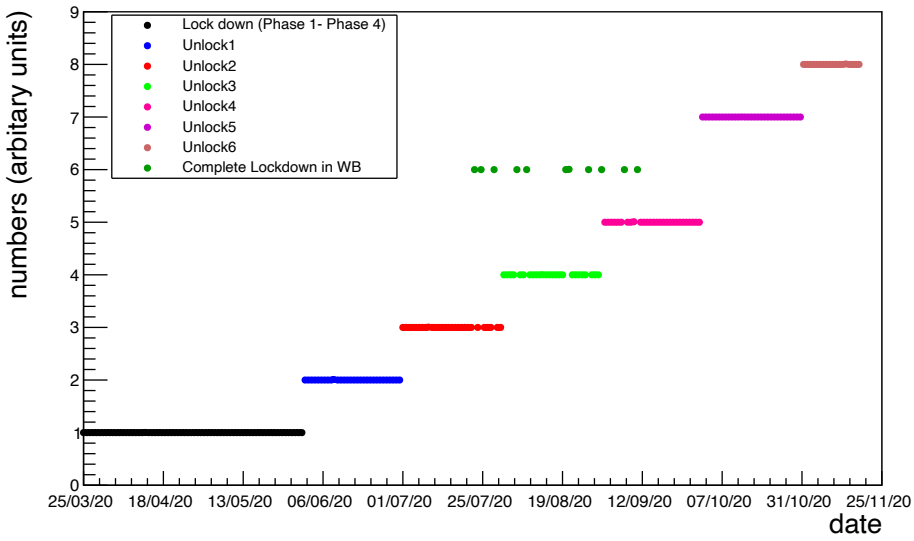

Figure 4.1: Different phases of lockdown and unlock as a function of date. The complete lockdown is marked with 1, different unlock phases are marked as 2, 3 so on and the complete lockdown days in West Bengal during the unlock phases are marked with 6.

The complete lockdown is marked with 1, different unlock phases are marked as 2, 3 so on and the complete lockdown days in West Bengal during the unlock phases are marked with 6. During the lockdown (25^{th} March to 6^{th} April 2020; Lockdown Phase-1) and before lockdown (10^{th} - 20^{th} March 2020), significant variation in the concentrations of the five most abundant pollutants in the air ($PM_{2.5}$, PM_{10}, NO_2, CO, O_3) are observed in Kolkata. The concentrations of air pollutants in Kolkata are decreased by ∼23% ($PM_{2.5}$), ∼34% (PM_{10}), ∼60% (NO_2), ∼29% (CO) while the O_3 concentration is increased by ∼17% due to the clearer atmosphere as compared to that before lockdown period [2]. We also looked into the last year data for the same period (March-April, 2019) and found that, during the lockdown, the concentration of air pollutants are decreased by ∼27% ($PM_{2.5}$), ∼32% (PM_{10}), ∼66% (NO_2), ∼16% (CO) and O_3 concentration is increased by ∼87% [2].

We have used the live day to day data from Ref [6] of the concentrations of the seven major air pollutants and studied the effects of them on cosmic ray flux. In our work, we have reported the

measured muon fluxes before and after the lockdown at Kolkata and tried to correlate the same with the change in the concentrations not only of the individual components of air pollutants but also the total amount of pollutants.

4.2 Experimental set-up

The schematic of the muon flux measurement set-up is shown in Figure 4.2. Data are taken in Kolkata before (December 27, 2019 to February 18, 2020 during RPC testing) and after (June 24, 2020 to November 17, 2020) the lockdown due to the COVID-19 pandemic. For initial analysis, these data are initially considered. Three plastic scintillators tagged as SC1, SC2, and SC3, made of BC400 material are used in this setup [7, 8]. The dimensions of these scintillators are 10 $\times$ 10 cm^2, 2 $\times$ 10 cm^2 and 20 $\times$ 20 cm^2 respectively. The coincidence area of three detectors is 20 cm^2. The distance between the top and bottom scintillator is $\sim$ 10 cm whereas that between the top and the middle one is 4 cm. Each scintillator is connected with a Photo Multiplier Tube (PMT) and a base where one SHV (Safe High Voltage) and one BNC (Bayonet Neill-Concelman) connectors are provided for the application of High Voltage (HV) and collection of signals respectively. +1550 V are applied to all the PMTs. Thresholds to the leading edge discriminators (LEDs) are set to -15 mV for all the scintillators. The width of each discriminator output is kept at 50 ns. The coincidence of these three signals is achieved

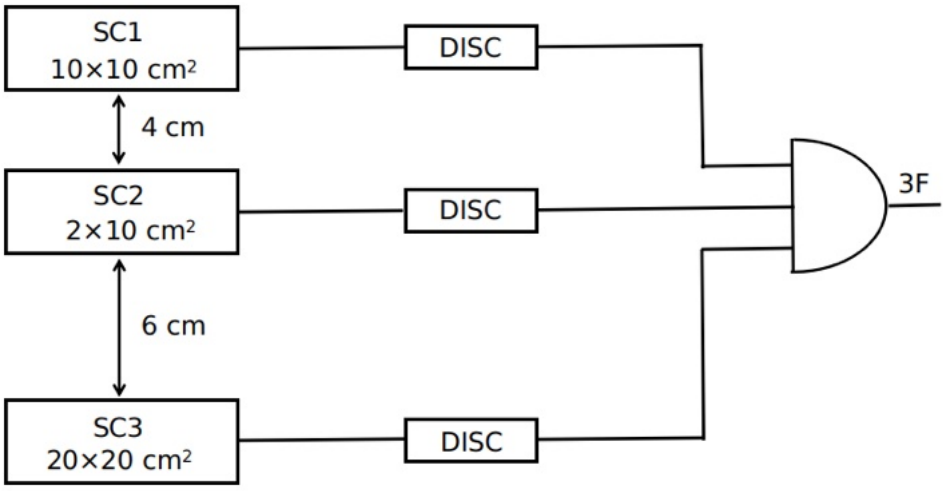

Figure 4.2: Schematic of the experimental set-up for muon flux measurement

using a logic unit. The three-fold coincidence signal is then counted using a scaler and then divided by the product of the area of coincidence window (20 cm^2), muon detection efficiency of the system ($\sim$ 72%) [8] and the measurement time to get the muon flux. The calculated muon flux is then multiplied by a factor of 0.95 to correct the effect of the difference in the threshold settings to the discriminator for the scintillators, during the efficiency measurement [8] (threshold is -30 mV) and the present measurement (threshold is -15 mV). Each data point represents a 30 minutes long measurement. To check the health of the individual detectors, the singles count rate of all the modules is measured several times. It is found that the singles count rate of scintillators SC1, SC2, and SC3 are found to be $\sim$ 77, $\sim$ 28, and $\sim$ 171 Hz respectively.

4.3 Results

The cosmic ray flux is measured in Kolkata before and after the lockdown due to the COVID-19 outbreak. The average muon flux before and after the lockdown is shown in Figure 4.3 as a function of time. We had a very small amount of data before the lockdown. The cosmic ray flux has a dependence on atmospheric parameters like temperature and pressure [9, 10]. In this

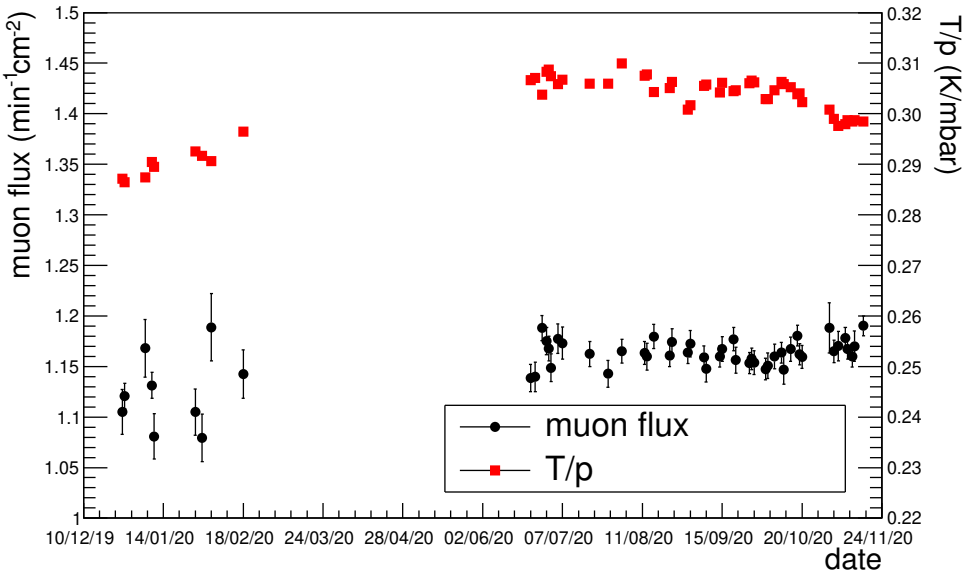

Figure 4.3: Cosmic ray muon flux and T/p as a function of date

work, the temperature and pressure data are collected from Ref [11]. The ratio of temperature and pressure as a function of the day is also shown in Figure 4.3.

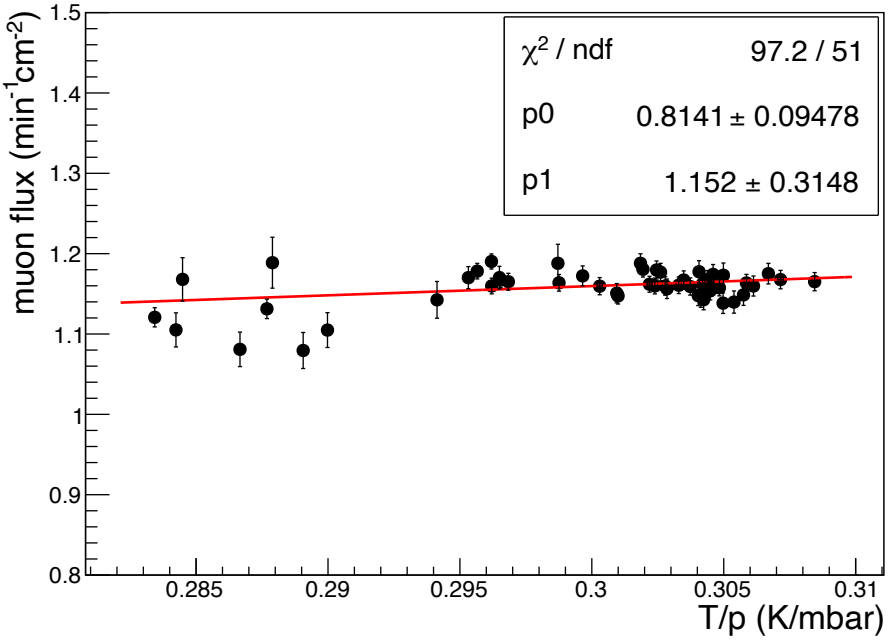

Figure 4.4: Correlation of cosmic muon flux with the ratio of temperature and pressure

In order to normalise the temperature ($T = t + 273$) and pressure (p) effects, a simple correlation between cosmic muon flux and T/p is studied using the relation $p0 + p1(T/p)$. The correlation of muon flux and T/p is shown in Figure 4.4. The parameters obtained from the correlation are 0.81 ± 0.10 min^{-1}cm^{-2} (p0) and 1.15 ± 0.32 min^{-1}cm^{-2}k^{-1} mbar (p1) respectively.

A positive correlation is observed between the muon flux and T/p. Using the parameters, the muon flux measured before and after the lockdown is normalised and shown in Figure 4.5.

In Figure 4.6, the distribution of the normalised muon flux is shown before and after the lockdown. It is found that the mean normalised muon flux before the lockdown period is 0.982 with a standard deviation of 0.031, whereas that after lockdown is 1.001 with a standard deviation of 0.012 *i.e.* 1.9 % increment in muon flux is found after lockdown.

In Figure 4.7, we have reported the individual air pollutants concentration before and after the lockdown (on the dates of cosmic ray data recording) and a clear decrement in the concentrations

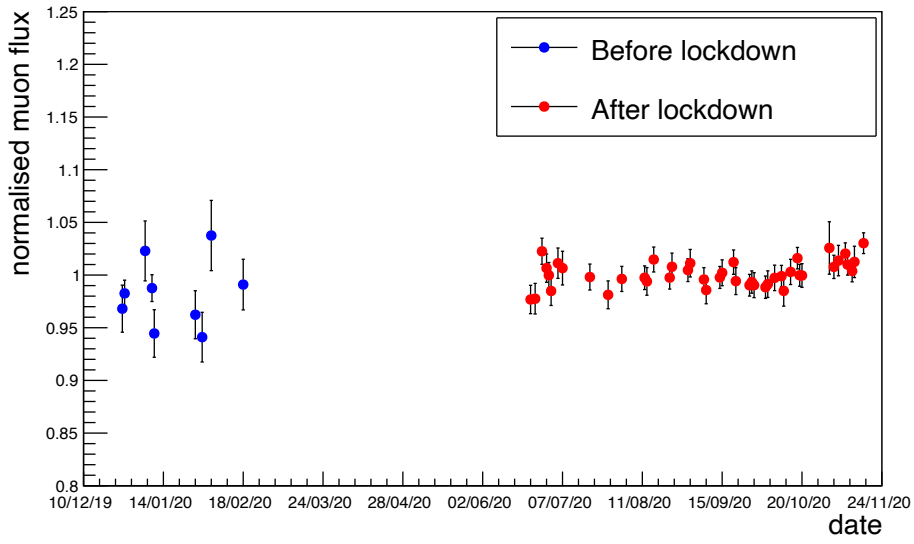

Figure 4.5: Normalised muon flux as a function of date. The gap between the two sets of data is the period of lockdown

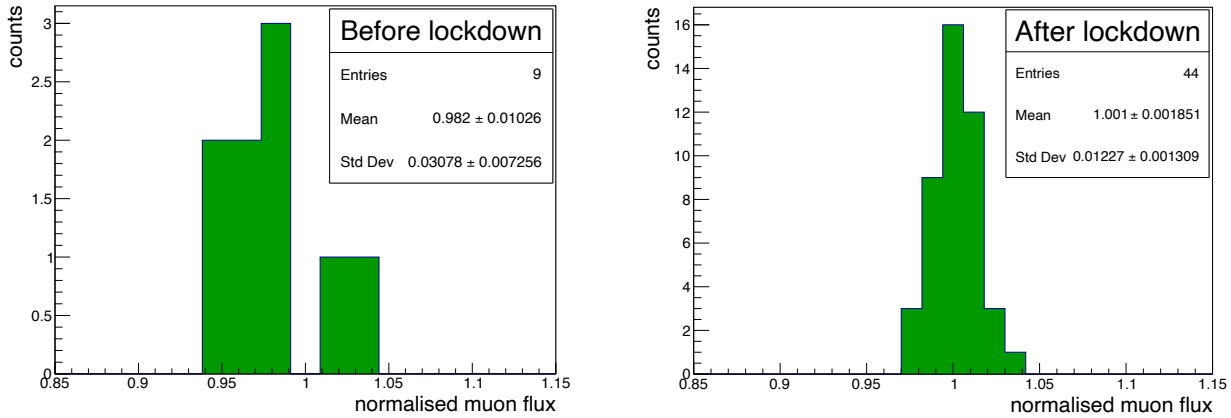

Figure 4.6: Distribution of normalised muon flux before and after the lockdown

of the air pollutants has been observed after the lockdown. One striking thing we observe during this study is that the concentration of O_3 also decreases after lockdown in our case unlike at Ref [2] where the concentration of O_3 was reported to be increased during lockdown (for a short time period though). Actually in Ref [2] the concentration of O_3 was reported to be increased during the lockdown (March 25 - April 6, 2020) compared to the values before the lockdown (March 10 - 20, 2020). In Ref [6], the concentration values of O_3 before the lockdown

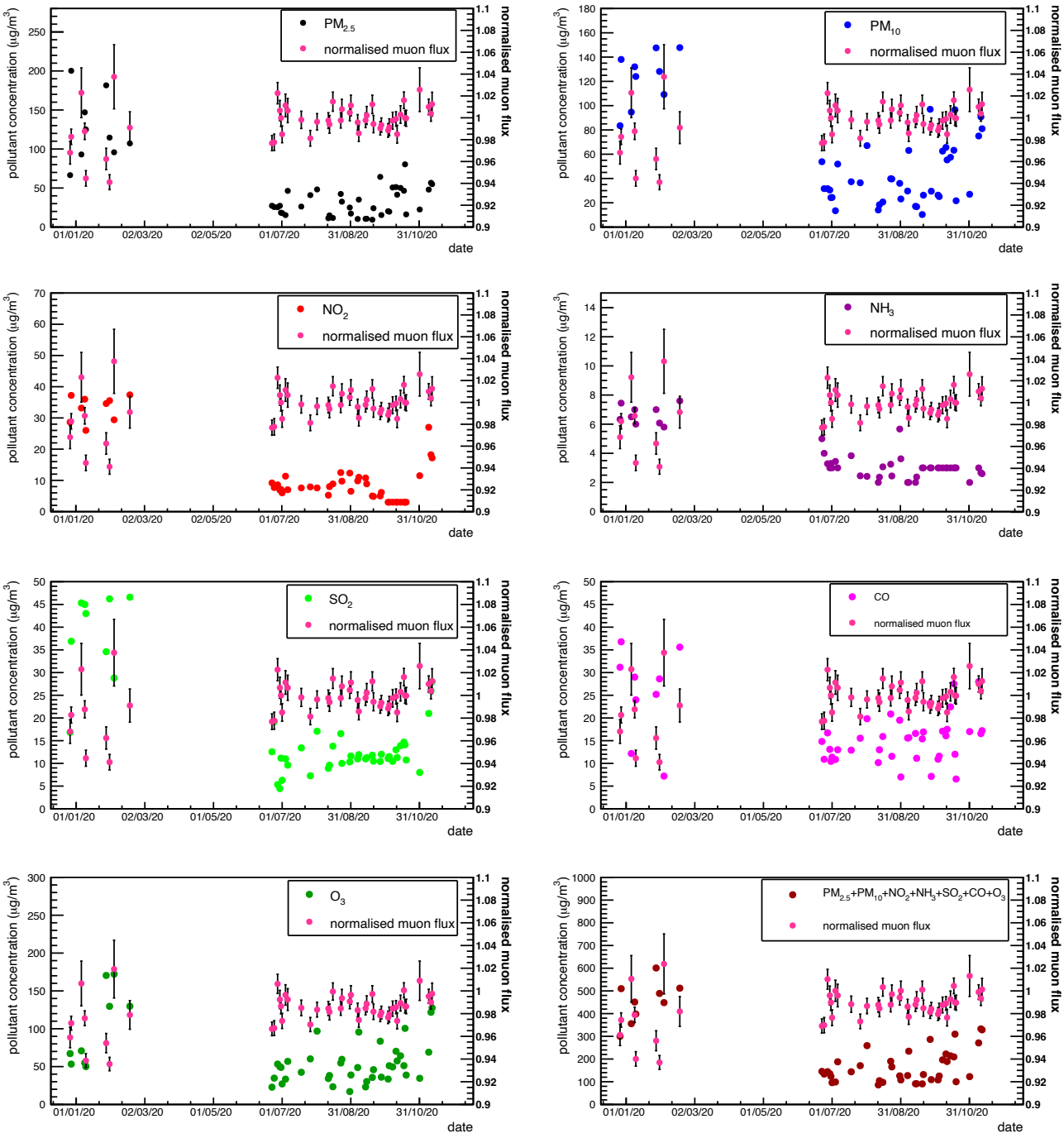

Figure 4.7: Pollutant concentrations (μg/m^3) of seven most abundant air pollutants measured at Bidhannagar, Kolkata station [6] and the normalised muon flux as a function of date

are quoted for December 27, 2019 to February 18, 2020 and after lockdown those are during

June 24, 2020 and November 17, 2020. Clearly, the dates in Refs [2, 6] are different and hence the discrepancy.

Figure 4.8 represents the variation of the muon flux with the density of the pollutants for the seven air pollutants individually and with the gross pollutants present. We observe a correlation between cosmic ray muon flux and the concentrations of the air pollutants before and after the lockdown where the flux increases with a decrease in the concentrations of the air pollutants.

The details of the variation as found by linear fitting of the muon flux vs pollutant concentration curve for different pollutants are tabulated in Table 4.1 below.

Table 4.1: Value of the fit parameters of the muon flux vs. pollutant concentration curve with 7 most abundant air pollutants.

Air pollutant type	p0	p1
$PM_{2.5}$	1.17 ± 0.003061	-0.0002475 ± 4.936e-05
PM_{10}	1.174 ± 0.003746	-0.0002763 ± 5.87e-05
NO_2	1.167 ± 0.003083	-0.0008197 ± 0.0002286
NH_3	1.182 ± 0.005682	-0.007278 ± 0.001676
SO_2	1.175 ± 0.003926	-0.001032 ± 0.0002183
CO	1.162 ± 0.003877	-0.0001226 ± 0.0001941
O_3	1.166 ± 0.004173	-0.0001161 ± 6.035e-05
Gross	1.176 ± 0.004605	-0.0001063 ± 2.617e-05

T/p normalised muon flux is also plotted as a function of the average concentration for the seven air pollutants individually and with the gross pollutants present in Figure 4.9. Here also we observed that the normalised flux increases with a decrease in the concentrations of the air pollutants.

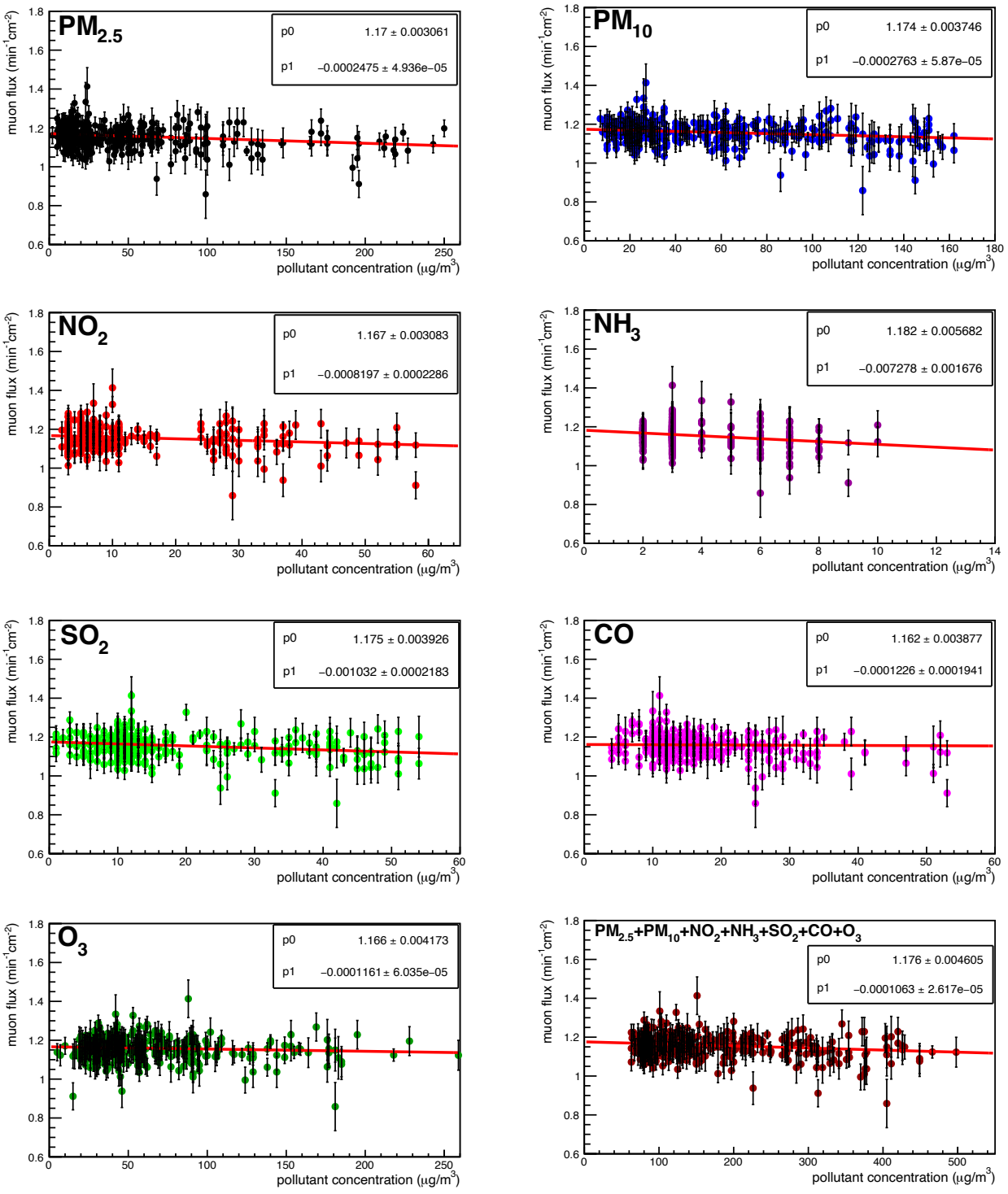

Figure 4.8: Measured muon flux as a function of pollutant concentrations of seven most abundant air pollutants

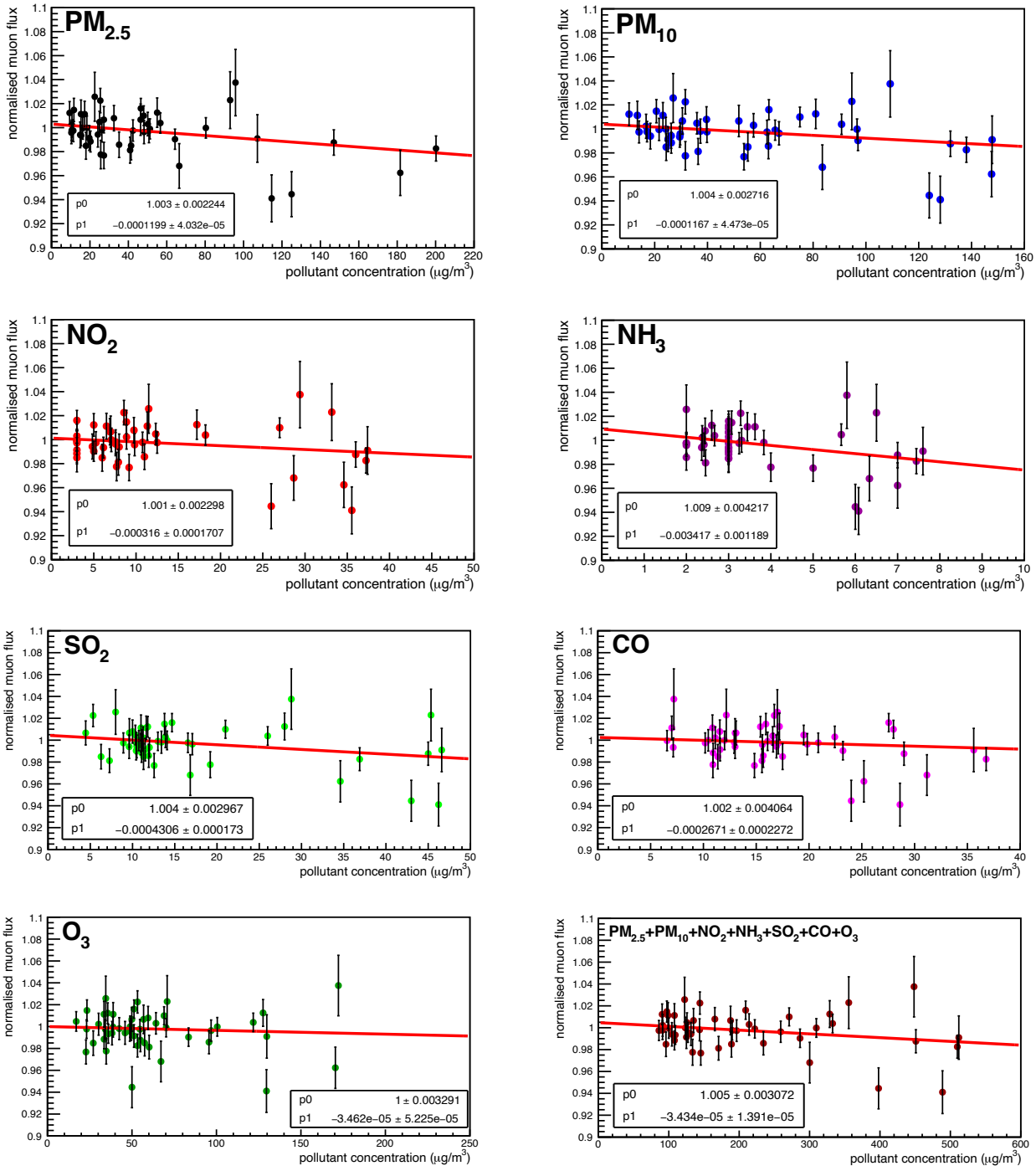

Figure 4.9: Normalised muon flux as a function of pollutant concentrations of seven most abundant air pollutants

4.4 Summary & Discussion

Cosmic ray muon flux is measured using the coincidence technique with plastic scintillation detectors before and after the lockdown. In this work, the temperature and pressure data of Kolkata are collected from online available information [6]. To restrict the outbreak of COVID-19, the Government of India imposed 67 days of nationwide complete lockdown in three phases. After that, the unlocking was declared in phases in different parts of India. Before the lockdown, we collected some cosmic ray flux data. After the lockdown, the measurement was continued to compare with the flux measured before the lockdown. In our measurement, it is found that the cosmic ray flux remained more or less unchanged before and after the lockdown. However, it is well known that there is an effect of atmospheric temperature and pressure on the cosmic ray flux and we also looked for any such possible correlation. A positive correlation is indeed observed between the muon flux and the ratio of atmospheric temperature and pressure. This correlation is fitted well by a function of the form *p0+p1(T/p)*, and the fit parameters *p0* and *p1* are used to normalise the *T/p* effect on the cosmic muon flux. It is found that the mean normalised muon flux before and after the lockdown period is 0.982 with a standard deviation of 0.031 and 1.001 with a standard deviation of 0.012 respectively.

A lockdown such as the one implemented due to the COVID-19 typically has a significant influence on the atmospheric condition in terms of the presence of pollutants. Our aim was to study any possible correlation of measured cosmic ray muon flux with this. To realise this, we considered the seven most abundant air pollutants ($PM_{2.5}$, PM_{10}, NO_2, NH_3, SO_2, CO, O_3) and investigated the change in their concentrations with the date (before and after lockdown). We found a significant declination in the concentrations of the pollutants and we tried to look for any correlation with the measured muon flux within the stipulated time window. The result shows a clear correlation as with decreasing concentrations of the air pollutants we observed an increasing trend of the normalised muon flux. From our observation, one can comment that the increase in cosmic ray flux can also be considered as one of the secondary indicators of less polluted air.

However, there are a few limitations of our measurement. First, the detector coverage area is very small, resulting in low statistics. Second, the statistics of muon data before the lockdown

is small. It will be very interesting if any other research laboratory having a large facility for cosmic ray flux measurement can try to study such correlation.

Bibliography

[1] V. Valkovič, Radioactivity in the Environment (2000), Pages 5-32, https://doi.org/10.1016/B978-044482954-2.50002-2.

[2] S. Jain *et al.*, Aerosol and Air Quality Research, 20: 1222-1236, (2020).

[3] S. Chen *et al.*, https://doi.org/10.1371/journal.pone.0215663 (2019).

[4] Abhijit Chatterjee *et al.*, Atmospheric Environment, https://doi.org/10.1016/j.atmosenv.2020.117947.

[5] https://www.covid19india.org/.

[6] https://app.cpcbccr.com/AQI_India/.

[7] S. Roy et al., Proceedings of ADNHEAP 2017, Springer Proceedings in Physics 2017, 199 - 204, ISBN 978-981-10-7664-0.

[8] S. Shaw *et al.*, Proceedings of the DAE Symp. on Nucl. Phys. 62 (2017) 1030.

[9] M. Neira, A. Prüss-Ustün and P. Mudu, Lancet 392: 1178-1179 (2018).

[10] M. Zazyan et al., J. Space Weather Space Clim., 5, A6 (2015).

[11] https://www.timeanddate.com/weather/india/kolkata

Chapter 5

Summary and Discussions

Compressed Baryonic Matter (CBM) experiment at the future Facility for Antiproton and Ion Research (FAIR) will mainly focus on the physics of Quark Gluon Plasma (QGP) which was formed in a few microseconds after the Big Bang and cover the whole early universe. CBM at FAIR is a fixed target experiment that will use proton and heavy ion beams to explore the QCD phase diagram at low temperature and moderate to high baryonic density regime. Also, one of the main questions CBM will explore is how the neutron star is formed. The equation of state will address those questions. Thus the CBM experiment has unique discovery potential because of very high beam intensity and high interaction rate.

In the CBM experiment, the measurements of $J/\psi \rightarrow \mu^+\mu^-$ and low mass vector meson (LMVM) decay $\rho \rightarrow \mu^+\mu^-$, $\omega \rightarrow \mu^+\mu^-$ and $\Phi \rightarrow \mu^+\mu^-$ in Au+Au collisions at 25 AGeV have been proposed as a key probe to the indication of in-medium modification of hadrons, chiral symmetry restoration and de-confinement at high baryon density (ρ_b). The Muon Chamber (MuCh) subsystem at the CBM experiment is dedicatedly designed to track the di-muons coming from the decay of LMVMs (ρ, ω, Φ) and charmonium (J/ψ). This will only be possible with the application of advanced instrumentation, including highly segmented and fast gas-filled detectors such as Gas Electron Multipliers (GEM), Resistive Plate Chamber (RPC), which will be used in the MuCh subsystem located downstream of the Silicon Tracking System (STS). According to the current design, MuCh consists of an absorber of 28 cm low-density graphite (density 1.78 g/cm^3) and 30 cm concrete (density $\sim$ 2.3 g/cm^3) combination, and after that, there will be three iron absorbers of thickness 20 cm, 20 cm, 30 cm respectively, interleaved

with detector stations, which will allow for tracking through the absorber stack. The muon detector in the CBM experiment will be constructed in such a way that there will be micro-pattern gaseous detectors with high-rate capability in the first two stations and other detectors like single gap RPC in the later stations. Due the foreseen high interaction rates and also to measure the physics observables precisely, the CBM detector system needs to be capable of handling large particle rates and also radiation hard. The ageing effect also needs to be very minimal for the long-term operation of all the detector subsystems.

As mentioned earlier, the RPC will be used in the 3^{rd} and 4^{th} stations of CBM-MuCh subsystem, where the area coverage would be quite large. In the 3^{rd} station, there will be 5° segmentation and in the 4^{th} station, there will be 6° segmentation. From the simulation, it has been predicted that there will be a particle rate of 15 kHz/cm^2 and 5.6 kHz/cm^2 respectively, on the 3^{rd} and 4^{th} stations for central Au-Au collations at 8 AGeV. To handle such a rate, it is necessary to use plates with low bulk resistivity. It is also necessary to operate the detector at a lower gas gain such that the dead time fraction is lower. India has the full responsibility for all the detectors and electronics for the MuCh setup in CBM.

The Resistive Plate Chamber (RPC) detector, usually made up of resistive electrode plates *e.g.* bakelite or glass, etc., is a well-known gaseous detector in the field of High Energy Physics experiments for triggering and tracking because of its good tracking capability, high efficiency, good time resolution, and low cost of fabrication. RPCs are also being used in several cosmic ray experiments to cover large detection area. Keeping in mind their high efficiency and cost-effectiveness, bakelite plates having moderate to low bulk resistivity are being explored for use as large-area RPC in future heavy-ion (HI) collision experiments. Future HI experiment CBM will use RPCs for muon detection in the Muon Chamber (MuCh subsystem).

The main issue in RPC is its limitation in the rate handling capability. Several experimental groups have developed sophisticated techniques to increase the particle rate capability and reduce the noise rate of this detector.

Generally, bakelite electrode plates suffer from surface roughness issue. If the surface is not smooth, the micro discharge probability and spurious pulses increase, which leads to the reduction of the performance of the detector. Also, this non-uniformity increases the spark probability.

In bakelite RPC, linseed oil coating is done to get rid of surface roughness issue. The linseed oil coating also helps to reduce the noise rate of the detector, protects the electrode plate from Hydrofluoric Acid (HF) corrosive effect and it also has photon quenching properties that reduce the UV sensitivity of the electrode plates. In conventional linseed oil-coated bakelite RPC a serious problem was observed in the BaBar experiment. The coated linseed oil formed stalagmite that subsequently forms the conducting paths through the gas gap around the spacers, and the discharge permanently damages the detector. The formation of stalagmite is due to the polymerisation of uncured linseed oil droplets present on the surface. However, a lot of R&D is performed, and the solution is found to overcome this issue.

The motivation of this thesis work was to search for a suitable detector for the 3^{rd} and 4^{th} stations of CBM-MuCh. An initiative is taken at Bose Institute for R&D of RPC detectors using moderate to low resistive bakelite plates commercially available in the local market of India for the 3^{rd} and 4^{th} stations of MuCh subsystem.

The thesis is constructed in the following way.

In Chapter 1, the CBM experiment at FAIR is introduced. Different sub-detector systems of the CBM experiment are described in a nutshell.

The historical development of RPC, along with its different types and modes of operation, are discussed in Chapter 2.

Chapter 3 described the detailed R&D on bakelite RPC prototypes for the CBM experiment. The outcome of the research work is described at a glance in the following paragraphs:

The aim of this research is to build RPC using indigenous materials for the CBM experiment. Several RPC modules are fabricated using commercially available bakelite plates. The electrical property of the materials (bulk resistivity) is studied. As a progress of the project, an oil-less single gap RPC prototype is built with indigenous bakelite plates of 2 mm thickness having bulk resistivity 3×10^{10} Ω cm. The gas gap of the prototype is also made of 2 mm. The chamber is tested in the avalanche mode with 100% Tetrafluoroethane gas. Standard NIM electronics have been used for this study. With this prototype, an efficiency $\sim$ 70% and time resolution 1.2 ± 0.03 ns (σ) are obtained from an applied voltage of 10.2 kV onwards.

Another prototype is then fabricated with the same material but with linseed oil coating on the inner surfaces. A new technique is followed for the linseed oil coating of the bakelite sheets. In conventional bakelite RPC, the linseed oil coating is done after making the gas gap. In the case of BaBar RPC, the performance deteriorated drastically due to the trapping of uncured linseed oil in the hidden storage cavities near the spacers. To ensure that the curing is properly done throughout the entire surface, in this particular work, the linseed oil coating is done before making the gas gap. After the linseed oil coating, the plates are cured for 15 days. The advantage of this procedure is that after linseed oil coating, it can be checked visually whether the curing is properly done or if any uncured droplet of linseed oil is present.

The detector is tested with 100% Tetrafluoroethane ($C_2H_2F_4$) gas in the avalanche mode. Efficiency plateau $\sim$ 95% from 9.4 kV onwards and $\sim$ 85% from 10.1 kV onwards are obtained for the -15 mV and -20 mV discriminator threshold respectively. The noise rate is found to be very high for such a chamber compared to the results reported earlier for the RPCs with oil-coated bakelite plates in the conventional way. The detection efficiency of the RPC in the cosmic ray test is compared with the conventional linseed oil-coated bakelite RPC. However, the leakage current and noise rate are comparatively high.

The chamber is subsequently tested with cosmic rays in avalanche mode using Tetrafluoroethane ($C_2H_2F_4$) and Isobutane (i-C_4H_{10}) gas mixture in 90/10 volume ratio. The leakage current through the RPC module is measured as a function of the applied HV. The efficiency and noise rate are also studied by varying the applied HV. With the gas mixture, the module is tested with - 20 mV and - 25 mV threshold settings for the LED. An efficiency of $\sim$ 95 $\pm$ 2% is achieved from 10 kV onwards for both the threshold settings. The maximum noise rates are found to be 120 Hz/cm^2 and 80 Hz/cm^2 for the - 20 mV and - 25 mV thresholds respectively. The best time resolution 0.8 $\pm$ 0.06 ns (σ) is obtained for an applied voltage of 10.4 kV.

To test the long-term stability, the detector is operated at 10.2 kV for a period of more than three month with a mixture of $C_2H_2F_4$ and i-C_4H_{10} in the 90/10 volume ratio and with 100% $C_2H_2F_4$. It is found that for $C_2H_2F_4$ and i-C_4H_{10} mixture and 100% $C_2H_2F_4$ the average efficiencies are found to be 88 $\pm$ 6 % and 93 $\pm$ 6 % respectively whereas the average noise rates for two compositions are found to be 189 $\pm$ 131 Hz/cm^2 and 208 $\pm$ 129 Hz/cm^2.

The prototype detector is also tested in the high-intensity gamma-ray environment background to have an idea about the behaviour in a real experiment-like scenario. A ^{137}Cs source of activity 13.6 GBq is used for this study. 662 keV photon is emitted from the source with an intensity of 46 kHz/cm^2. Very high efficiency for the cosmic ray muons is also obtained in the presence of high-intensity photons. This radiation tolerance test is very important, especially for high-energy heavy-ion collision experiments.

In this thesis work, a new RPC prototype is developed with a new method of linseed oil coating. This RPC can give a solution to the 3^{rd} and 4^{th} stations of CBM-MuCh. As proof of principle, a new technology of oil coating in RPC with bakelite electrodes is introduced. The characterisation studies with the cosmic test showed that this technology does work. The detector also passed the initial stability test. The detector performs well also in harsh radiation environments.

In Chapter 4, an application of the radiation detector is presented. As an application of the radiation detector, a study is performed to see the correlation between the concentration of air pollutants and the cosmic ray muon flux measured using the coincidence technique with plastic scintillation detectors. To restrict the outbreak of COVID-19, the Government of India imposed 67 days of complete nationwide lockdown in three phases. After that, the unlocking was declared in different phases in different parts of India. Before the lockdown, we collected some cosmic ray flux data during the characterisation of the RPC. After the lockdown, the measurement is continued to compare with the flux as measured before the lockdown. In our measurement, it is found that the cosmic ray flux remained more or less unchanged before and after the lockdown. However, it is well known that there is an effect of atmospheric temperature and pressure on the cosmic ray flux and we also looked for any such possible correlation. A positive correlation is indeed observed between the muon flux and the ratio of atmospheric temperature and pressure. This correlation is fitted well by a function of the form *p0+p1(T/p)*, and the fit parameters *p0* and *p1* are used to normalise the *T/p* effect on the cosmic muon flux.

A lockdown such as the one implemented due to COVID-19 typically has a significant influence on the atmospheric condition in terms of the presence of pollutants. We wanted to study any possible correlation of measured cosmic ray muon flux with this. To realise our goal, we considered the seven most abundant air pollutants ($PM_{2.5}$, PM_{10}, NO_2, NH_3, SO_2, CO, O_3)

and investigated the changes in their concentrations with time (before and after lockdown). We found a significant declination in the concentrations of the pollutants and we tried to look for any correlation with the measured muon flux within the stipulated time window. The result: a clear correlation with decreasing concentrations of the air pollutants and further an increasing trend of the normalised muon flux. From our observation, one can comment that the increase in the cosmic ray flux can also be considered as one of the secondary indications of less polluted air.

However, there are a few specific limitations of our measurement. First, the detector coverage area is very small, resulting in low statistics. Second, the statistics of muon data before the lockdown is small.

As a continuation of the present work, the following studies might be taken as a future work plan by the interested groups:

For such a newly developed RPC prototype, performance needs to be studied in a test beam in the accelerator under a harsh hadron environment. The long-term stability also needs to be studied under high particle radiation.

Appendix A

Implementation of Electronic FEB Id and channel Id for MuCh

In the CBM-MuCh, the first two stations will be equipped with GEM detector and the third and forth stations will be equipped with RPC detector. For both RPC and GEM detectors pad readout will be used. For the available GEM foil size, each layer of 1^{st} station has been divided into 18 modules (shown in Figure A.1). MuCh system is using STS-MUCH-XYTER ASIC readout for the individual pad. The ASIC contains 128 electronics channels (e-channel, for differentiation from the channel which is generated from simulation). In the first station, each module will include $23 \times 97 = 2231$ pads, which require at-least 18 Front-end Electronic Boards (FEBs) with one ASIC on it. In the mini CBM (mCBM) test beam campaign, two modules of GEM detector, equivalent of 1^{st} station of MuCh, have been configured according to the availability of FEBs and both modules could not be fully populated. In the simulation work, channels that are connected to Pads are implemented in Cbm-MuchPad class within the CbmRoot framework so that we can have information about physically connected FEBs and corresponding e-channels.

A.1 Implementation in CbmRoot Framework

A class named CbmMuchSegmentPar is implemented to map the channel and sector information of a module to the FEB id and e-channel id. Two getter functions in the CbmMuchPad class is implemented to extract the FEB Id and e-channel information, respectively. Cbm-

MuchSegmentPar class contains two 2D matrices. One matrix maps the FEB id, which varies from 0-17, and another maps the e-channel id from channel and sector information from CbmMuchAddress class. Each CbmMuchPad has a unique CbmMuchAddress from which channel and sector information is extracted and using CbmMuchSegmentPar FEB-Id and e-channel information gathered [1].

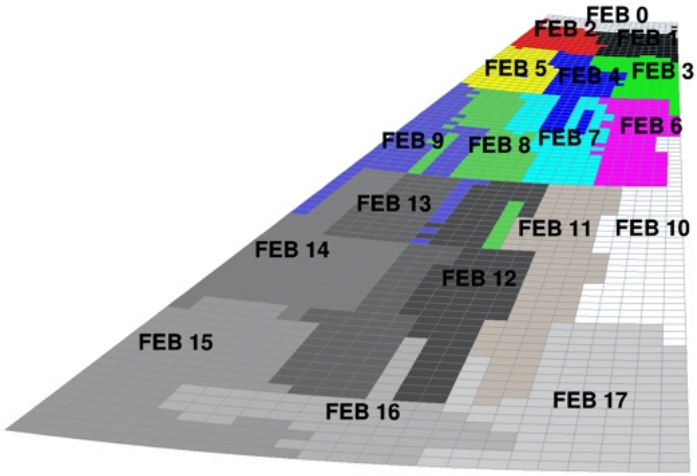

Figure A.1: 1^{st} station detector Module pad layout with FEB and e-channel representation drawn from simulation.

A.2 Result of simulation

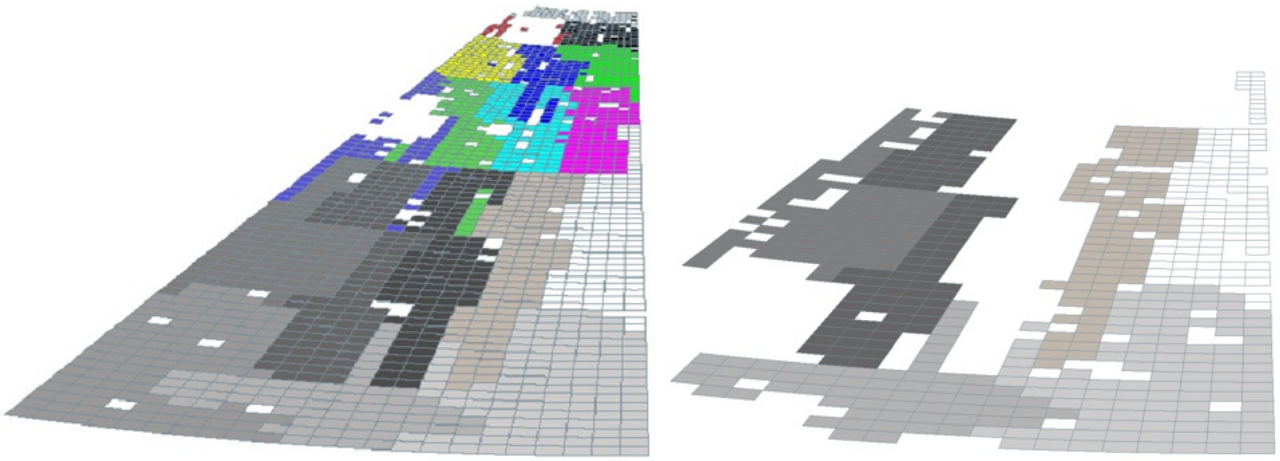

(a) Readout pad for detector Module 1 (b) Readout pad for detector Module 2

Figure A.2: Pad drawn from mCBM data.

A macro is written for pictorial representation and to draw the pad from the FEB and Channel information. Also, the same is used for mCBM data to compare with the simulation result. The Monte Carlo (MC) points are generated using transport macro. The PCB diagram obtained from the simulated data is shown in Figure A.1. Different colour represents the different FEB connection to associated e-channels, and the FEB number is indicated according to the convention used in the mCBM.

The PCB from the mCBM data (run number 380 taken in December 2019), which is drawn using the address variable of CbmMuchPad is shown in Figure A.2. In Figure A.2(a), the first GEM module is shown with all 18 FEB connected and in Figure A.2(b), the second GEM module is shown with 6 FEB connected in it. The blank spaces are due to the non-availability of FEB on these locations [1].

Bibliography

[1] Implementation of Electronic FEB Id and channel Id for MUCH.
A. Sen and V. Singhal
CBM Progress report 2019, 75. ISBN: 978-3-9815227-8-5 DOI: 10.15120/GSI- 2020-00904

Reprints

Published by IOP Publishing for Sissa Medialab

Received: *April 14, 2020*
Revised: *May 3, 2020*
Accepted: *May 4, 2020*
Published: *June 26, 2020*

XV Workshop on Resistive Plate Chambers and Related Detectors
10–14 February, 2020
University of Rome Tor Vergata, Rome, Italy

Characterisation of an RPC prototype with moderate resistivity plates using tetrafluoroethane ($C_2H_2F_4$)

A. Sen,[1] **S. Chatterjee, S. Roy, S. Biswas and S. Das**

Department of Physics and Centre for Astroparticle Physics and Space Science (CAPSS), Bose Institute, EN-80, Sector-V, Bidhannagar, Kolkata-700091, India

E-mail: arindam@jcbose.ac.in

Abstract: Keeping in mind the requirements of high rate capable, cost effective, large area detectors to be used in future high energy physics experiments, commercially available bakelite plates having moderate bulk resistivity are used to build an RPC module. The chamber is tested with cosmic rays in the avalanche mode using 100% Tetrafluoroethane ($C_2H_2F_4$). Standard NIM electronics are used for this study. The efficiency, noise rate and time resolution are measured. The detailed method of measurement and the first test results are presented.

Keywords: Gaseous detectors; Gaseous imaging and tracking detectors; Resistive-plate chambers

ArXiv ePrint: 2004.05469

[1]Corresponding author.

https://doi.org/10.1088/1748-0221/15/06/C06055

Contents

2020 JINST 15 C06055

1 Introduction

Since the invention of the Resistive Plate Chambers (RPCs) [1] as a cost effective technology that can be used to build large area granular, reasonably fast and high rate capable detectors, it has found use not only in a large number of high energy physics experiments [2–7] as trigger, Time of Flight (TOF) and tracking devices but also in several cosmic ray experiments [8, 9] and Neutrino experiments [10–12]. Future experiments such as Compressed Baryonic Matter (CBM) at FAIR also propose to use RPCs as one of the key detectors [13].

Keeping in mind the possibility of using RPCs as future high rate ($\sim$ 15 kHz/cm^2) capable tracking detectors, we have taken up a study to characterise an RPC prototype built using a particular type of bakelite plates with moderate bulk resistivity. The prototype is tested with 100% Tetrafluoroethane ($C_2H_2F_4$) gas for the first time in this work.

2 Detector description and experimental set-up

The detector prototype is built with two 2 mm thick bakelite plates, each having dimension 30 cm $\times$ 30 cm and bulk resistivity $3 \times 10^{10}\,\Omega$ cm (at 22°C temperature and 60% Relative humidity) and without any linseed oil coating inside. The gas gap is maintained with four edge spacers having width 1 cm, thickness 2 mm and one button spacer having 1 cm diameter, thickness 2 mm. Both the spacers are made of perspex (resistivity $\sim 10^{15}\,\Omega$ cm). The surface resistivity of the graphite layer is measured to be $\sim 500\,\mathrm{k}\Omega/\square$. Two 1 cm $\times$ 1 cm copper tapes are used at two diagonally opposite corners to apply high voltage (HV). HV of opposite polarities are applied on two sides. To collect the signals copper pick-up panels are used. They are made of 2.5 cm wide strips with a separation of 2 mm between two consecutive ones.

The signals from the pick-up strips are fed to a 10X fast amplifier and then to the discriminator. The cosmic ray master trigger is made using three fast plastic scintillators. Among them, two scintillators (with dimensions 10 cm $\times$ 10 cm and 2 cm $\times$ 10 cm respectively) are placed above and one (with dimension 20 cm $\times$ 20 cm) is placed below the RPC module. The scintillators make the trigger window of area 2 cm $\times$ 10 cm. Thresholds to the discriminators are set to -15 mV for all the scintillators and also for the RPC. The width of the 3-Fold scintillator master trigger is set to

150 ns. Finally, the discriminated RPC signal from one single strip is taken in coincidence with the 3-Fold master trigger and a 4-Fold NIM signal is obtained. The ratio of the 4-Fold signal and the 3-Fold scintillator signal is defined as the efficiency of the detector. The single RPC signals are also counted for a particular duration and the rate is defined as the noise rate of the chamber.

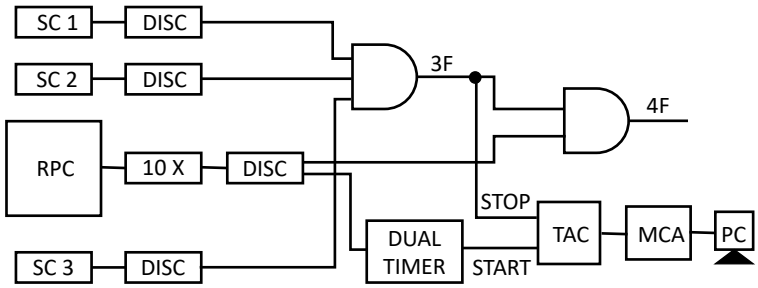

Figure 1. Schematic representation of the cosmic ray test setup. SC 1, SC 2 and SC 3 are the plastic scintillators of dimensions 10 cm × 10 cm, 2 cm × 10 cm and 20 cm × 20 cm. respectively. DISC, 10 X, TAC, MCA and PC are the discriminators, 10X fast amplifier, Time to Amplitude Converter, Multi Channel Analyser and Personal Computer respectively.

To measure the timing properties of the RPC, the same set-up is used. The discriminated RPC signal is stretched by a dual timer and fed as the START signal of the Time to Amplitude Converter (TAC). The 3-Fold scintillator coincidence signal is taken as the STOP signal input of the TAC. The output of the TAC is fed to the Multi Channel Analyser (MCA) and the spectra are stored in a Personal Computer (PC). Figure 1 shows the schematic of the set-up for testing the RPC module using cosmic rays.

During the whole measurement, the temperature and relative humidity inside the laboratory are maintained at ∼ 18–20°C and 37–40% respectively whereas the atmospheric pressure is monitored to be 1009–1020 mbar.

3 Results

In this work, the efficiency, noise rate, time difference of RPC signal and the master trigger and time resolution of an oil-less bakelite RPC as a function of voltage are measured with cosmic rays. The detector current as a function of the bias voltage is shown in figure 2. It is visible that initially the current increases slowly with the voltage and above 8 kV across the gas gap the increase becomes rapid. At 8 kV voltage difference across the gap the signal of amplitude ∼ 10–15 mV is observed in the oscilloscope at 50 Ω termination. The result has been compared with the one obtained using Argon/CO_2 gas in 70/30 ratio. Sharp breakdown in the I-V characteristics resulted with Argon/CO_2 at a lower voltage compared to that with the Tetrafluoroethane.

The noise rate as a function of voltage is measured for two consecutive days keeping the discriminator threshold at −15 mV and the results are shown in figure 3. It is seen that for both days the noise rate increases with applied voltage but on the second day, the noise rate is found to be much less than that of the first day, because of better conditioning. The conditioning is done with continuous gas flow and keeping 4 kV across the gas gap over-night. It is to be mentioned here that,

2020 JINST 15 C06055

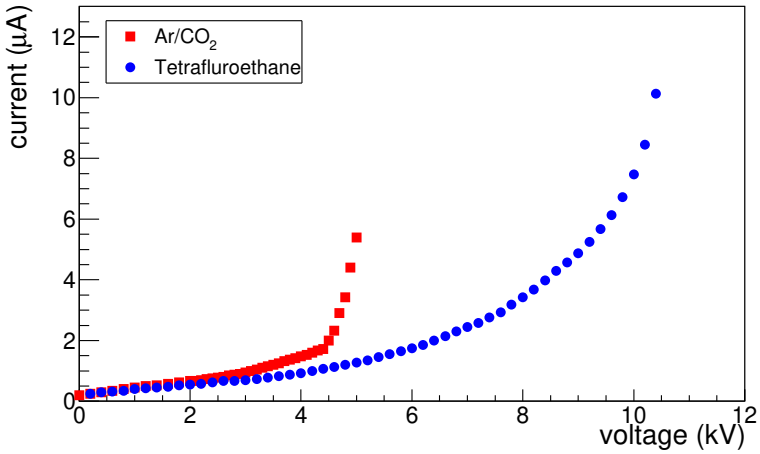

Figure 2. The I-V Characteristics of RPC with two gas mixtures.

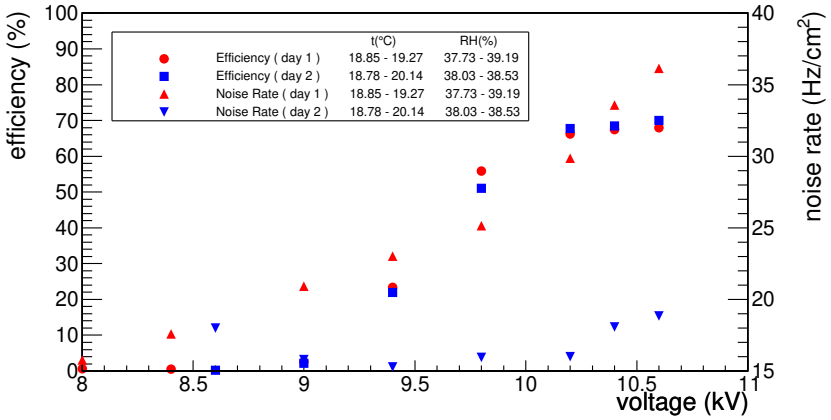

Figure 3. Efficiency and noise rate as a function of voltage.

for linseed oil treated RPCs the noise rate with cosmic rays is found to be one order of magnitude better in some cases [14] and even two orders of magnitude for streamer operated RPCs with higher resistivity [15–17].

From figure 3 it can also be seen that the efficiency starts increasing from 9 kV and saturates at a value of 70% from 10.2 kV onwards. The same result is observed on both days.

While measuring the time resolution the RPC signal is stretched to 500 ns to avoid the effect of double or reflection pulses if there is any. The full scale of the TAC is set to 100 ns. The typical time spectrum for the RPC is shown in figure 4. The distribution of the time difference between the RPC signal and the master trigger is fitted with the Gaussian function. Finding the σ of the distribution and subtracting the contribution from the scintillator in quadrature the intrinsic time resolution of the RPC is calculated.

The time difference of the RPC signal with respect to the master trigger and the time resolution (σ) of the RPC as a function of the applied voltage are shown in figure 5. Since the RPC signal

2020 JINST 15 C06055

is used as the START signal and with the increase of the applied voltage the electric field inside the RPC becomes stronger, electrons travel faster and the signals arrive earlier. As a result with the increase of applied voltage the time difference increases and reaches a plateau from 10.2 kV onwards. The time resolution (σ) decreases and a value $\sim$ 1.2 ns is obtained from 10.2 kV.

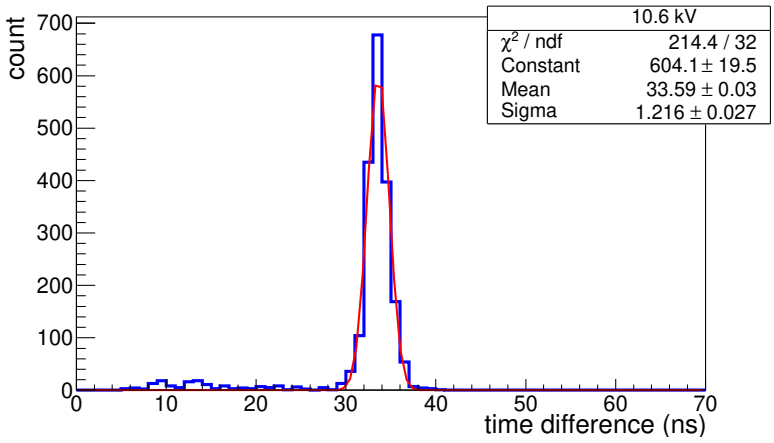

Figure 4. Time spectrum of RPC at a voltage difference 10.6 kV across the gas gap.

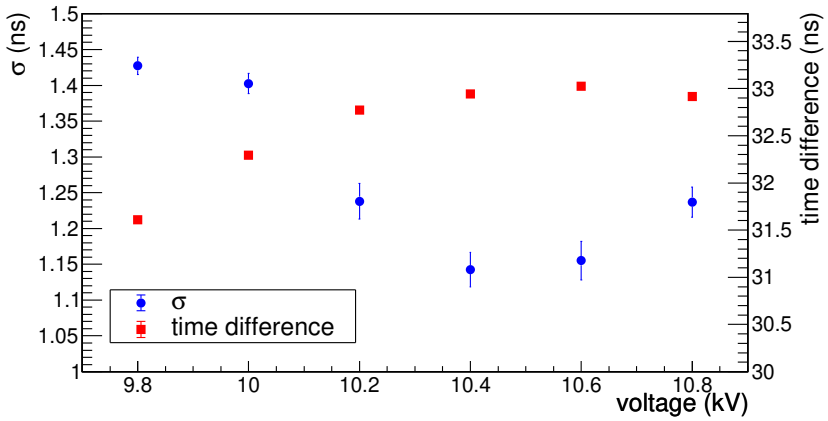

Figure 5. Time resolution and time difference of RPC signal and master trigger as a function of voltage.

4 Summary and outlook

An oil-less single gap RPC prototype is built with indigenous bakelite plates having bulk resistivity $3\times10^{10}\,\Omega\,$cm. The chamber is tested in the avalanche mode with 100% Tetrafluoroethane gas. With this prototype, an efficiency $\sim$ 70% and time resolution 1.2 ns (σ) are obtained from an applied voltage of 10.2 kV onwards. Investigation of the reason behind lower efficiency is going on. One probable reason for the limitation in the efficiency is the voltage drop on the electrodes because of high current. Other Tetrafluoroethane based conventional gas mixtures will be tried. Estimation of the induced signal charge and the long-term stability test of this particular chamber is also in future plan.

High rate handling capability is one of the crucial factors for detectors to be used in many current and future high energy physics experiments. In that direction, we are searching for indigenous bakelite plates with better surface smoothness and lower resistivity.

Acknowledgments

The authors would like to thank Prof. Sanjay K. Ghosh, Prof. Sibaji Raha, Prof. Rajarshi Ray and Dr. Sidharth K. Prasad for valuable discussions and suggestions in the course of the study. We would also like to thank Ms. Aayushi Paul of University of Calcutta and Ms. Rituparna Banerjee of IIT-ISM, Dhanbad for the calibration of the TAC and measurement of bulk resistivity of bakelite plates. This work is partially supported by the research grant SR/MF/PS-01/2014-BI from DST, Govt. of India and the research grant of CBM-MuCh project from BI-IFCC, DST, Govt. of India. A. Sen acknowledges his Inspire Fellowship research grant [DST/INSPIRE Fellowship/2018/IF180361]. S. Biswas acknowledges the support of Intramural Research Grant provided by Bose Institute.

References

[1] R. Santonico and R. Cardarelli, *Development of Resistive Plate Counters*, *Nucl. Instrum. Meth.* **187** (1981) 377.

[2] BaBar Collaboration, *Technical Design Report*, SLAC-R-95-457.

[3] E. Cerron Zeballos, I. Crotty, D. Hatzifotiadou, J. Lamas Valverde, S. Neupane, M.C.S. Williams et al., *A New type of resistive plate chamber: The Multigap RPC*, *Nucl. Instrum. Meth. A* **374** (1996) 132.

[4] R. Arnaldi et al., *A low-resistivity RPC for the ALICE dimuon arm*, *Nucl. Instrum. Meth. A* **451** (2000) 462.

[5] ATLAS collaboration, *ATLAS Muon Spectrometer: Technical Design Report*, CERN-LHCC-97-022.

[6] CMS collaboration, *The CMS muon project: Technical Design Report*, CERN-LHCC-97-032.

[7] D. Belver et al., *The HADES RPC inner TOF wall*, *Nucl. Instrum. Meth. A* **602** (2009) 687.

[8] J.-F. Han, Q. Liu, Y.-G. Xie, Q.-M. Zhang, S. Qian, L.-H. Ma et al., *Cosmic ray test results on resistive plate chamber for the BESIII experiments*, *Nucl. Instrum. Meth. A* **577** (2007) 552.

[9] Argo-YBJ collaboration, *Layout and performance of RPCs used in the Argo-YBJ experiment*, *Nucl. Instrum. Meth. A* **562** (2006) 92.

[10] R. Acquafredda et al., *The OPERA experiment in the CERN to Gran Sasso neutrino beam*, 2009 *JINST* **4** P04018.

[11] Q. Zhang, Y. Wang, J. Zhang, J. Cao, T. Kwok, Y.-K. Hor et al., *An underground cosmic-ray detector made of RPC*, *Nucl. Instrum. Meth. A* **583** (2007) 278 [*Erratum ibid.* **586** (2008) 374].

[12] S. Biswas, S. Bhattacharya, S. Bose, S. Chattopadhyay, S. Saha, M.K. Sharan et al., *Performances of linseed oil-free bakelite RPC prototypes with cosmic ray muons*, *Nucl. Instrum. Meth. A* **602** (2009) 749 [arXiv:0907.2976].

[13] I. Deppner et al., *The CBM time-of-flight wall*, *Nucl. Instrum. Meth. A* **661S1** (2012) S121.

[14] B. Liberti et al., *ATLAS RPC perfomance on a dedicated cosmic ray test-stand*, *Nucl. Phys. B Proc. Suppl.* **177-178** (2008) 307.

2020 JINST 15 C06055

[15] A. Bergnoli et al., *Tests on OPERA RPCs*, *Nucl. Phys. B Proc. Suppl.* **158** (2006) 93.

[16] A. Bergnoli et al., *Tests of OPERA RPC Detectors*, *IEEE Trans. Nucl. Sci.* **52** (2005) 2963.

[17] ALICE collaboration, *Performance of the RPC-based ALICE muon trigger system at the LHC*, 2012 *JINST* **7** T12002 [arXiv:1211.1948].

2020 JINST 15 C06055

Nuclear Inst. and Methods in Physics Research, A 1024 (2022) 166095

Contents lists available at ScienceDirect

Nuclear Inst. and Methods in Physics Research, A

journal homepage: www.elsevier.com/locate/nima

A new technique of linseed oil coating in bakelite RPC and the first test results

A. Sen [*,1], S. Chatterjee[1], S. Das[1], S.K. Ghosh[1], S. Biswas[1]

Department of Physics and Centre for Astroparticle Physics and Space Science (CAPSS), Bose Institute, EN-80, Sector V, Kolkata 700091, India

ARTICLE INFO

Keywords:
Resistive plate chambers
Gaseous detectors
Linseed oil coating
Efficiency
Noise rate
Bakelite

ABSTRACT

Single gap Resistive Plate Chamber (RPC) is one of the very popular gaseous detectors used in high-energy physics experiments nowadays. It is a very fast detector having low cost of fabrication. The RPCs are usually built using glass or bakelite plates having high resistivity $\sim 10^{10}$–10^{11} Ω cm. Bakelite RPCs are generally fabricated with a linseed oil coating inside to make the inner electrode surface smoother which helps to reduce the micro discharge probability. Linseed oil coating also reduces the surface UV sensitivity dramatically and effectively protect the bakelite surfaces from the Hydrofluoric Acid (HF), produced by the interaction of fluorine with the water vapour. There is a conventional way to do this linseed oil coating after making the gas gap as done in experiments *e.g.* ALICE, CMS etc. A new technique is introduced here to do the linseed oil coating on the bakelite plate before making the gas gap. 100% Tetrafluoroethane ($C_2H_2F_4$) gas is used to test the RPC module in the avalanche mode with cosmic rays. Conventional NIM electronics is used for this study. The efficiency and noise rate are measured. In this article, the detailed method of fabrication and the first test results are presented.

1. Introduction

Resistive Plate Chambers (RPCs) are widely used in high-energy physics experiments for their high efficiency, excellent time resolution, hassle-free maintenance and low cost of fabrication [1]. In current high-energy physics experiments this parallel plate gaseous detector is mainly used for triggering and tracking purposes due to its excellent time resolution and high efficiency [2–8]. RPCs are also used in cosmic ray experiments and neutrino experiments for muon detection where large area coverage with minimal cost is required [9–15]. Future experiments such as Compressed Baryonic Matter (CBM) at Facility for Antiproton and Ion Research (FAIR) propose to use RPCs as one of the key detectors for time of flight (TOF) measurements [16].

The RPCs are usually built using glass or bakelite plates having high resistivity $\sim 10^{10}$–10^{11} Ω cm. The inner surfaces of the bakelite plates that face the filled gas are usually coated with linseed oil paint. The linseed oil is a fatty acid (R-COOH), an organic acid that contains the glycerides of linolenic, linoleic, oleic, stearic, and palmitic acids with a high degree of unsaturation of its fatty acid radicals [17]. The linseed oil coating reduces the spurious micro discharge on the inner surfaces. If the micro discharge probability is reduced, we can have a better performance compared to the RPC without oil coating [1,18,19]. To reduce the after-pulse/noise rate, low UV sensitive material for the electrode is desirable. It is reported earlier that the linseed oil coating reduces the surface UV sensitivity dramatically [18]. Hydrofluoric Acid (HF), produced by the interaction of fluorine with the water vapour, is chemically very reactive. It can affect different materials and has corrosive action. It is reported that the linseed oil coating on the bakelite surface can effectively protect it from the HF vapour attack [18]. That means the linseed oil treatment on the inner surfaces of the bakelite electrodes is an essential process for the optimum performance (high efficiency and low noise level) of RPC. For this treatment the inner surfaces of the RPC usually the gas gap is filled with low viscous linseed oil and thinner solution and the liquid is drained out slowly. Dry air is flown through the gas gap to cure the thin linseed oil layer left on all the inner surfaces of the plates as well as those of the spacers [20–22].

However, serious operational problems were observed in the bakelite RPCs in BaBar experiment. It was observed that the conducting paths through the gas gap, mainly around the spacers, created due to the formation of stalagmites by polymerisation of uncured linseed oil droplets, trigger discharges thereby resulting in irreversible damage to the bakelite plates [17,23]. The process of linseed oil treatment was later changed by increasing the ratio of the solvent to produce a thinner coating (10-30 μm) on the surfaces [24]. Efforts were subsequently made to look for alternatives to linseed oil treatment, or even to develop bakelite sheets that can be used without the application of linseed oil [22].

One of the main limitations of RPC is that its low particle rate handling capability [25]. Nowadays RPC detector can handle a particle rate ~10 kHz/cm^2 in the avalanche mode of operation [26] but for

* Corresponding author.
E-mail address: arindam@jcbose.ac.in (A. Sen).
[1] All the authors have equal credit for the work.

https://doi.org/10.1016/j.nima.2021.166095
Received 15 August 2021; Received in revised form 31 October 2021; Accepted 7 November 2021
Available online 10 December 2021

the future experiments, detectors with high particle rate handling capability (~15 kHz/cm^2) is required [27]. One of the ways of increasing the particle rate handling capability in RPC is the use of low resistive electrode plates of the detector. It is to be mentioned also that the mode of operation depends on used gas and applied voltage [28]. For high rate operation, the option is the avalanche mode.

Keeping in mind the possibility of using bakelite RPCs as future high rate capable tracking detectors, we have taken up a study to characterise RPC prototypes built using a particular type of bakelite plates with moderate bulk resistivity. The first prototype was built without any oil coating inside, with indigenous bakelite plates having bulk resistivity 3×10^{10} Ω cm. The prototype was tested with 100% Tetrafluoroethane ($C_2H_2F_4$) gas. With this prototype, an efficiency ~70% was obtained with an applied voltage of 10.2 kV onwards [29].

In the present work, we built a linseed oil coated bakelite RPC. However, in this work, we have adopted a different technique for the linseed oil treatment. In contrary to the usual procedure, the bakelite plates are coated with linseed oil before making the gas gap.

The prototype is tested with cosmic ray using 100% Tetrafluoroethane ($C_2H_2F_4$) gas and conventional NIM electronics. In this article, we report the first result of the bakelite RPC, fabricated using a new technique of linseed oil coating.

2. Fabrication of the detector

Two bakelite plates having a dimension 27 cm × 27 cm and thickness 2 mm are used as the electrodes. The bulk resistivity of the plates is measured to be ~3×10^{10} Ω cm at 22 °C temperature and 60% relative humidity. At first, the bakelite plates are cleaned using an isopropyl alcohol bath. Commercially available linseed oil is used for the inside coating. The linseed oil coating is done here in a similar way as the silicone oil coating technique followed in Ref. [14]. About 2 g of linseed oil is applied over the 27 cm × 27 cm area of each plate. Based on the specific gravity (0.930 at 15.5 °C) of the fluid, the estimated coating thickness would be ~30 μm. The linseed oil is distributed over the surfaces and both the plates are left for 15 days in a sealed box for curing. Two plates are then cleaned again with dry air. Uniform separation between the electrode plates is ensured by using four edge spacers of dimension 27 cm × 1 cm and thickness 2 mm and one button spacer of diameter 10 mm and thickness 2 mm. All the spacers are made of polycarbonate. Two nozzles also made of polycarbonate (resistivity ~ 10^{15} Ω cm) for gas inlet and outlet are used as part of edge spacers. All the spacers are glued on one plate in the oil coated side using Araldite epoxy adhesive. The glued plates are kept for 24 h for curing and the other plate is glued on it and kept again for curing for 24 h. All the gluing processes are carried out on a laminar flow table. After cleaning, a thin layer of graphite is coated at the outer surfaces of the bakelite plates for the distribution of voltage. A gap of 1 cm from the edges of the plate to the graphite layer is maintained to avoid external electrical discharge. The average surface resistivity of the two graphite layers are found to be ~510 kΩ/□ and 540 kΩ/□ respectively. Two 1 cm × 1 cm copper tapes of ~20 μm thickness are pasted at two diagonally opposite corners to apply high voltage (HV). The HV cables are soldered on these copper strips. These copper strips are covered using Kapton tapes for isolation. Equal HVs with opposite polarities are applied on two surfaces. The steps of building of the module are shown in Fig. 1.

2.5 cm wide copper (20 μm thick) pick-up strips are fabricated having 2 mm separation among two consecutive strips, in order to collect the accumulated induced charge and are placed above the graphite layers. The pick-up strips are made by the etching process of one side from a double sided copper cladded, 2 mm thick G-10 sheet. The other side copper layer of the G-10 sheet is used as the ground plane. The strips are covered with 100 μm thick mylar foils to isolate them from the graphite layers. The signals from the strips are collected through RG-174/U coaxial cables.

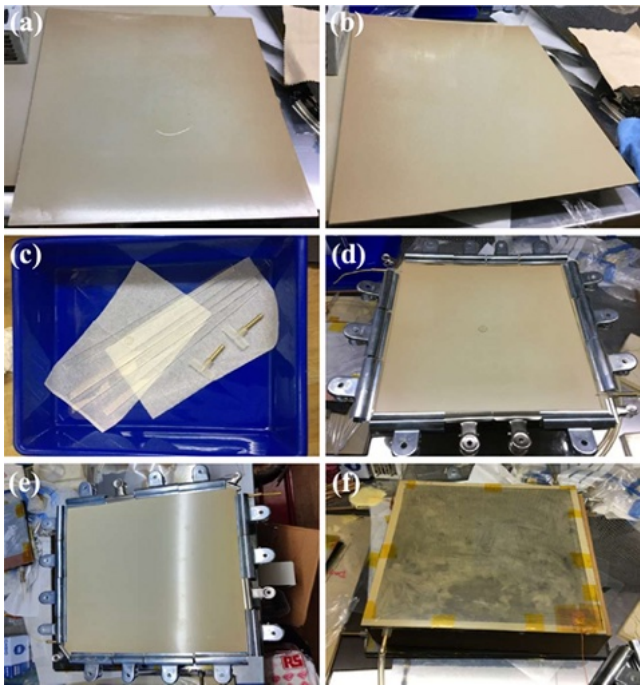

Fig. 1. Steps of building the RPC module. (a) Application of linseed oil on the bakelite surface, (b) cured linseed oil coated bakelite surface, (c) polycarbonate made gas nozzles and spacers, (d) gluing of spacers and nozzles on one bakelite plate, (e) making of gas gap after gluing the second plate, (f) complete RPC module after graphite coating.

3. Experimental set-up

Three plastic scintillation detectors, two placed above the RPC module and one placed below, are used to obtain the trigger from the incoming cosmic rays. The coincidence signal obtained from the top most paddle scintillator (SC1) having dimension 10 cm × 10 cm, a finger scintillator (SC2) of dimension 10 cm × 2 cm and the paddle scintillator (SC3) having dimension 20 cm × 20 cm are taken as the trigger (3-fold). RPC is placed in between the finger (SC2) and the paddle scintillator (SC3). All the scintillators are operated at 1550 V and −15 mV threshold is applied to the leading edge discriminator (LED).

The RPC signal from the pick-up strip is first fed to the 10x fast amplifier and the output of it then goes to the LED. Different thresholds are applied to the LEDs to reduce the noise. From the LED one output goes to the scaler to count the number of signals from the RPC which is known as the noise count or singles count of the chamber. The other output from LED goes to the dual timer where the discriminated RPC signal is stretched to avoid any double counting of the pulses and also to apply the proper delay to match the signal with the trigger. The output of the dual timer is put in coincidence with the trigger and this is defined as the 4-fold. The window of the cosmic ray test set-up is of area 10 cm × 2 cm. The detailed block diagram of this arrangement is shown in Fig. 2.

100% Tetrafluoroethane ($C_2H_2F_4$) gas is used as the active medium. A typical gas flow rate of 2 ml/min equivalent to 6 gap volume changes per day is maintained by using two needle valves.

The HVs to the RPC module are applied at a ramp-up rate of 2 V/s on both the sides. The leakage currents from both the side as measured by the HV module are also recorded. The temperature and the humidity are also recorded at the time of measurement using a data logger, built-in house [30].

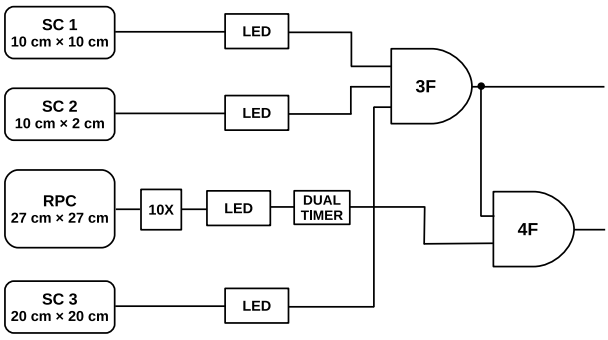

Fig. 2. Schematic of the experimental set-up.

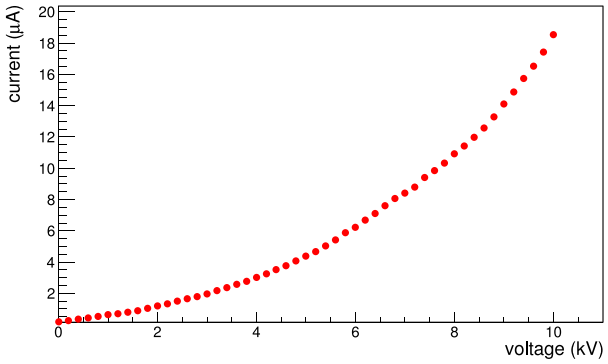

Fig. 3. Leakage current as a function of the applied voltage for the RPC module. The error bars are smaller than the symbols.

4. Result

After building the chamber, 100% $C_2H_2F_4$ gas is purged for 24 h before application of HV. To check the performance of the detector, firstly the leakage current through the RPC module is measured as a function of the applied HV and shown in Fig. 3. Breakdown of the gas, although not sharp, is seen at about ∼8 kV. The gas gap behaves as an insulator in the low applied voltage range and hence the slope over this voltage region scales as the conductance of the polycarbonate spacers. At higher range of voltage, the gas behaves as a conducting medium due to the ionisation. Therefore, the slope over this range scales as the conductance of the bakelite plates. The curve of leakage current vs. voltage as found here is not only very similar to the curve as reported earlier [20] but the magnitude of current is also comparable.

For the test using cosmic rays, the efficiency of the RPC is defined as the ratio of the 4-fold counts of the RPC to the 3-fold trigger count of the plastic scintillator telescope for a fixed duration. The noise rate (or singles count rate) of the RPC is defined as the number of counts per unit area of the strip per second. The efficiency and the noise rate are studied by varying the applied HV. Both the efficiency and noise rate are measured for two different discriminator threshold settings, −15 mV and −20 mV respectively for the RPC. The temperature and relative humidity values during these measurements are recorded and the average temperature is found to be about 25 °C and 27 °C, respectively and the average relative humidity is found to be 44% in both the cases. The efficiency and the noise rate as a function of voltage is shown in Fig. 4. For −15 mV threshold setting the efficiency increases with applied voltage and reaches a plateau at ∼95% from 9.4 kV onwards whereas for −20 mV threshold setting the efficiency saturates at ∼85% from the applied voltage of 10.1 kV onwards. The noise rate increases with applied HV. The noise rate is measured to be much higher for the lower threshold with a maximum value of ∼500 Hz/cm^2. For −20 mV threshold the maximum noise rate is found to be ∼200 Hz/cm^2.

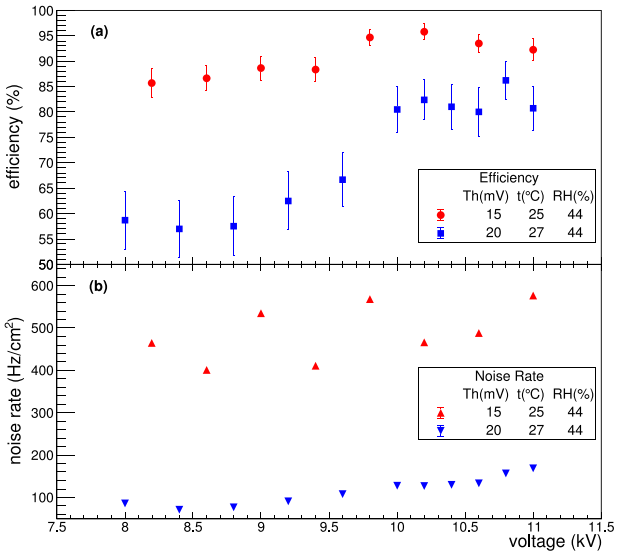

Fig. 4. (a) The efficiency as a function of the applied voltage for the RPC, (b) Noise rate as a function of the applied voltage.

5. Summary and outlook

A small size RPC prototype is built having a dimension of 27 cm × 27 cm bakelite plates of thickness 2 mm. The gas gap of the prototype is also made 2 mm. A new technique is followed for the linseed oil coating of the bakelite sheets. In conventional bakelite RPC, the linseed oil coating is done after making the gas gap. In case of BaBar RPC the performance deteriorated drastically due to trapping of uncured linseed oil in the hidden storage cavities near the spacers [17]. To ensure that the curing is properly done throughout the entire surface, in this particular work, the linseed oil coating is done before making the gas gap. After the linseed oil coating, the plates are cured for 15 days. The advantage of this procedure is that after linseed oil coating it can be checked visually whether the curing is properly done or any uncured droplet of linseed oil is present or not.

The detector is tested with 100% Tetrafluoroethane ($C_2H_2F_4$) gas in the avalanche mode. Efficiency plateau ∼95% from 9.4 kV onwards and ∼85% from 10.1 kV onwards are obtained for the −15 mV and −20 mV discriminator threshold respectively. The noise rate is found to be very high for such a chamber compared to the results reported earlier for the RPCs with bakelite plates oil coated in the conventional way [31–33]. However, normally a small amount (4%–5%) of Isobutane is needed as quencher, and very small (∼0.3–0.5%) of SF_6 to avoid discharges and double signals. Moreover, Tetrafluoroethane is a prohibited gas nowadays, and very expensive, so it is not convenient as a gas in a real experiment. So, we are planning to repeat the tests with conventional gas mixture in near future.

The detection efficiency of the RPC in the cosmic ray test is compared with the conventional linseed oil coated bakelite RPC [1,20,21]. However, the investigation behind the high leakage current and high noise rate is going on.

As a proof of principle, the paper introduced a new technology of oil coating in RPC with bakelite electrodes. The cosmic test showed that this technology does work. However, the cosmic test does not answer on the main questions about the long-term stability and the particle rate capabilities. The long-term stability test, measurement of timing properties and the effect of the temperature and relative humidity on the performance are planned to be studied in future. To answer the question of particle rate capabilities, it is required to do test with an accelerator, which is also in future plan.

This work involves a small prototype. However, detectors with much larger size are used in actual experiments. So, we plan to repeat

this technique to build large RPC detector and test the performance of the same.

Declaration of competing interest

The authors declare that they have no known competing financial interests or personal relationships that could have appeared to influence the work reported in this paper.

Acknowledgements

We would like to thank Mr. Shivshant Chauhan for his help in the installation of the detector and running the experiment. We would also like to thank Mr. Subrata Das for helping in fabrication of the pick-up strips used in this study. The authors would also like to thank Prof. Sibaji Raha, Prof. Rajarshi Ray and Dr. Sidharth K. Prasad for valuable discussions and suggestions in the course of the study. This work is partially supported by the CBM-MuCh project from BI-IFCC, DST, Govt. of India. A. Sen acknowledges his Inspire Fellowship research grant [DST/INSPIRE Fellowship/2018/IF180361].

References

[1] R. Santonico, R. Cardarelli, Nucl. Instrum. Methods A 187 (1981) 377.
[2] BaBar, Technical Design Report, SLAC-R-95-457.
[3] E. Cerron Zeballos, et al., Nucl. Instrum. Methods. A 374 (1996) 132.
[4] R. Arnaldi, et al., Nucl. Instrum. Methods. A 451 (2000) 462.
[5] ATLAS Collaboration, ATLAS Muon Spectrometer Technical Design Report, CERN/LHCC, pp. 97-22.
[6] G. Chiodini, et al., Nucl. Instrum. Methods A 581 (2007) 213.
[7] CMS Collaboration, Muon Project, CERN/LHCC 97-32.
[8] D. Belver, et al., Nucl. Instrum. Methods. A 602 (2009) 687.
[9] J. Han, et al., Nucl. Instrum. Methods. A 577 (2007) 552.
[10] G. Aielli, et al., Nucl. Instrum. Methods. A 562 (2006) 92.
[11] R. Acquafredda, et al., JINST 4 (2009) P04018.
[12] Q. Zhang, et al., Nucl. Instrum. Methods. A 583 (2007) 278.
[13] http://www.ino.tifr.res.in/ino/.
[14] S. Biswas, et al., Nucl. Instrum. Methods. A 602 (2009) 749.
[15] A. Behera, et al., Nucl. Instrum. Methods. A 602 (2009) 784.
[16] I. Deppner, et al., Nucl. Instrum. Methods. A 661 (2012) S121.
[17] J. Va'vra, Nucl. Instrum. Methods. A 515 (2003) 354.
[18] C. Lu, Nucl. Instrum. Methods. A 602 (2009) 761.
[19] S. Biswas, et al., Nucl. Instrum. Methods. A 604 (2009) 310.
[20] M. Abbrescia, et al., Nucl. Instrum. Methods. A 394 (1997) 13.
[21] B. Hong, et al., J. Korean Phys. Soc. 48 (4) (2006) 515.
[22] J. Zhang, et al., Nucl. Instrum. Methods. A 540 (2005) 102.
[23] F. Anulli, et al., Nucl. Instrum. Methods. A 508 (2003) 128.
[24] F. Anulli, et al., Nucl. Instrum. Methods. A 539 (2005) 155.
[25] Y. Haddad, et al., Nucl. Instrum. Methods. A 718 (2013) 424.
[26] L. Pizzimento, et al., JINST 15 (2020) C11010.
[27] E. Nandy, et al., Proc. of the DAE-BRNS Symp. on Nucl. Phys., Vol. 61, 2016, p. 1024.
[28] K.K. Meghna, et al., Nucl. Instrum. Methods. A 816 (2016) 1.
[29] A. Sen, et al., JINST 15 (2020) C06055.
[30] S. Sahu, et al., JINST 12 (2017) C05006.
[31] A. Bergnoli, et al., Nucl. Phys. B (Proc. Suppl.) 158 (2006) 93.
[32] A. Bergnoli, et al., IEEE Trans. Nucl. Sci. 52 (6) (2005).
[33] F. Bossu, et al., JINST 7 (2012) T12002.

Nuclear Inst. and Methods in Physics Research, A 1045 (2023) 167572

Contents lists available at ScienceDirect

Nuclear Inst. and Methods in Physics Research, A

journal homepage: www.elsevier.com/locate/nima

Characterization of a new RPC prototype using conventional gas mixture

A. Sen *, S. Chatterjee, S. Das, S. Biswas

Department of Physics, Bose Institute, EN-80, Sector V, Kolkata 700091, India

ARTICLE INFO

Keywords:
Resistive Plate Chamber
Gaseous detector
Cosmic ray
Efficiency
Noise rate
Linseed oil

ABSTRACT

Resistive Plate Chamber is a well-known gaseous detector in the field of High Energy Physics experiments for its good tracking capability, high efficiency, good time resolution, and low cost of fabrication. The main issue in Resistive Plate Chamber is its limitation in the rate handling capability. Several experimental groups have developed sophisticated techniques to increase the particle rate capability and reduce the noise rate of this detector. In bakelite Resistive Plate Chamber linseed oil coating on the inner electrode surface is done to get rid of surface roughness of the resistive electrodes. We developed a new method for linseed oil coating in case of bakelite Resistive Plate Chamber to achieve good efficiency (> 90%). In this article, we discussed the test results obtained from a prototype fabricated in this new method, using a conventional gas mixture.

1. Introduction

Resistive Plate Chamber (RPC) is a gaseous detector made up of resistive electrode plates *e.g.* bakelite, glass, ceramic, etc. [1–4]. High Energy Physics experiments have been using RPCs for triggering and tracking because of their high efficiency and good time resolution. RPCs are also being used in several cosmic ray experiments to cover large detection area [5,6]. Future heavy-ion experiments *e.g.* Compressed Baryonic Matter (CBM) is exploring the possibility of using RPCs for muon detection [7].

In bakelite RPC linseed oil coating [8] is done to get rid of the surface roughness of the resistive plates [9]. The linseed oil coating also helps to reduce the noise rate of the detector, protects the electrode plates from Hydrofluoric Acid (HF) corrosive effect and it also has photon quenching properties that reduce the UV sensitivity of the electrode plates.

In conventional linseed oil coated bakelite RPC, a serious problem was observed in the BaBar experiment. The coated linseed oil forms stalagmite that subsequently introduces conducting paths through the gas gap specially around the spacers and the discharge permanently damages the detector. The formation of stalagmite is due to the polymerization of uncured linseed oil droplets present on the surface [10]. However, lot of R&D is performed and the solution is found out for this issue [11].

A new technique of linseed oil coating on the bakelite plates [12] is introduced in which one can check visually whether there is any uncured oil present inside the gas gap. With this new technique one RPC prototype was built and tested with 100% $C_2H_2F_4$ gas. In this article the test results of the RPC prototype with conventional $C_2H_2F_4$ and i-C_4H_{10} mixture is presented.

2. Detector description and experimental set-up

The detector is built with two 27 cm× 27 cm bakelite plates of thickness 2 mm and having bulk resistivity of ∼ 3× 10^{10} Ω cm (at 22 °C). Four edge spacers, two gas nozzles, one button spacer made of polycarbonate (resistivity ∼ 10^{15} Ω cm) and having thickness of 2 mm are used to make the gas gap. The surface resistivity of the outer graphite surface of the electrode plates are measured to be ∼ 510 kΩ/□ and 540 kΩ/□.

The signal is read out from the copper strips of dimension 2.5 cm × 27 cm. The strips are covered with 100 μm thick mylar foils to isolate them from the graphite layers. The details of the fabrication of the chamber is described in [12].

Three scintillation detectors of dimensions 10 cm × 10 cm (SC1), 10 cm × 2 cm (SC2), 20 cm × 20 cm (SC3) are used to generate the trigger for the detector. All the scintillators are operated at +1550 V and −15 mV threshold is applied to the leading edge discriminator (LED). The RPC signal from the pick-up strip is first fed to a 10x fast amplifier and then the output goes to the LED. Suitable thresholds are applied to the LEDs to reduce the noise. From the LED, one output goes to the scalar to count the number of the signal from the RPC which is known as the noise count or singles count of the chamber. The other output from LED goes to the dual timer where the discriminated RPC signal is stretched to avoid any double counting of the pulses and also to apply the proper delay to match the signal with the trigger. The output of the dual timer is taken in coincidence with the trigger and this is defined as the 4-fold signal. The window of the cosmic ray test set-up is of area 10 cm × 2 cm. The block diagram of the set-up is shown in Fig. 1.

* Corresponding author.
E-mail address: arindam@jcbose.ac.in (A. Sen).

https://doi.org/10.1016/j.nima.2022.167572
Received 8 June 2022; Received in revised form 4 August 2022; Accepted 3 October 2022
Available online 14 October 2022
0168-9002/

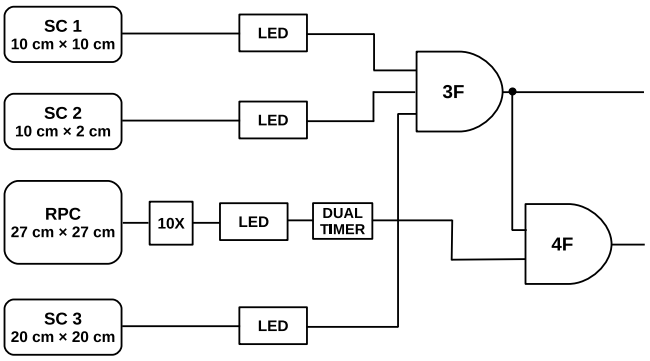

Fig. 1. Block diagram of the cosmic ray test set-up for characterization of the detector [12].

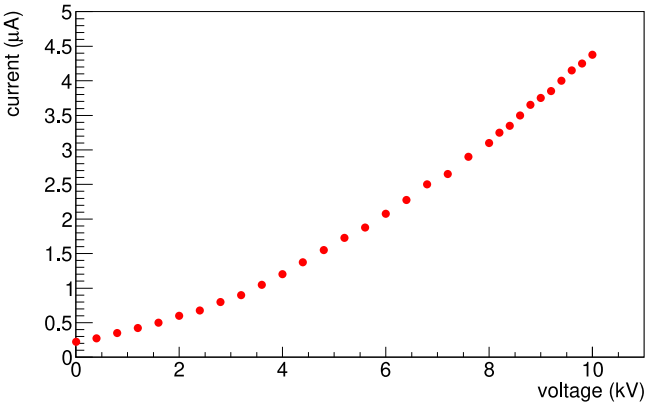

Fig. 2. Leakage current as a function of the voltage for $C_2H_2F_4$ and i-C_4H_{10} gas mixture in 90/10 volume ratio.

3. Result

The chamber is tested with cosmic rays in avalanche mode. The detector is purged with Tetrafluoroethane ($C_2H_2F_4$) and Isobutane (i-C_4H_{10}) gas mixture in 90/10 volume ratio. The leakage current through the RPC module is measured as a function of the applied high voltage (HV) and shown in Fig. 2.

The efficiency of the RPC module for the cosmic rays is defined as the ratio of the 4-fold counts to the 3-fold coincidence trigger count of the plastic scintillator telescope for a fixed duration and the noise rate of the RPC, is defined as the number of counts per unit area of the strip per second. The efficiency and noise rate are studied by varying the applied HV. The RPC is tested with −20 mV and −25 mV threshold settings to the LED. An efficiency of greater than 90% is achieved from 10 kV onwards for both the threshold settings. The maximum noise rates are found to be 120 Hz/cm^2 and 80 Hz/cm^2 for the −20 mV and −25 mV thresholds respectively as shown in Fig. 3.

4. Summary

A linseed oil-coated RPC prototype of dimension 27 cm × 27 cm is fabricated using indigenous resistive bakelite plates. The linseed oil coating is done before making the gas gap. Before building the detector, electrode plates are checked visually whether the oil is cured properly or if any uncured oil is present on the surface.

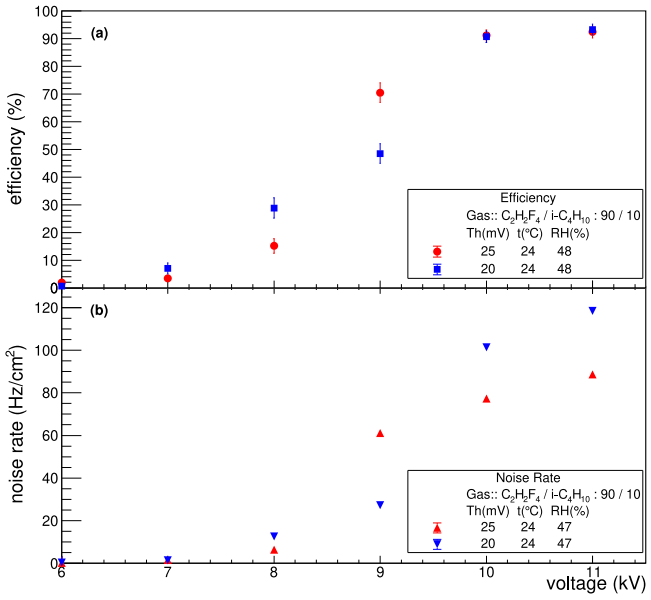

Fig. 3. (a) Efficiency as a function of the applied voltage, (b) Noise rate as a function of the applied voltage for $C_2H_2F_4$ and i-C_4H_{10} gas mixture in 90/10 volume ratio.

The detector is tested with Tetrafluoroethane ($C_2H_2F_4$) and Isobutane (i-C_4H_{10}) in 90/10 volume ratio. Both the current and noise rate are very low for this gas mixture compared to the 100% $C_2H_2F_4$ used earlier for the same detector [12]. An efficiency of greater than 90% is found from 10 kV onwards with a maximum noise rate of 120 Hz/cm^2 at - 20 mV threshold.

Declaration of competing interest

The authors declare that they have no known competing financial interests or personal relationships that could have appeared to influence the work reported in this paper.

Acknowledgments

The authors would like to thank Ms. Rudrapriya Das for her help in running the experiment and Prof. Sanjay K Ghosh for many valuable discussions and suggestions during the course of study. The authors would also like to thank Mr. Subrata Das for building the readout strips. This work is partially supported by the CBM-MuCh project from BI-IFCC, DST, Govt. of India. A. Sen acknowledges his Inspire Fellowship research grant [DST/INSPIRE Fellowship/2018/IF180361].

References

[1] R. Santonico, R. Cardarelli, Nucl. Instrum. Methods A 187 (1981) 377.
[2] A. Sen, et al., JINST 15 (2020) C06055.
[3] G.C. Trinchero, et al., Nucl. Instrum. Methods A 508 (2003) 102.
[4] A. Laso Garcia, et al., JINST 7 (2012) P10012.
[5] G. Aielli, et al., Nucl. Instrum. Methods A 562 (2006) 92.
[6] Q. Zhang, et al., Nucl. Instrum. Methods A 583 (2007) 278.
[7] A. Kiseleva, et al., Indian J. Phys. 85 (1) (2011) 211–216.
[8] B. Hong, et al., J. Korean Phys. Soc. 48 (4) (2006) 515.
[9] C. Lu, Nucl. Instrum. Methods A 602 (2009) 761.
[10] J. Va'vra, Nucl. Instrum. Methods A 515 (2003) 354.
[11] F. Anulli, et al., Nucl. Instrum. Methods A 508 (2003) 128.
[12] A. Sen, et al., Nucl. Instrum. Methods A 1024 (2022) 166095.

Pramana – J. Phys. (2021) 95:64
https://doi.org/10.1007/s12043-021-02106-z

Cosmic ray flux and lockdown due to COVID-19 in Kolkata – Any correlation?

A SEN, S CHATTERJEE, S ROY, R BISWAS, S DAS, S K GHOSH and S BISWAS*

Department of Physics and Centre for Astroparticle Physics and Space Science, Bose Institute, EN-80, Sector V, Kolkata 700 091, India
*Corresponding author. E-mail: saikat@jcbose.ac.in; saikat.ino@gmail.com

MS received 20 November 2020; revised 30 December 2020; accepted 5 January 2021

Abstract. Cosmic ray muon flux is measured by the coincidence technique using plastic scintillation detectors in the High Energy Physics Detector Laboratory at Bose Institute, Kolkata. Due to the COVID-19 outbreak and nationwide complete lockdown, the laboratory was closed from the end of March 2020 till the end of May 2020. After lockdown, although the city is not in its normal state, we still were able to take data on some days. The lockdown imposed a strict restriction on the transport service other than the emergency ones and also most of the industries were shut down in and around the city. This lockdown has significant effect on the atmospheric conditions in terms of change in the concentration of air pollutants. We have measured the cosmic ray flux before and after the lockdown to observe the apparent change if any, due to change in the atmospheric conditions. In this article, we report the measured cosmic ray flux at Kolkata (22.58°N 88.42°E and 11 m above the Sea Level) along with the major air pollutants present in the atmosphere before and after the lockdown.

Keywords. Cosmic ray; muon flux; plastic scintillation detector; air quality index; air pollutants.

PACS Nos 29.40.Mc; 95.55.Vj; 95.85.Ry; 96.40.–z; 07.89.+b

1. Introduction

Cosmic ray consists of high-energy particles that mostly originate from the outer space, with some very high energy particles which can have extragalactic origin. Primary cosmic rays consist of 90% protons, 9% α-particles and other heavier nuclei [1]. These primary cosmic rays interact with the gas molecules in the atmosphere and produce secondary cosmic rays. These secondary particles consist mostly of pions and some kaons. Neutral pions (π^0) decay into γ-rays that generate electromagnetic showers (e^+, e^-, γ), which possess low penetration power. Charged pions (π^+, π^-) decay into muons and neutrinos. Neutrinos have a very small cross-section for interaction and typically pass through the Earth without any further interactions. On the other hand, muons are heavy particles and thus loss of energy through bremsstrahlung is negligible for them. This makes the muon a very penetrating particle, unlike electron. The muon has a lifetime of 2.2 μs, yet it still makes it down to detectors at the surface of the Earth traversing through the atmosphere. This is because muons travels at a speed that is close to that of light and thus experience relativistic time dilation and therefore can be detected by our detectors. Since the secondary cosmic rays are mostly muons and they can travel large distance through the atmosphere before they are detected, it will be really interesting if any correlation of this cosmic ray muon flux with the change in atmosphere in terms of the concentration of air pollutants is found [2–4].

For this study, cosmic ray flux has been measured in our laboratory using plastic scintillator detectors before and after the imposition of lockdown due to the COVID-19 pandemic. The effects of atmospheric pressure and temperature on the muon flux have also been studied here. A brief description of the change of the atmospheric parameters due to lockdown is discussed in the next section. The succeeding sections describe the details of the experimental set-up and results, followed by summary and discussions.

2. Effect of lockdown

India is at a critical stage in its fight against COVID-19 with positive cases crossing 89,58,140 and death toll at

Published online: 17 April 2021

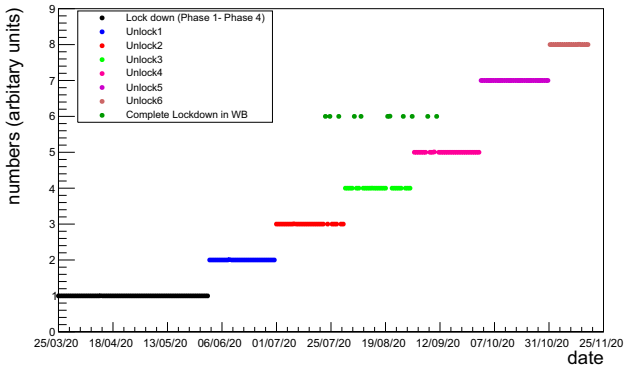

Figure 1. Different phases of lockdown and unlock as a function of date. The complete lockdown is marked with 1, different unlock phases are marked as 2, 3 so on and the complete lockdown days in West Bengal during the unlock phases are marked with 6.

1,31,618 until November 18, 2020 [5]. The entire country was under complete lockdown from March 25 to April 14, 2020, for 21 days, which was further extended by the Government of India till May 3, 2020, followed by the third phase of lockdown till May 17, 2020, and the fourth phase till May 31, 2020, to tackle the spread of COVID-19. Restrictions on social gathering and travelling resulted in the shutdown of all the businesses which include industries, transport (air, water and surface), markets, shops, tourism, construction and demolition, hotels and restaurants, mining and quarrying, etc. except essential services like groceries, milk, medicines and emergency services like hospital, fire service and administration. In June 2020, both central and state governments declared restricted unlocking phase. While unlock phases started from 1 June 2020, there were complete lockdown in West Bengal on some selected dates to fight against COVID-19. The dates of lockdown are mentioned in figure 1.

The complete lockdown is marked with 1, different unlock phases are marked as 2, 3 so on and the complete lockdown days in West Bengal during the unlock phases are marked with 6. During the lockdown (25 March–6 April 2020; Lockdown Phase-1) and before lockdown (10–20 March 2020), significant variation in the concentrations of the five most abundant pollutants in the air ($PM_{2.5}$, PM_{10}, NO_2, CO, O_3) are observed in Kolkata. The concentrations of air pollutants in Kolkata are decreased by ∼23% ($PM_{2.5}$), ∼34% (PM_{10}), ∼60% (NO_2), ∼29% (CO) while the O_3 concentration is increased by ∼17% due to the clearer atmosphere compared to that before the lockdown period [2]. We also looked into the last year data for the same period (March–April, 2019) and found that, during the lockdown, the concentrations of air pollutants are decreased by ∼27% ($PM_{2.5}$), ∼32% (PM_{10}), ∼66% (NO_2), ∼16% (CO) and O_3 concentration is increased by ∼87% [2].

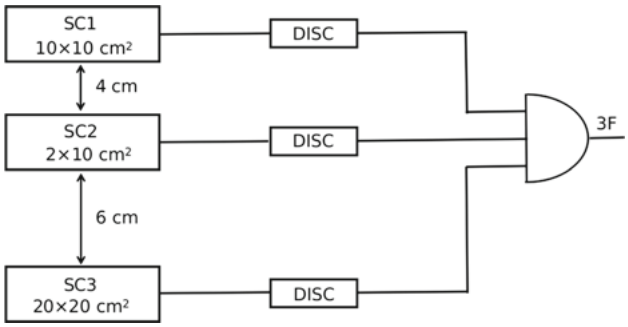

Figure 2. Schematic of the experimental set-up for muon flux measurement at the laboratory.

We have used the live day-to-day data from ref. [6] of the concentrations of the seven major air pollutants and studied their effects on cosmic ray flux. In our work, we have reported the measured muon fluxes before and after the lockdown at Kolkata and tried to correlate the same with the change in concentrations not only of the individual components of air pollutants but also of the total amount of pollutants.

3. Experimental set-up

The schematic of the muon flux measurement set-up is shown in figure 2. Three plastic scintillators tagged as SC1, SC2 and SC3, made using BC400 material are used in this set-up [7,8]. The dimensions of these scintillators are 10×10 cm^2, 2×10 cm^2 and 20×20 cm^2 respectively. The coincidence area of the three detectors is 20 cm^2. The distance between the top and bottom scintillators is ∼10 cm whereas that between the top and the middle one is 4 cm. Each scintillator is connected with a photomultiplier tube (PMT) and a base where one SHV (safe high voltage) and one BNC (Bayonet Neill–Concelman) connectors are provided for the application of high voltage (HV) and collection of signals respectively. A voltage of +1550 V is applied to all the PMTs. Thresholds to the discriminators are set to −15 mV for all the scintillators. The width of each discriminator output is kept at 50 ns. The coincidence of these three signals is achieved using a logic unit. The three-fold coincidence signal is then counted using a scaler and then divided by the product of the area of coincidence window (20 cm^2), muon detection efficiency of the system (∼72%) [8] and the measurement time to get the muon flux. The calculated muon flux is then multiplied by a factor of 0.95 to correct the effect of the difference in the threshold settings to the discriminator for the scintillators, during the efficiency measurement [8] (threshold is −30 mV) and the present measurement

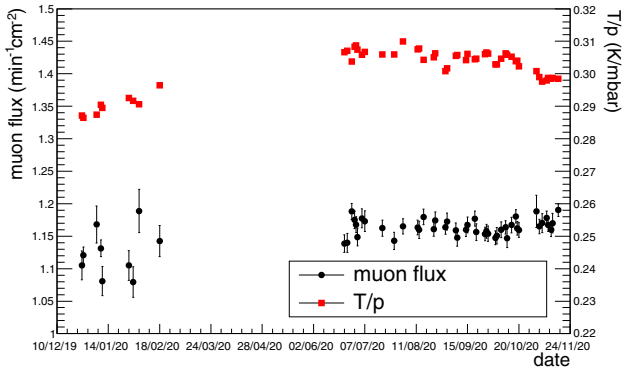

Figure 3. Cosmic ray muon flux and T/p as a function of date.

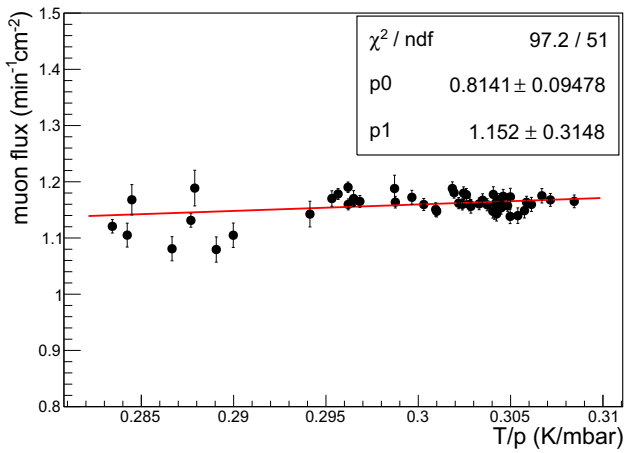

Figure 4. Correlation of cosmic muon flux with the ratio of temperature and pressure.

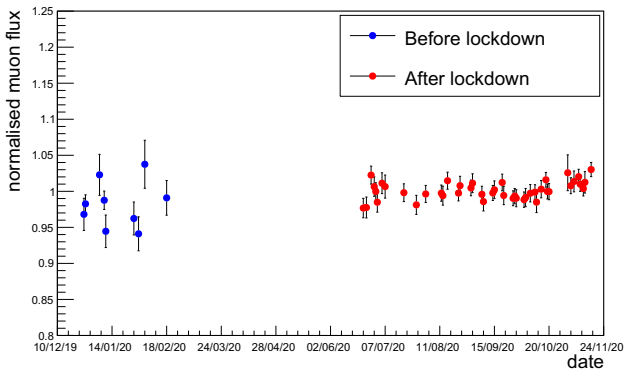

Figure 5. Normalised muon flux as a function of date. The gap between the two sets of data is the period of lockdown.

(threshold is −15 mV). Each data point represents a 30-min long measurement. To check the health of the individual detectors, the single count rates of all the modules are measured several times. The single count rates of scintillators SC1, SC2 and SC3 are found to be ∼77, ∼28 and ∼171 Hz respectively.

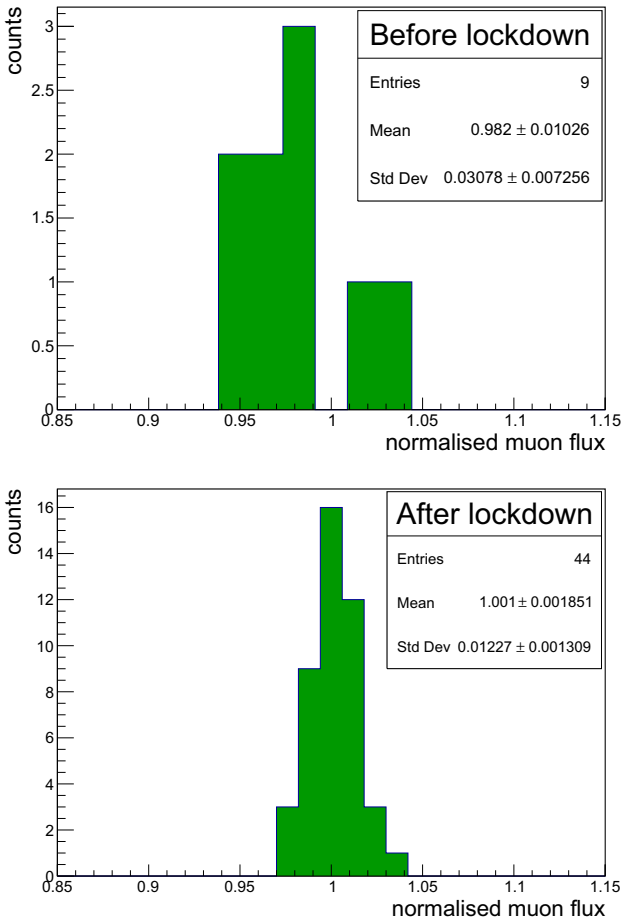

Figure 6. Distribution of normalised muon flux before and after the lockdown.

4. Results

The cosmic ray flux is measured in Kolkata before and after the lockdown due to the COVID-19 outbreak. The average muon flux before and after the lockdown is shown in figure 3 as a function of date. We had a very small amount of data before lockdown. The cosmic ray flux depends on atmospheric parameters like temperature and pressure [9,10]. In this work, the temperature and pressure data are collected from ref. [11]. The ratio of temperature and pressure as a function of date is also shown in figure 3. In order to normalise the temperature ($T = t + 273$) and pressure (p) effects, a simple correlation between cosmic muon flux and T/p is studied using the relation $p0 + p1(T/p)$. The correlation between muon flux and T/p is shown in figure 4. The parameters obtained from the correlation are 0.81 ± 0.09 $\mathrm{min}^{-1}\,\mathrm{cm}^{-2}$ ($p0$) and 1.15 ± 0.31 $\mathrm{min}^{-1}\,\mathrm{cm}^{-2}\,\mathrm{k}^{-1}$ mbar ($p1$) respectively.

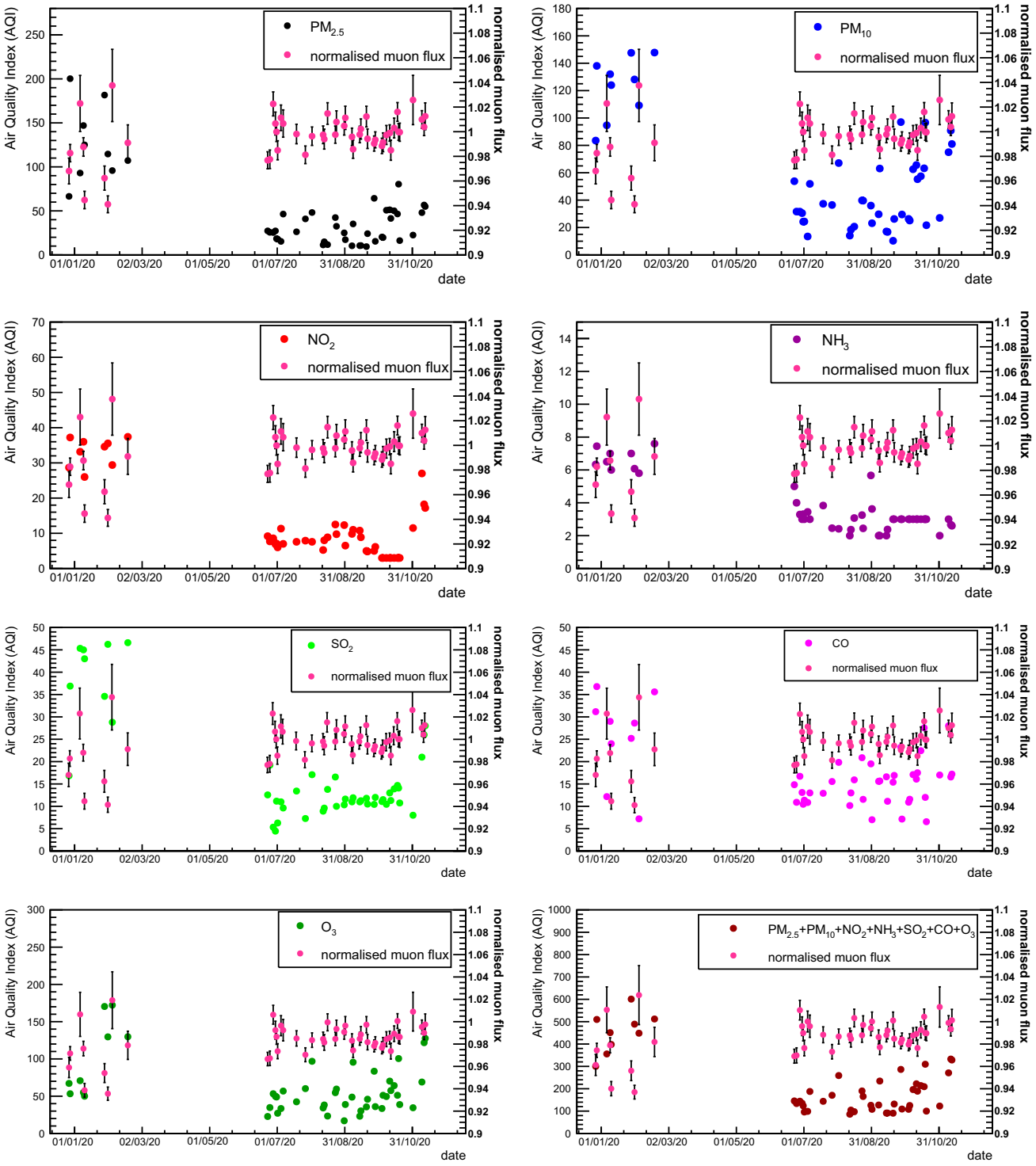

Figure 7. Average air quality index (AQI) of seven most abundant air pollutants measured at Bidhannagar, Kolkata station [6] and the normalised muon flux as a function of date.

A positive correlation is observed between the muon flux and T/p. Using the parameters, the muon flux measured before and after the lockdown is normalised and shown in figure 5.

In figure 6, the distribution of the normalised muon flux is shown before and after the lockdown. It is found that the mean normalised muon flux before the lockdown period is 0.982 with a standard deviation of 0.031,

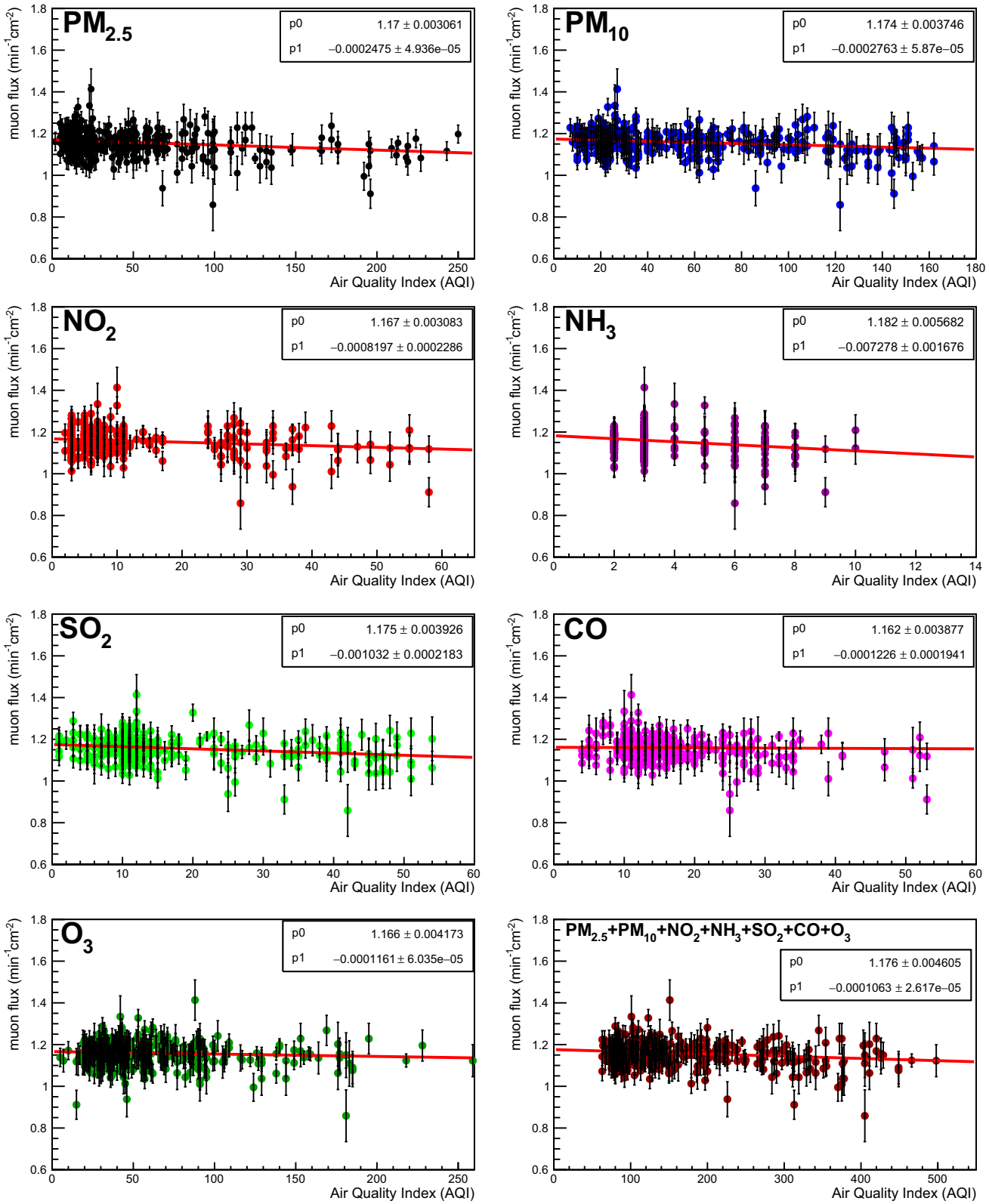

Figure 8. Measured muon flux as a function of AQI of seven most abundant air pollutants.

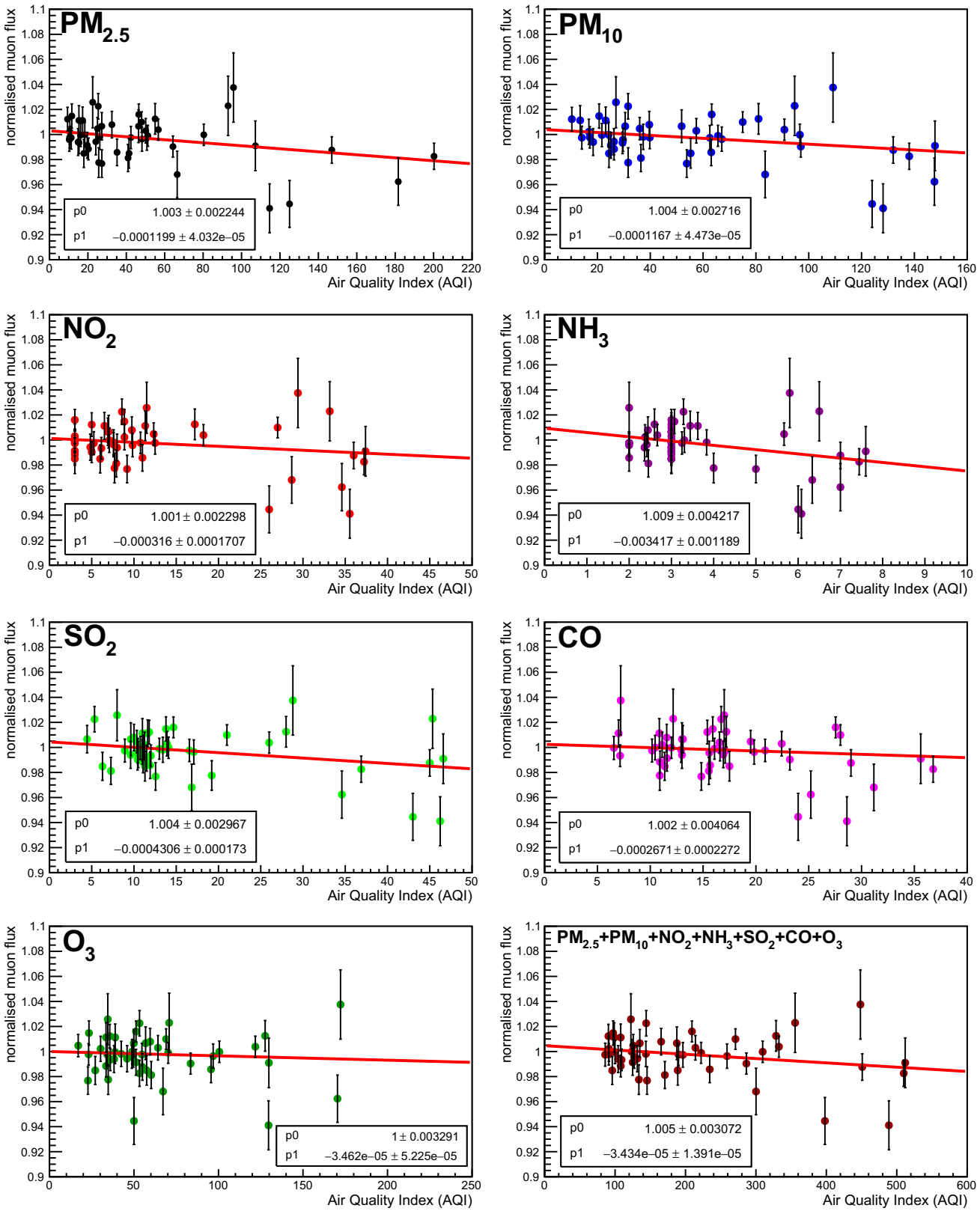

Figure 9. Normalised muon flux as a function of AQI of seven most abundant air pollutants.

Table 1. Value of the fit parameters of the muon flux vs. AQI curve with seven most abundant air pollutants.

Air pollutant type	$p0$	$p1$
$PM_{2.5}$	1.17 ± 0.003061	−0.0002475 ± 4.936e-05
PM_{10}	1.174 ± 0.003746	−0.0002763 ± 5.87e-05
NO_2	1.167 ± 0.003083	−0.0008197 ± 0.0002286
NH_3	1.182 ± 0.005682	−0.007278 ± 0.001676
SO_2	1.175 ± 0.003926	−0.001032 ± 0.0002183
CO	1.162 ± 0.003877	−0.0001226 ± 0.0001941
O_3	1.166 ± 0.004173	−0.0001161 ± 6.035e-05
Gross	1.176 ± 0.004605	−0.0001063 ± 2.617e-05

whereas that after the lockdown is 1.001 with a standard deviation of 0.012, i.e. 1.9% increment in muon flux is found after the lockdown.

In figure 7, we have reported the individual air pollutants (average air quality index (AQI) which is proportional to the concentration of the pollutants) before and after the lockdown (on the dates of cosmic ray data recording) and a clear decrement in the concentrations of the air pollutants has been observed after the lockdown. One striking thing we observe during this study, is that the concentration of O_3 also decreases after lockdown in our case unlike in ref. [2] where the concentration of O_3 was reported to be increased during the lockdown (for a short time period though). Actually in ref. [2] the concentration of O_3 was reported to be increased during the lockdown (March 25–April 6, 2020) compared to the values before the lockdown (10–20 March 2020). In ref. [6], the concentration values of O_3 before the lockdown are quoted for December 27, 2019 to February 18, 2020 and after lockdown those are during June 24, 2020 and November 17, 2020. Clearly, the dates in refs [2,6] are different and hence the discrepancy. Figure 8 represents the variation of the muon flux with AQI for the seven air pollutants individually and with the gross pollutants present. We observe a correlation between cosmic ray muon flux and the concentrations of the air pollutants before and after the lockdown where the flux increases with decrease in the concentrations of the air pollutants. The details of the variation found by linear fitting of the muon flux vs. air quality index curve for different pollutants, are tabulated in table 1.

T/p normalised muon flux is also plotted as a function of the average AQI for the seven air pollutants individually and with the gross pollutants present in figure 9. Here also we observed that the normalised flux increases with decrease in the concentrations of the air pollutants.

5. Summary and discussion

Cosmic ray muon flux was measured using the coincidence technique with plastic scintillation detectors. To restrict the outbreak of COVID-19, Government of India imposed 67 days of nationwide complete lockdown in three phases. After that, the unlocking was declared in phases in different parts of India. Before the lockdown, we collected some cosmic ray flux data. After lockdown the measurement was continued to compare with the flux measured before lockdown. In our measurement, it is found that the cosmic ray flux remained more or less unchanged before and after the lockdown. However, it is well known that atmospheric temperature and pressure affect the cosmic ray flux and we looked for any such possible correlation. A positive correlation is indeed observed between the muon flux and the ratio of atmospheric temperature and pressure. This correlation is fitted well by a function of the form $p0 + p1(T/p)$, and the fit parameters $p0$ and $p1$ are used to normalise the T/p effect on the cosmic muon flux. It is found that the mean normalised muon flux before and after the lockdown period are 0.982 with a standard deviation of 0.031 and 1.001 with a standard deviation of 0.012 respectively.

A lockdown such as the one implemented due to COVID-19 typically has significant influence on the atmospheric condition in terms of the presence of pollutants. We wanted to study any possible correlation of measured cosmic ray muon flux with this. To realise this, we considered the seven most abundant air pollutants ($PM_{2.5}$, PM_{10}, NO_2, NH_3, SO_2, CO, O_3) and investigated the change in their concentrations with date (before and after the lockdown). We found significant declination in the concentrations of the pollutants and we tried to look for any correlation with the measured muon flux within the stipulated time window. The result shows a clear correlation as with decreasing concentrations of the air pollutants we observed an increasing trend of the normalised muon flux. From our observation, one can comment that the increase in cosmic ray flux can also be considered as one of the secondary indicators of less polluted air.

However, there are a few limitations of our measurement. First, the detector coverage area was very small,

resulting in low statistics. Second, the statistics of muon data before lockdown is small. It will be very interesting if any other research laboratory having a large facility of cosmic ray flux measurement can try to study such correlation.

Acknowledgements

The authors would like to thank Dr Abhijit Chatterjee, Prof. Sibaji Raha, Prof. Rajarshi Ray, Prof. Somshubhro Bandyopadhyay and Dr Sidharth K Prasad for valuable discussions and suggestions in the course of the study. We would also like to thank Mrs Sharmili Rudra, Dr Rama Prasad Adak, Mr Dipanjan Nag, Ms Nilanjana Nandi and Mr Subrata Das for helping in the fabrication of the detectors. This work is partially supported by the research grant SR/MF/PS-01/2014-BI from DST, Govt. of India, the research grant of CBM-MuCh project from BI-IFCC, DST, Govt. of India and IRHPA (Intensification of Research in High Priority Areas/Sanction No. IR/S2/PF.01/2011) scheme. A Sen acknowledges his Inspire Fellowship research grant (DST/INSPIRE Fellowship/2018/IF180361).

References

[1] V Valkovič, *Radioactivity in the environment*, https://doi.org/10.1016/B978-044482954-2.50002-2 (2000) pp. 5–32
[2] S Jain *et al*, *Aerosol Air Quality Res*. **20**, 1222 (2020)
[3] S Chen *et al*, https://doi.org/10.1371/journal.pone.0215663 (2019)
[4] Abhijit Chatterjee *et al*, *Atmospheric environment*, https://doi.org/10.1016/j.atmosenv.2020.117947
[5] https://www.covid19india.org/
[6] https://app.cpcbccr.com/AQI_India/
[7] S Roy *et al*, *Proceedings of ADNHEAP 2017*, Springer Proceedings in Physics 2017, pp. 199–204, ISBN 978-981-10-7664-0
[8] S Shaw *et al*, *Proc. DAE Symp. Nucl. Phys.* **62**, 1030 (2017)
[9] M Neira, A Prüss-Ustün and P Mudu, *Lancet* **392**, 1178 (2018)
[10] M Zazyan *et al*, *J. Space Weather Space Clim.* **5**, A6 (2015)
[11] https://www.timeanddate.com/weather/india/kolkata